

MASTER THESIS

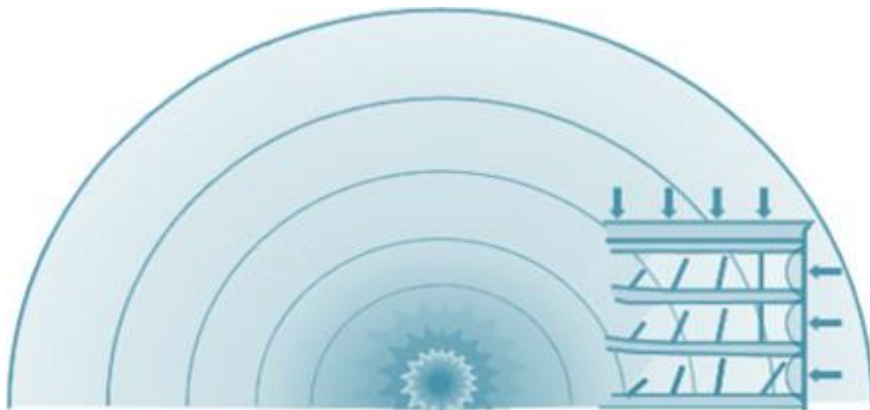
**Prediction of the nonlinear dynamic
behaviour of a concrete slab
subjected to blast load**

Main report

Author: L. Kraaijenbrink

Status: Final

Date: 23 August 2022



HASKONINGDHV NEDERLAND B.V.

George Hintzenweg 85
3068 AX Rotterdam
Industry & Buildings
Trade register number: 56515154

+31 88 348 90 00 **T**
info@rhdhv.com **E**
royalhaskoningdhv.com **W**

Document title: Prediction of the nonlinear dynamic behaviour of a concrete slab subjected to blast load

Subtitle: Main report

Status: 1.2/Final

Date: 23 August 2022

Author(s): ing. L. Kraaijenbrink

Thesis committee: prof.dr.ir. J.G. Rots
prof.dr.ir. M.A.N. Hendriks
dr.ir. K.N. van Dalen
ir. P.J. Flink

TU Delft
TU Delft
TU Delft
Royal HaskoningDHV

Unless otherwise agreed with the Client, no part of this document may be reproduced or made public or used for any purpose other than that for which the document was produced. HaskoningDHV Nederland B.V. accepts no responsibility or liability whatsoever for this document other than towards the Client.

Please note: this document contains personal data of employees of HaskoningDHV Nederland B.V.. Before publication or any other way of disclosing, consent needs to be obtained or this document needs to be anonymised, unless anonymisation of this document is prohibited by legislation.

Preface

I have written this thesis for my master's degree Civil Engineering, track Structural Engineering at Delft University of Technology, The Netherlands. Commissioned by Royal HaskoningDHV I researched the topic of blast analysis on concrete structures. I find this topic very fascinating, because of the dynamic aspects of it together with the structural challenges it provides.

First of all, I would like to thank Royal HaskoningDHV for giving me the opportunity to graduate at such a well-regarded company. I have learned a lot and met many interesting people. Special thanks to ir. Peter Flink, who guided me through the thesis.

Also, I would like to thank prof.dr.ir. Jan Rots, prof.dr.ir. Max Hendriks and dr.ir. Karel van Dalen for given me the assistance I needed.

Last, but not least, a thanks to my family for supporting me the whole way through my master's degree. A lot of time and dedication went into this education, which was hard sometimes.

Lennart Kraaijenbrink

Den Haag, 23rd of August 2022

Abstract

With the rise of hydrogen as a green alternative for fossil fuels, the demand for storage capacity of hydrogen increases significantly. Due to the high risk of explosions in urban environments it brings along, the blast analysis of buildings within in range of the explosions becomes more relevant.

The goal of this research is to develop a quick method to analyse the roof of a building subjected to blast load. This is done by first clarifying the blast load definition on a reinforced concrete (RC) structural element through existing design standards and literature. Next, the material behaviour of the concrete and the reinforcement steel is scrutinised by an extensive literature study. Materials behave differently under dynamic loads. The dynamic material properties are increased by the strength increase factor (SIF) and the dynamic increase factor (DIF).

In blast analysis, most energy is dissipated through plastic deformation. Therefore, it is of great importance to accurately describe the nonlinear behaviour of RC elements. The nonlinear behaviour of RC elements is translated in the moment-curvature relationship. This relationship is calculated on cross-sectional level and serves as input for the global beam or slab model. The global structural behaviour of the beam or the slab is calculated using the finite difference method (FDM). The FDM model generates a force-deflection (F-u) relationship which can be used in the single degree of freedom (SDOF) mass-spring system. The SDOF mass-spring system is used in this research to predict the dynamic behaviour of RC elements.

The research method is validated by published experiments and finite element analysis. Three experiments are reported, where the following results are obtained:

- Flexural stiffness may be assumed when the scaled distance is above $1.2 \text{ m/kg}^{1/3}$. This is labelled as the 'far field design range'.
- When choosing the DIFs carefully, the dynamic behaviour of RC elements can be predicted well.
- The FDM model can provide a good estimation of the nonlinear F-u relationship. The method of incorporating cracks in the FDM model is not previously presented in published literature.
- The unloading stiffness requires additional care. This research briefly covers the unloading stiffness.
- According to the UFC 3-340-02 (Department of Defence, US, 2008), RC elements without shear reinforcement and without the possibility of membrane action, fail at a support rotation of 2 degrees. This is where crushing is supposed to happen. This research shows that this is rather conservative and that the support rotation can go up to 6 degrees before failure.

Finally, the validated research method is applied on a case study. The case study contains a slab supported on two stiff beams on opposing sides. This results in a main span (weak direction) and a secondary span (stiff direction) due to the flexural stiffness of the supporting beams. In most cases, the slab supported by beams can be approached as a SDOF mass-spring system. After occurrence of cracks, the slab reinforcement in the main span direction will absorb most of the energy and is therefore the dominating member in the two degrees of freedom (2DOF) mass-spring system.

Table of Contents

1	Introduction	11
1.1	Background and motivation	11
1.2	Problem statement	12
1.3	Research objective	12
1.4	Report structure	14
2	Blast load	15
2.1	Mechanics of an explosion	15
2.2	Effects of an explosion	16
2.3	Interaction between blast and structure	17
2.4	Force acting on a roof	20
2.5	Far field and near field explosions	20
3	Material behaviour	21
3.1	Static material models	21
3.1.1	Concrete	21
3.1.2	Reinforcement steel	22
3.2	Static strength increase	23
3.3	Dynamic strength increase	23
3.3.1	Concrete compressive strength	24
3.3.2	Concrete compressive fracture energy	25
3.3.3	Concrete tensile strength	25
3.3.4	Tensile fracture energy	26
3.3.5	Young's modulus of concrete	27
3.3.6	Reinforcement steel strength	29
3.3.7	Reinforcement Young's modulus	31
4	Cross-sectional behaviour of reinforced concrete elements	32
4.1	Moment-curvature relationship	32
4.2	Failure criteria	34
5	Static behaviour of reinforced concrete elements	35
5.1	Finite difference method	35
5.2	One-way elements	36
5.2.1	Finite difference model	36
5.2.2	Force-deflection relationship	39
5.3	Two-way elements	39
5.3.1	Finite difference model	39
5.3.2	Force-deflection relationship	42

6	Dynamic behaviour of reinforced concrete elements	43
6.1	Structural response to a blast load	43
6.1.1	Mass-spring-damper system	43
6.1.2	Inertia effects	43
6.1.3	Structural damping	43
6.2	One-way elements as a single degree of freedom mass-spring system	44
6.2.1	Equation of motion and equivalent parameters	44
6.2.2	Analytical solution	45
6.2.3	Numerical solution	46
6.3	Two-way elements as a two degrees of freedom mass-spring system	48
6.3.1	Equations of motion and equivalent parameters	48
6.3.2	Numerical solution	51
7	Experimental validation and calibration	53
7.1	Validation experiment 1	53
7.1.1	Experiment observations	53
7.1.2	Moment-curvature relationship	53
7.1.3	Force-deflection relationship	54
7.1.4	Nonlinear time history analysis	55
7.2	Validation experiment 2	56
7.2.1	Experiment observations	56
7.2.2	Moment-curvature relationship	57
7.2.3	Force-deflection relationship	57
7.2.4	Nonlinear time history analysis	58
7.3	Validation experiment 3	58
7.3.1	Experiment observations	58
7.3.2	Moment-curvature relationship	59
7.3.3	Force-deflection relationship	60
7.3.4	Nonlinear time history analysis	60
8	Case study	62
8.1	Method	64
8.2	Original results	65
8.3	Parameters	66
8.4	Applied force	67
8.5	Moment-curvature relationship	68
8.6	Single degree of freedom mass-spring system	70
8.6.1	Force-deflection relationship	70
8.6.2	Deflection-time history	70
8.7	Two degrees of freedom mass-spring system	71
8.7.1	Case	71
8.7.1.1	Force-deflection relationship	71

8.7.1.2	Deflection-time history	72
8.7.2	Parametric study	73
8.7.2.1	Variation 1: SDOF and 2DOF mass-spring system comparison	73
8.7.2.2	Variation 2: Beam stiffness effect	74
8.7.2.3	Variation 3: Beam mass effect	75
9	Discussion	76
9.1	Nonlinear pressure distribution	76
9.2	Dynamic increase factors	76
9.3	Unloading stiffness	76
9.4	Failure mechanism	77
9.5	Post-crushing behaviour	77
9.6	Verification of the post-crushing behaviour	77
9.7	Case study	78
10	Conclusions and recommendations	79
10.1	Reflection on the research scope and assumptions	79
10.2	Reflection on the research objective	80
10.3	Reflection on the problem statement	81
10.4	Contribution of this research to existing studies	81
10.5	Recommendations and further development	82
11	References	83

Appendices

Appendix I – Experiment 1

Appendix II – Experiment 2

Appendix III – Experiment 3

Appendix IV – Analytical solution to the SDOF mass-spring system

Table of Tables

Table 3.1: DIF_t and DIF_G high strain rates (Vegt & Weerheijm, 2016)	27
Table 3.2: DIF_E for different strain rates	29
Table 3.3: Johnson-Cook parameters for steel reinforcement	31
Table 6.1: participating mass and load factor for different loading diagrams.	45
Table 8.1: Dynamic properties	66
Table 8.2: Concrete properties	66
Table 8.3: Reinforcement steel properties	66

Table of Figures

Figure 1.1: Location of Admin Old	11
Figure 1.2: Flowchart of the experiment calibration	13
Figure 2.1: Energy path of molecules through the reaction progress	15
Figure 2.2: Tools to lower the activation energy	16
Figure 2.3: Free field pressure for detonations (left) and deflagrations (right)	16
Figure 2.4: Blast wave interaction with the building (interaction with the ground not included)	17
Figure 2.5: Typical pressure function for blast analysis	17
Figure 2.6: Free air burst	19
Figure 2.7: Air burst	19
Figure 2.8: Surface air burst	19
Figure 2.9: Simplified pressure function on a roof	20
Figure 3.1: Stress-strain relationship for concrete in FEM analysis	22
Figure 3.2: Stress-strain relationship for reinforcement steel	22
Figure 3.3: strain rate ranges for different types of load according to UFC 3-340-02	23
Figure 3.4: DIF_c at different strain rates	24
Figure 3.5: Experimentally obtained DIFs on concrete tensile strength	26
Figure 3.6: strain-stress curve for concrete under tension at different strain rates (left: PC, right: BFSC)	26
Figure 3.7: Relation between crack opening velocity and DIF_G	27
Figure 3.8: Influence of strain rate on the Young's modulus of concrete	28
Figure 3.9: Influence of strain rate on the compressive strain	28
Figure 3.10: True stress-strain and engineering stress-strain	30
Figure 3.11: Correction of the true stress-strain curve	30
Figure 3.12: mathematical derivation of the Bridgman correction formula.	31
Figure 4.1: Flowchart for the moment-curvature relation	33

Figure 5.1: FDM beam example	36
Figure 5.2: illustration of rotational stiffness at the discrete crack	37
Figure 5.3: Secant bending stiffness	38
Figure 5.4: Change in Secant stiffness after an iteration	38
Figure 5.5: Roughly graphed F-u relationship	39
Figure 5.6: FDM for a 2D case	40
Figure 5.7: general boundary condition	40
Figure 5.8: Simply supported edge condition	41
Figure 5.9: Clamped edge condition	41
Figure 5.10: Poisson's ratio after cracking	42
Figure 6.1: Mass-spring-damper system for a beam	43
Figure 6.2: Analytical approach for a SDOF mass-spring system	45
Figure 6.3: Newton-Raphson iteration	46
Figure 6.4: Flowchart SDOF time-marching Newton-Raphson scheme	47
Figure 6.5: Used example	48
Figure 6.6: 2DOF system	48
Figure 6.7: Flowchart 2DOF time-marching Newton-Raphson scheme	51
Figure 7.1: Walls after the blast. Top wall: NRC-3. Bottom wall: NRC-4	53
Figure 7.2: Moment-curvature relationship EPR4 (dynamic) and static	54
Figure 7.3: F-u graph for NRC-4 (dynamic) and the static case	54
Figure 7.4: Comparison with the experiment	55
Figure 7.5: NLTH analyses	55
Figure 7.6: Panel 4 after the blast	56
Figure 7.7: Scaled illustration of the observations	56
Figure 7.8: M- κ graph for panel 4	57
Figure 7.9: F-u graph for panel 4	57
Figure 7.10: Deflection-time history graph of the mass-spring system	58
Figure 7.11: simplification of the nonlinear pressure distribution	59
Figure 7.12: M- κ graph for Trial 1	59
Figure 7.13: F-u graph for Trial 1	60
Figure 7.14: Unloading stiffnesses	60
Figure 7.15: Mass-spring system deflection for Trial 1	61
Figure 7.16: mass factor and load factor for Trial 1	61
Figure 8.1: Floor plan Admin Old	62
Figure 8.2: Cross section Admin Old	62
Figure 8.3: Cross section Admin Old	63

Figure 8.4: Columns in Admin Old	63
Figure 8.5: Used FEM model in the original calculation	63
Figure 8.6: Geometry of the slab (not scaled)	64
Figure 8.7: Deflection in the original results	65
Figure 8.8: reinforcement stress in the main span direction	65
Figure 8.9: Stress-strain relationship for the concrete (h=454 mm)	67
Figure 8.10: Stress-strain relationship for the reinforcement	67
Figure 8.11: Applied force in the original calculation	68
Figure 8.12: M- κ graph in the main span direction	68
Figure 8.13: M- κ graph in the secondary span direction	69
Figure 8.14: M- κ graph in the beams	69
Figure 8.15: F-u graph for the SDOF mass-spring system. On the left: total F-u. On the right: Dead weight subtracted.	70
Figure 8.16: Deflection-time history graph for the SDOF mass-spring system	70
Figure 8.17: F-u graph for the 2DOF mass-spring system	71
Figure 8.18: mass-spring system results of the case	72
Figure 8.19: F-u graph in the mass-spring system of the case	72
Figure 8.20: Variation 1.1: 12x the edge stiffness, beam mass = 1e6x cross-section mass	73
Figure 8.21: Variation 2.1: 8x the edge stiffness, beam mass = 1x cross-section mass	74
Figure 8.22: Variation 2.2: 5x the edge stiffness, beam mass = 1x cross-section mass	74
Figure 8.23: Variation 2.1: 2.5x the edge stiffness, beam mass = 1x cross-section mass	74
Figure 8.24: Variation 3.1: 5x the edge stiffness, beam mass = 0.1x cross-section mass	75
Figure 8.25: Variation 3.2: 5x the edge stiffness, beam mass = 10x cross-section mass	75

Used symbols

Roman symbols

Symbol:	Meaning:
A	Yield stress of the material under reference conditions
a	Reinforcement bar radius after necking
a	Acceleration
B	Strain hardening constant
b	Decay coefficient
C	Strengthening coefficient of strain rate
C	Damping
C_{Cr}	Critical damping
C_D	Drag coefficient
C_E	Equivalent load factor
D	Plate flexural rigidity
DIF_c	Dynamic increase factor for concrete compressive strength
DIF_E	Dynamic increase factor for concrete Young's modulus
DIF_{Gc}	Dynamic increase factor for compressive fracture energy
DIF_{Gt}	Dynamic increase factor for tensile fracture energy
DIF_t	Dynamic increase factor for concrete tensile strength
E	Young's modulus
EI	Beam flexural rigidity
EI_φ	Tangent stiffness
EI_{secant}	Secant stiffness
E_s	Reinforcement steel Young's modulus
f	Maximum concrete stress
F	Force
f_c	Maximum compressive stress
f_{cm}	Mean concrete strength
f_{dc}	Maximum dynamic concrete stress
f_{dck}	Dynamic characteristic concrete strength
f_{dcm}	Mean dynamic concrete strength
f_{dy}	Maximum dynamic reinforcement steel yield stress
f_t	Maximum tensile stress
f_y	Maximum reinforcement steel yield stress
G_c	Compressive fracture energy
G_F	Tensile fracture energy
h	Element length

h_{eq}	Equivalent element length or crack bandwidth
k	Bridgman correction factor
k	stiffness
K_L	Participating load factor
$K_{L,s}$	Participating load factor slab
K_{LM}	Participating mass-load factor
K_M	Participating mass factor
$K_{M,b}$	Participating mass factor beam
$K_{M,s,xx}$	Participating mass factor beam in x-direction
$K_{M,s,xy}$	Participating mass factor slab coupling x-direction and y-direction
$K_{M,s,yy}$	Participating mass factor beam in y-direction
L	Length
m	Thermal softening coefficient
m	Distributed bending moment
M	Concentrated bending moment
M	Mass
n	Strain hardening coefficient
p	Pressure
P_R	Reflected pressure
P_s	Overpressure
P_{so}	Peak overpressure
P_{sof}	Incident pressure on the roof
q_{of}	Dynamic pressure corresponding to CEP_{sof}
R	Range estimation
R	Radius
r	Residual force
S	Iteration factor or matrix
T^*	Homogeneous temperature
t_E	Time to yield the reinforcement
t_o	Positive phase duration
u	Displacement
v	Velocity
W	Mass of the explosive material
W	Width
w_b	Beam deflection
w_s	Slab deflection
Z	Scaled distance

Greek symbols

Symbol:	Meaning:
α	Factor
α_c	Strain parameters in parabolic compression curve
$\alpha_{c/3}$	Strain parameters in parabolic compression curve
α_j	Strain in parabolic compression curve
α_u	Strain parameters in parabolic compression curve
β	Newmark scheme parameter
γ	Newmark scheme parameter
δ	Crack opening velocity
ε	strain
$\dot{\varepsilon}^*$	Reference strain rate
$\dot{\varepsilon}_c$	Concrete strain rate
$\dot{\varepsilon}_{c,avg}$	Concrete average strain rate
$\dot{\varepsilon}_{c0}$	Reference concrete in compression strain rate
$\dot{\varepsilon}_{ct}$	Concrete in tension strain rate
$\dot{\varepsilon}_{ct0}$	Reference concrete in tension strain rate
ε_{eng}	Engineering strain
ε_{eq}	Equivalent strain
ε_j	Strain in Hordijk tension curve
$\dot{\varepsilon}_{s,avg}$	Steel average strain rate
ε_t	Strain parameter in Hordijk tension curve
ε_{true}	True strain
ε_u	Ultimate strain
ζ	Factor
κ	Curvature
ν	Poisson's ratio
ρ_{xy}	Torsion curvature
σ_{eng}	Engineering stress
σ_{true}	True stress
$\bar{\sigma}_x$	Equivalent stress
φ	Rotation
ϕ	Normalised deflection function

Abbreviations

Abbreviation:	Meaning:
2DOF	Two Degrees of Freedom
ASF	Average Strength Factor
BFSC	Blast Furnace Slag Cement
DIF	Dynamic Increase Factor
FDM	Finite Difference Method
FEM	Finite Element Method
F-u	Force-Deflection
JC	Johnson-Cook
M-κ	Moment-Curvature
NLTH	Nonlinear Time History Analysis
PC	Portland Cement
RC	Reinforced Concrete
SDOF	Single Degree of Freedom
SIF	Strength Increase Factor
TNT	Trinitrotoluene

1 Introduction

This chapter introduces the subject of the research and the reason why it should be conducted. A problem statement and research objectives are formulated. Lastly, an overview of the research is given.

1.1 Background and motivation

In 2017, Royal HaskoningDHV performed a high-level blast assessment on an office building, called 'Admin Old', at a refinery site in The Netherlands (report reference: BG8305-RHD-01-ZZ-RP-S-0002). This building is constructed in 1960 and has an in-situ cast reinforced concrete structural system. The resulting blast loads are not incorporated in the original design. The building is indicated in Figure 1.1.

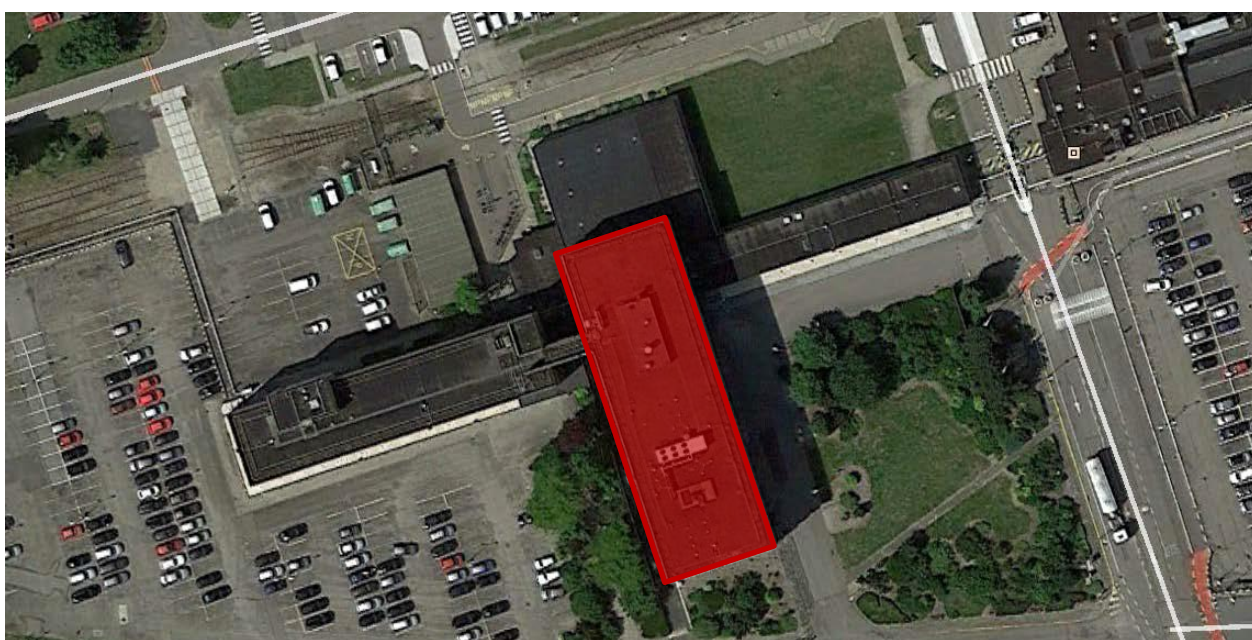


Figure 1.1: Location of Admin Old

Royal HaskoningDHV uses a 3D model of the buildings structural system existing out of 2D shells and 1D beams to analyse the building. A nonlinear time history analysis (NLTH) is performed. It is time consuming to model a complete building in finite element software and do a nonlinear analysis. Not just the modelling and running the model takes a lot of time, but also making sure the model is correct. A hand calculation can provide a good estimation of the result in a FEM analysis and is much quicker.

The purpose of the current research is to develop a quick method to analyse the building on blast load. The most convenient way to do this is to filter out members, such as a beam or a plate, of the building and analyse them individually. This research focusses on the roof of the building, which is supported by beams. By modelling it as a mass-spring system, the dynamic response can be well-captured.

A single degree of freedom (SDOF) mass-spring system represents the slab supported by stiff beams. A two degrees of freedom (2DOF) mass-spring system takes the beam deflection into account. Another reason to use a mass-spring system is to filter out the response to the first eigenmode, which is the dominating one.

An important purpose to conduct the current research is to validate the analysis of Admin Old made by Royal HaskoningDHV. This is done by analysing published experiments and use the obtained insights on the analysis of Admin Old. Experiments are mainly done on a single beam or plate instead of a building.

1.2 Problem statement

How can a two-way reinforced concrete slab with stiffened edges subjected to blast load be reduced to a SDOF or 2DOF mass-spring system in which it approximates the nonlinear behaviour of the experimentally tested slabs?

The problem statement contains much information on the focus in this research. It states that a two-way reinforced concrete (RC) slab is investigated. According to (Blaauwendraad, 2010), a slab has the following definition: "A plate subjected to a load perpendicular to its plane is in a state of bending and transverse shear. If the plate is of concrete, it is called a slab. Plates are generalizations of beams. A beam spans one direction, but a plate is able to carry loads in two directions."

The mentioning of stiffened edges implies that the slab is supported by beams. In the case study the beam and slabs are cast in-situ and are therefore fully connected. There are only two beams present, at each opposing side of the main span.

The slab is subjected to blast load. This is a time varying load, which goes by in less than a second. Although the duration of the blast load is short, it cannot be treated as an instantaneous impact load. In certain cases, the maximum deflection might occur before the complete blast wave has arrived at the slab. This is not the case for an instantaneous impact load.

The slab is reduced to a single-degree of freedom (SDOF) mass-spring system or a two-degree of freedom (2DOF) mass-spring system. The difference is that for a SDOF mass-spring system the edges with beams are supposed to act as vertically fixed supports, whereas in a 2DOF mass-spring system the beams have a vertical motion.

The mass-spring system should approximate the nonlinear behaviour of the concrete. This is because in blast analysis, the maximum load acting on the slab is so high that damage is expected. In fact, in many cases the design goal in such analysis is to avoid collapsing of the building, meaning that severe damage is allowed. Therefore, an elastic blast analysis is less common than a plastic analysis.

Lastly, the mass-spring system should match existing experiments. The theory on the material models, dynamic effects and response are tested on published experiments. The applied analysis method is then calibrated where needed.

1.3 Research objective

The goal is to find a method to accurately predict the nonlinear dynamic behaviour of the element. This method should be able to replace the time consuming NLTH analyses with a detailed FEM model, while remaining the accuracy of such analyses. This is achieved by verifying the used method with FEM analyses and calibration with published experiments. The flowchart in Figure 1.2 and the explanation below the figure further clarifies the verification process of the used method.

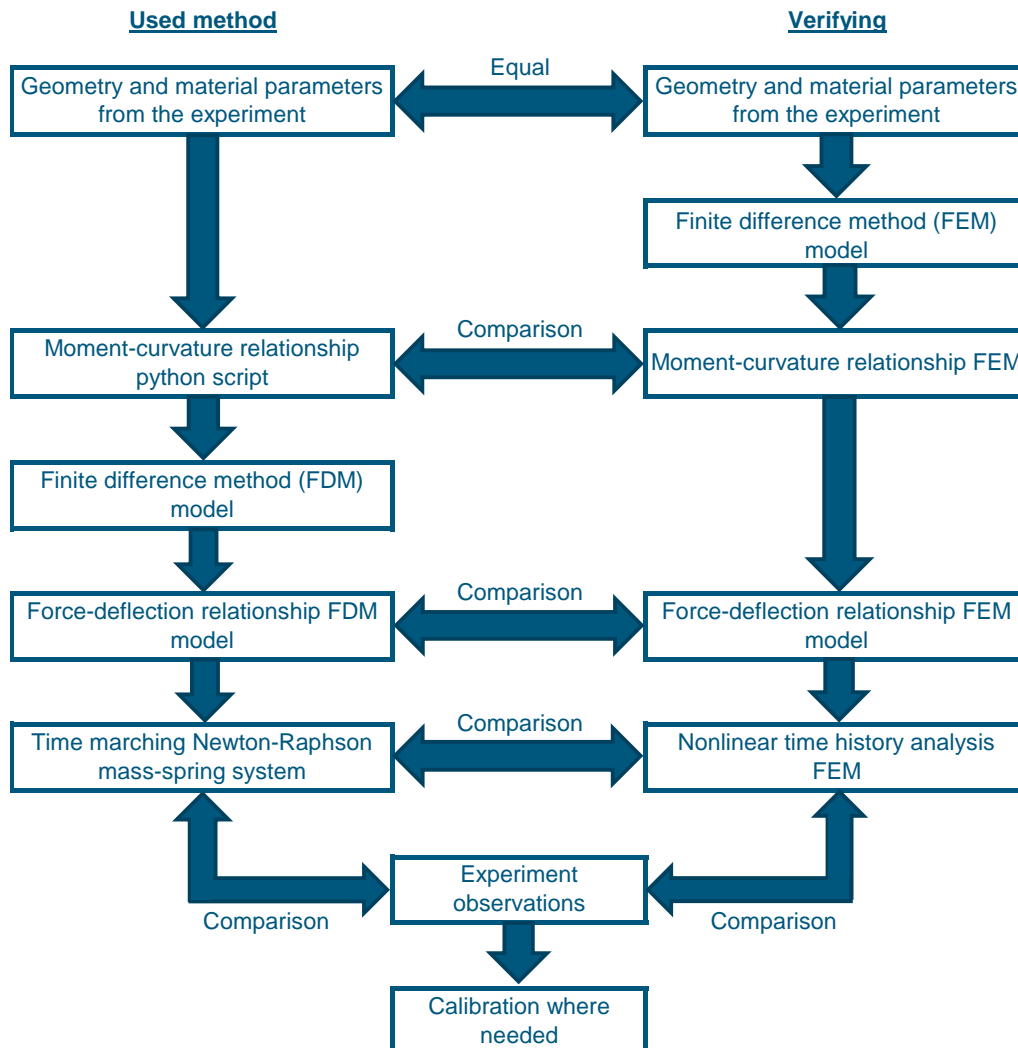


Figure 1.2: Flowchart of the experiment calibration

Validation process:

1. The material properties under blast load conditions are substantiated by a literature study.
2. A moment-curvature (M- κ) relationship is manually constructed based on the material properties. A python script is written to achieve this. The python script incrementally increases the curvature and finds force balance after each curvature increase step. The M- κ relationship is compared with the one found in a finite element method (FEM) model.
3. The M- κ is used as input for the finite difference method (FDM) model. This model solves the beam equation or slab equation numerically. Another two python scripts are written for the FDM beam model and the FDM slab model. The load is incrementally increased while storing the previous nodal deflections. Two things are extracted from the results of the FDM model: the force-deflection (F-u) relationship of the mid-point of the beam or slab and the participating mass and load factors.
4. The F-u graph and participating mass and load factors are input for the single degree of freedom (SDOF) mass-spring system or the two degrees of freedom (2DOF) mass-spring system. There is no incremental procedure in the mass-spring system. Therefore an iterative Excel spreadsheet is convenient to use. A time marching Newton-Raphson iteration procedure is used. The results of the mass-spring system are compared with experiments. Adjustments are made where necessary.

1.4 Report structure

The report structure follows the design steps to be followed for a blast analysis. Chapter 2 explains what a blast load is. The cause of an explosion is addressed. Once the explosion has occurred, a blast wave propagates through the air. This is called the free field blast. When the blast wave arrives at the structure, the blast wave gets disturbed by the presence of the structure.

Chapter 3 describes the material parameters to be used in blast analysis. The main component in this chapter is the dynamic increase factor. The dynamic increase factor is the strength increase of a material under rapid loading conditions.

The method of analysing the slab to a blast load is described in chapter 4, chapter 5, and chapter 6. Chapter 4 describes the cross-sectional behaviour. In this research, the cross-sectional behaviour is characterised by the moment-curvature relationship. Chapter 5 is about the static behaviour of the element. First, the FDM is conceptually explained. After that, it goes more in-depth on the application on a one-way element and two-way elements. The results of the FDM are the F-u graph and the participating mass and load factors. Chapter 6 is about the dynamic behaviour. The mass-spring-damper system specifically for blast analysis on one-way elements or two-way elements is addressed. Then the equation of motion and the solution of it are described for the SDOF mass-spring system and the 2DOF mass-spring system.

The results are presented in chapter 7 and chapter 8. Chapter 7 gives a summarised version of Appendix I, Appendix II and Appendix III. In these appendices the experiments are presented, analysed, and discussed. In chapter 8, the obtained insights into the dynamic blast analysis on one-way elements and two-way elements are applied on the roof of Admin Old. This case study is expanded by a parametric study, where the influence of the supporting beams is investigated.

The results are discussed in chapter 9. Conclusions are drawn in chapter 10 followed by the recommendations.

2 Blast load

In this chapter the definition of a blast load is given. The mechanics of an explosion are briefly discussed. Once an explosion has occurred, the blast wave travels through the air. The pressure of the wave front has a characteristic shape in time. At some point it reaches the building, which interacts in the blast wave.

2.1 Mechanics of an explosion

Every molecule has a certain amount of chemical potential energy stored within the bonds between its atoms. Chemicals with more potential energy are less stable and thus more likely to react. This does not necessarily mean that the chemical will explode after the reaction. This depends on the speed of the reaction and the activation energy.

Usually, a trigger is needed to activate the chemical reaction, unless the chemical is extremely unstable. A log of wood, for example, has enough chemical potential energy to start burning after igniting it. Yet, the log will not explode, while TNT, with less chemical potential energy than the log of wood, will explode after being ignited. This is because the speed of the chemical reaction is much faster than that of the log of wood. To put it in numbers: the log has a chemical potential energy of 15.5 MJ/kg and a reaction speed of 0.3 m/s. TNT has a chemical potential energy of 4.184 MJ/kg and a reaction speed of 6900 m/s.

Not all explosive materials will explode after being ignited. An example is C-4, which is commonly used in the military. C-4 is very stable for an explosive material. It can safely be lit on fire without the risk of exploding. This is because C-4 needs more input energy than TNT to initiate the explosion, a combination of heat and shock. The energy needed to initiate the explosion is the activation energy. Activation energy is the energy barrier that must be overcome to start the chemical reaction, as illustrated in Figure 2.1. The higher the activation energy, the slower the chemical reaction. This is because, probability wise, fewer molecules can overcome the energy barrier.

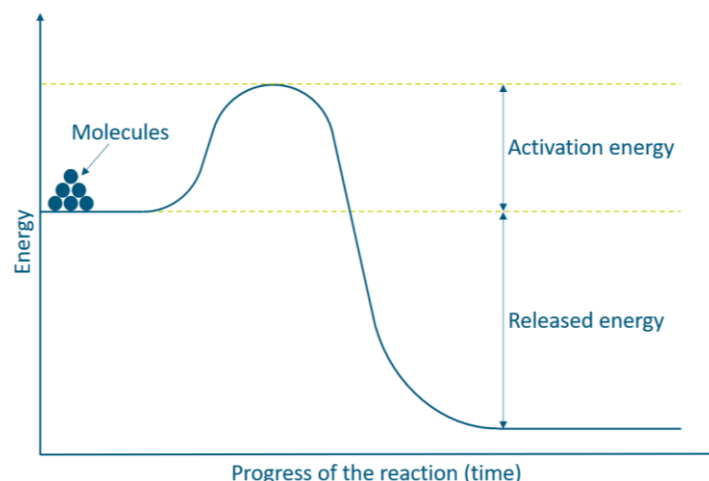


Figure 2.1: Energy path of molecules through the reaction progress

Lowering the activation energy can be done in two ways and are shown in Figure 2.2. The first method is by adding a catalyst to the chemical. This is mainly used in chemistry and biology, not necessarily to trigger an explosion. The second method is more usual for detonating a stable explosive material. To trigger the explosion, a detonator is used. A detonator gives an initial activation energy, which lowers the energy barrier enough to initiate the explosion.

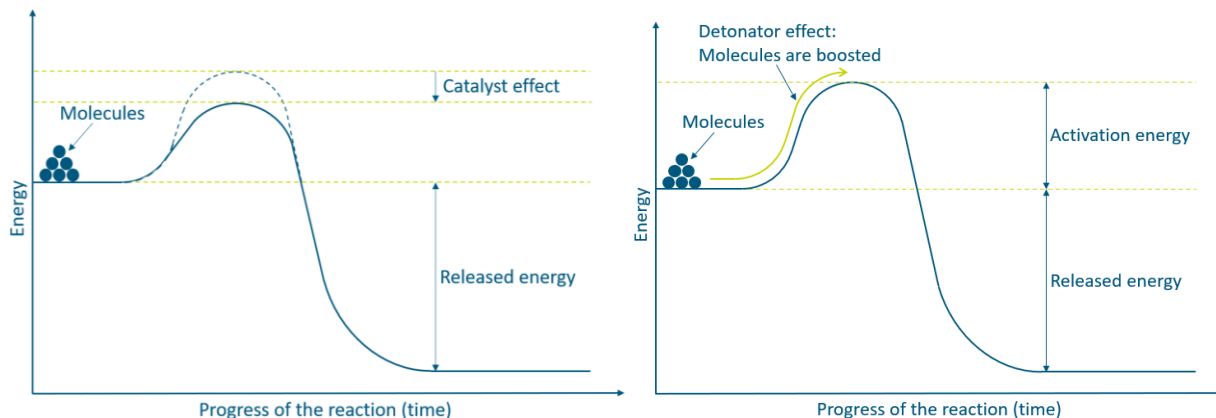


Figure 2.2: Tools to lower the activation energy

2.2 Effects of an explosion

Once the explosion has started, a large amount of energy is released, and the volume of the explosive material rapidly expands to a significantly larger volume. This heats up and pushes surrounding gas particles in form of a wave. The waves propagate because the molecules bump into each other and thereby transfer the pressure change. Flames are created due to combustion of the explosive material in air. In a combustion process, a distinction is made between a detonation and deflagration. The difference is the speed of the chemical reaction. A detonation is characterised by a supersonic flame velocity (> 343 m/s). Lower flame velocities are deflagrations. Usually, a detonation (Figure 2.3, left) is a more powerful explosion than a deflagration (Figure 2.3, right). Generally, detonations occur due to the explosion of solid explosives and deflagrations due to gas explosions, according to (Ministerie van Verkeer en Waterstaat, 2003).

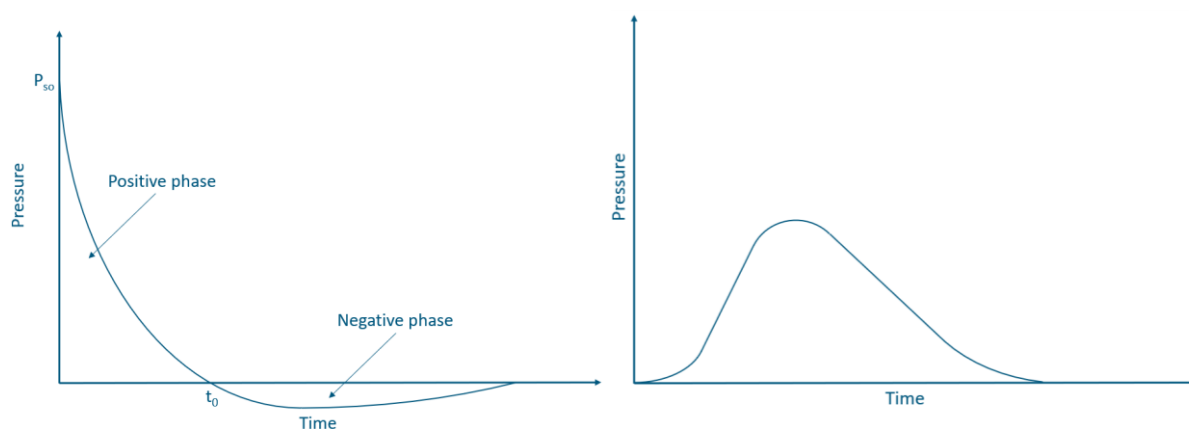


Figure 2.3: Free field pressure for detonations (left) and deflagrations (right)

The general term for the wave resulting from detonations and deflagration is blast wave. In this research, blast wave coming from a detonation is examined.

2.3 Interaction between blast and structure

The blast wave can freely propagate in the air if there are no obstacles in the way. Once the blast wave encounters an obstacle, such as a building or the ground, it starts interfering the wave. The incoming wave is called the incident wave. After reaching the façade of a building the wave gets reflected. The reflection of the wave leads to a higher, or at least equal, pressure. This is illustrated in Figure 2.4.

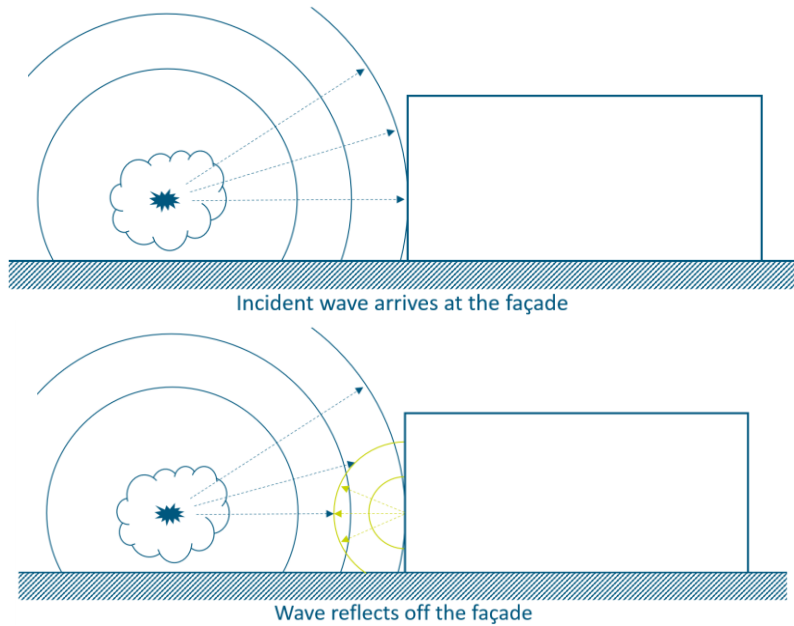


Figure 2.4: Blast wave interaction with the building (interaction with the ground not included)

The pressure of the blast wave front is characterised by a positive phase and a negative phase. The positive phase is of short duration but contains most of the energy. In practice the negative phase is neglected, and the positive phase is described as (2.1) or approximated by an equivalent triangular function. Equation (2.1) is also known as the Friedlander waveform.

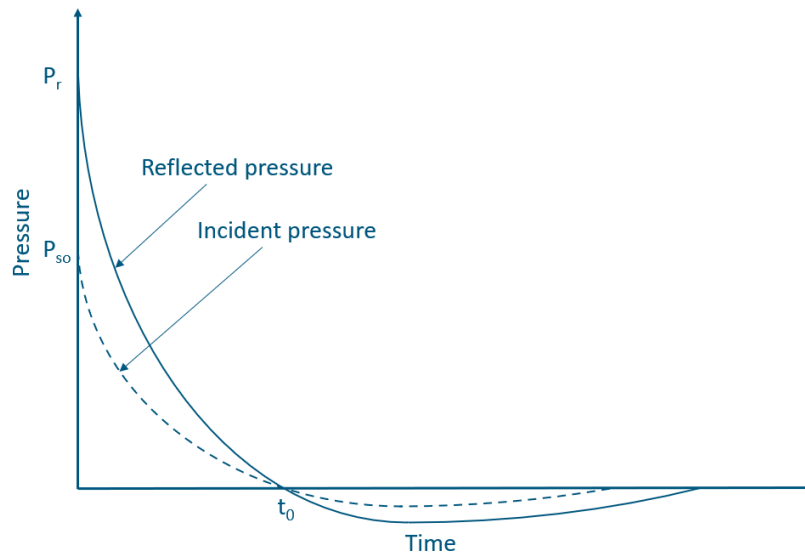


Figure 2.5: Typical pressure function for blast analysis

$$P_s(t) = P_{so} \left(1 - \frac{t}{t_0}\right) e^{-b\frac{t}{t_0}} \quad (2.1)$$

Where:

- P_{so} is the peak overpressure
- t_0 is the positive phase duration
- b is the decay coefficient

The destructive effect of a blast load on a building depends on the following factors, according to UFC 3-340-02 (Department of Defence, US, 2008):

1. Explosive properties, namely type of explosive material, energy output (high or low order detonation), and weight of explosive.
2. The location of the detonation relative to the protective structures.
3. The magnitude and reinforcement of the pressure by its interaction with the ground barrier, or the structure itself.

Explosive properties

Explosive materials can come in solid form, liquid form or gaseous form. The blast effects of solid explosives are best known and are primarily high explosives, according to UFC 3-340-02 (Department of Defence, US, 2008). Figure 2.5 holds for supersonic explosions created by high-explosive solid materials. These types of explosions result in the governing load on the structure. The mass and potential chemical energy of the material defines the strength of the blast load. However, not every type of explosive has the same density. It is convenient to relate each type of explosive to one reference. This is called the TNT equivalency (trinitrotoluene). TNT has a mass density of 1.60 g/ml.

Reinforcement of the incident wave

As Figure 2.5 shows, the reflected wave is stronger than the incident wave. Under perfect linear-elastic circumstances the particles of the incident wave arrive at the obstacle and bounces off with the same pressure as the pressure of the incident wave. This doubles the pressure in the region where the incident wave and reflected wave coincide. However, the reflected molecules are distorted in the transfer region which reinforces the reflecting wave pressure.

Location of the detonation

The distance of the detonation to the structure defines the strength of the load acting on the structure. This distance is well described by the Hopkinson-Cranz scaling law (2.2).

$$Z = \frac{R}{W^{1/3}} \quad (2.2)$$

Where:

R = Range estimation

Z = Scaled distance

W = mass of the explosive material

The vertical distance is relevant for the ground interaction with the blast wave. There are three categories of explosions relating the vertical distance to the ground. UFC 3-340-02 gives the following descriptions:

1. Free air burst: When a detonation occurs adjacent to and above a protective structure such that no amplification of the initial shock wave occurs between the explosive source and the protective structure, then the blast loads acting on the structure are free-air blast pressures

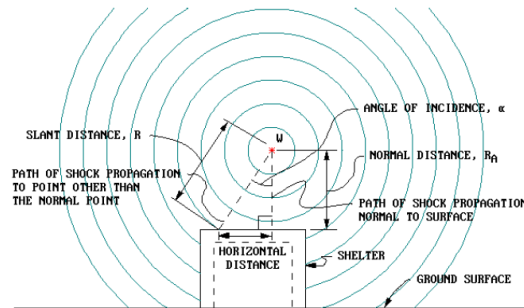


Figure 2.6: Free air burst

2. Air burst: The air burst environment is produced by detonations which occur above the ground surface and at a distance away from the protective structure so that the initial shock wave, propagating away from the explosion, impinges on the ground surface prior to arrival at the structure. As the shock wave continues to propagate outward along the ground surface, a front known as the Mach front is formed by the interaction of the initial wave (incident wave) and the reflected wave. This reflected wave is the result of the reinforcement of the incident wave by the ground surface.

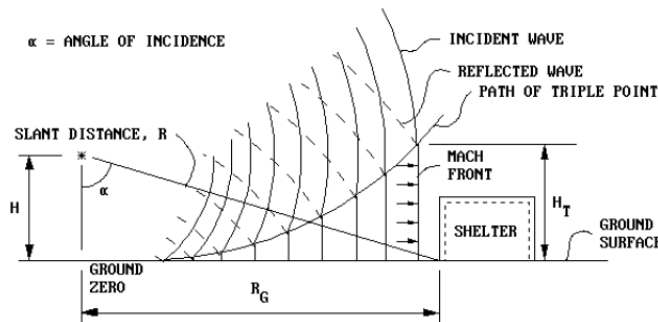


Figure 2.7: Air burst

3. Surface burst: A charge located on, or very near the ground surface, is considered to be a surface burst. The initial wave of the explosion is reflected and reinforced by the ground surface to produce a reflected wave. Unlike the air burst, the reflected wave merges with the incident wave at the point of detonation to form a single wave, similar in nature to the free air burst but essentially hemispherical in shape.

Figure 2-14 Surface Burst Blast Environment

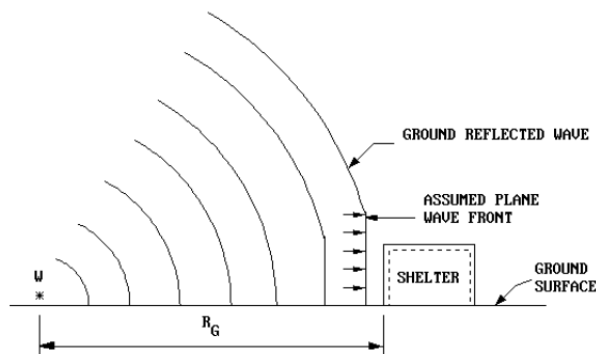


Figure 2.8: Surface air burst

2.4 Force acting on a roof

As the blast wave propagates through the air, the pressure encloses the structure. The peak pressure arrives directly at the front façade which receives the greatest load. The pressure on the roof gradually builds up as the wave front needs time to propagate over the roof. The peak pressure on the roof is lower than the peak reflected pressure that arrives at the front façade. Also, the wavelength of the characteristic pressure function on the roof is larger than for the front façade (UFC 3-340-02). Figure 2.9 illustrates the pressure function on a roof.

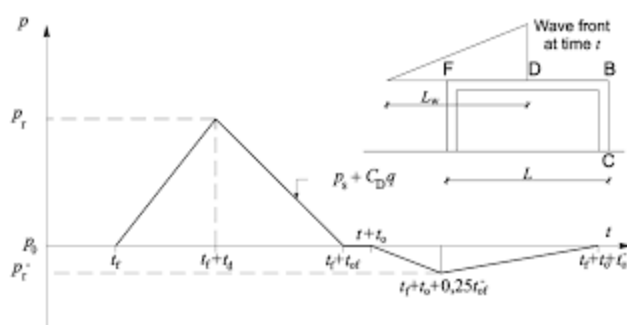


Figure 2.9: Simplified pressure function on a roof

UFC 3-340-02 describes the pressure function as follows:

$$P_R = C_E P_{sof} + C_D q_{of} \quad (2.3)$$

Where:

- P_{sof} is the incident pressure at point F
- C_E is the equivalent load factor
- C_D is the drag coefficient
- q_{of} is the dynamic pressure corresponding to $C_E P_{sof}$

2.5 Far field and near field explosions

The failure mechanism of a structure depends on the scaled distance Z . Experiments have shown that below a certain value the explosion can be categorised as near field, while above this value the explosion is considered as far field. UFC3-340-02 sets this boundary on $1.2 \text{ m/kg}^{1/3}$. Anything above that failure tends to have flexural failure. Scaled distances between $0.4 \text{ m/kg}^{1/3}$ and $1.2 \text{ m/kg}^{1/3}$ can have either or both local and flexural failure but are classified as near field. Scaled distances below $0.4 \text{ m/kg}^{1/3}$ will most likely fail on local failure.

Local failure of a concrete slab is hard to simulate in a finite element model and to express in a mass-spring system. Software packages with explicit solver should be used to capture local failure.

Besides the modelling complexity, near field explosions are less relevant for roof slabs because it is unlikely that the explosion happens on or close to the roof. Because of the reason only far field explosions are considered in this research.

3 Material behaviour

Materials behave differently under dynamic loads. This has to do with the speed at which the load is applied. The dynamic material properties are increased by the strength increase factor (SIF) and the dynamic increase factor (DIF), as (3.1) and (3.2) are formulating.

$$f_{dc} = SIF \cdot DIF \cdot f_c \quad (3.1)$$

$$f_{dy} = SIF \cdot DIF \cdot f_y \quad (3.2)$$

3.1 Static material models

The material stress-strain relationships used in this research are based on the static material behaviour. They are obtained by applying the load slowly on a specimen. Typically, a softening or hardening branch is found after reaching the maximum stress of the material. The used material models are mainly based on RTD 1016-1:2020 (Hendriks & Roosen, 2020) and experience of Royal HaskoningDHV.

3.1.1 Concrete

The stress-strain relationship of concrete in compression is based on the parabolic curve (3.3). The area under the compression curve is the amount of energy that can be absorbed. This area is in literature referred to as the concrete compressive fracture energy or the energy absorption capacity and denoted as G_c . The maximum compressive strength is denoted as f_c .

$$f = \begin{cases} -f_c \frac{1}{3} \frac{\alpha_j}{\alpha_{c/3}} & \text{if } \alpha_{c/3} < \alpha_j \leq 0 \\ -f_c \frac{1}{3} \left(1 + 4 \left(\frac{\alpha_j - \alpha_{c/3}}{\alpha_c - \alpha_{c/3}} \right) - 2 \left(\frac{\alpha_j - \alpha_{c/3}}{\alpha_c - \alpha_{c/3}} \right)^2 \right) & \text{if } \alpha_c < \alpha_j \leq \alpha_{c/3} \\ -f_c \left(1 - \left(\frac{\alpha_j - \alpha_c}{\alpha_u - \alpha_c} \right)^2 \right) & \text{if } \alpha_u < \alpha_j \leq \alpha_c \\ 0 & \text{if } \alpha_j \leq \alpha_u \end{cases} \quad (3.3)$$

$$\alpha_{c/3} = -\frac{1}{3} \frac{f_c}{E} \quad (3.4)$$

$$\alpha_c = 5\alpha_{c/3} \quad (3.5)$$

$$\alpha_u = \alpha_c - \frac{3}{2} \frac{G_c}{hf_c} \quad (3.6)$$

The stress-strain relationship for concrete in tension is based on the Hordijk curve (3.7). The softening curve is based on the tensile fracture energy G_F . Concrete is a brittle material, but the tensile strength is not completely gone after cracking. The post-cracking behaviour of concrete under tension is called the tension softening curve. Defining this curve is necessary for an accurate cracking model. Besides that, defining the tension softening curve usually benefits the nonlinear analysis, because the decline of the fracture tensile stress down to 0 runs smoothly.

$$f = \begin{cases} f_t \frac{\varepsilon_j}{\varepsilon_t} & \text{if } 0 < \varepsilon_j \leq \varepsilon_t \\ f_t \left(1 + \left(3.0 \frac{\varepsilon_j}{\varepsilon_u} \right)^3 \exp(-6.93 \frac{\varepsilon_j}{\varepsilon_u}) - \frac{\varepsilon_j}{\varepsilon_u} (1 + 3.0^3) \exp(-6.93) \right) & \text{if } \varepsilon_t < \varepsilon_j \leq \varepsilon_u \\ 0 & \text{if } \varepsilon_j > \varepsilon_u \end{cases} \quad (3.7)$$

$$\varepsilon_u = 5.136 \frac{G_F}{h_{eq} f_t} \quad (3.8)$$

The stress-strain relationship of concrete is illustrated in Figure 3.1. This is the input of the parabolic concrete compression curve and the Hordijk concrete tension curve according to the DIANA manual. A popular way of implementing cracks in a FEM model is by use of a smeared cracking model. In smeared cracking models, the input for the tensile fracture energy depends on the crack bandwidth. This should be considered when using smeared cracking models.

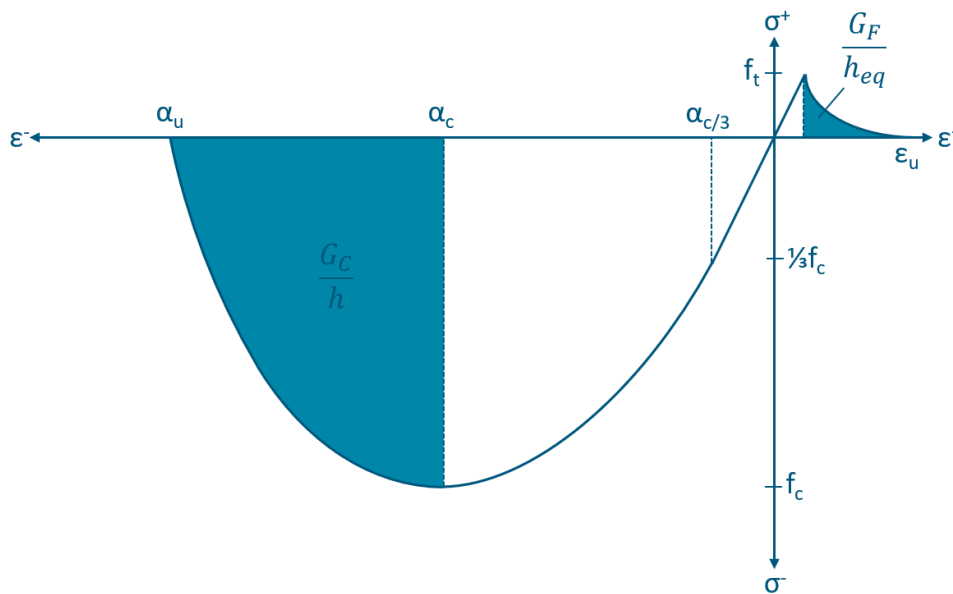


Figure 3.1: Stress-strain relationship for concrete in FEM analysis

3.1.2 Reinforcement steel

Figure 3.2 schematises the stress-strain relationship for reinforcement steel. The tension hardening branch is simplified by a straight line. The values for the distinct points in the graph are given in the design codes NEN-EN 1992-1-1 (Normcommissie 351 001 "Technische Grondslagen voor Bouwconstructies", 2011) and Model Code 2010 (Fédération internationale du béton (fib), 2013).

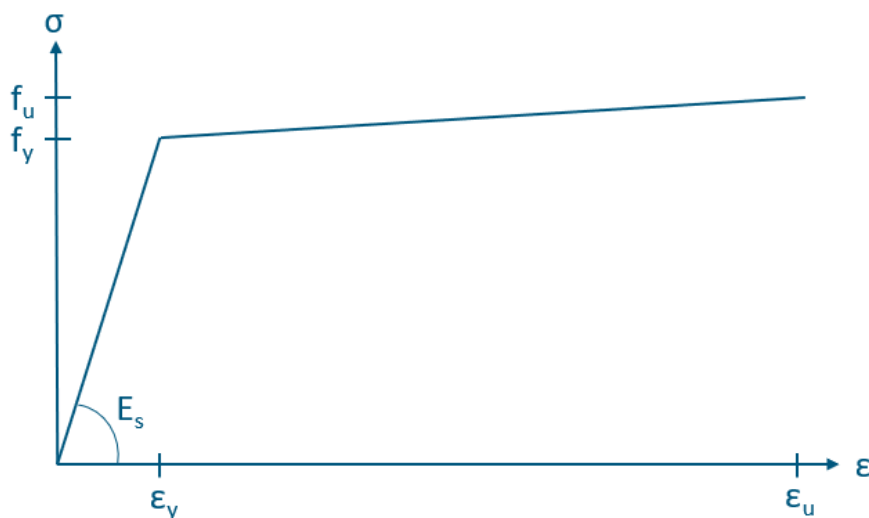


Figure 3.2: Stress-strain relationship for reinforcement steel

3.2 Static strength increase

A static increase factor (SIF) is applied on the nominal strength of the material. The SIF is also called the Average strength factor (ASF). Usually, this only applies to structural steel because commonly the minimum required strength of the material is specified. The mean strength is higher. The UFC 3-340-02 suggests using a SIF of 1.1 on reinforcement steel.

The regular design codes do not give a value for the mean yield strength f_{ym} of the reinforcement steel. The probabilistic model code (Joint Committee on Structural Safety, 2001) published by the Joint Committee on Structural Safety provides statistical parameters for reinforcement steel. The standard deviation is given as 30 MPa. Considering the fact that the characteristic value corresponds with a probability of 5%, the mean yield strength must be 550 MPa according to the normal distribution. This corresponds with the suggested value of 1.1 by UFC3-340-02. The factor between the ultimate strength and the yield strength is 1.08, according to the design codes Model Code 2010 and NEN-EN 1992-1-1.

3.3 Dynamic strength increase

Material parameters used in designing a structure usually represent the static parameters. These parameters are determined in experiments on specimens loaded relatively slow. This falls into the category 'Quasi-static' in Figure 3.3. When a material is loaded much faster, the strength and ductility of the material might increase. The increase of strength depends on the strain rate and is usually called the DIF. This is something to consider when designing a structure subjected to blast load. MC2010 gives recommendations for the DIF's for concrete and reinforcement steel. These are based on papers that are cited in this chapter.

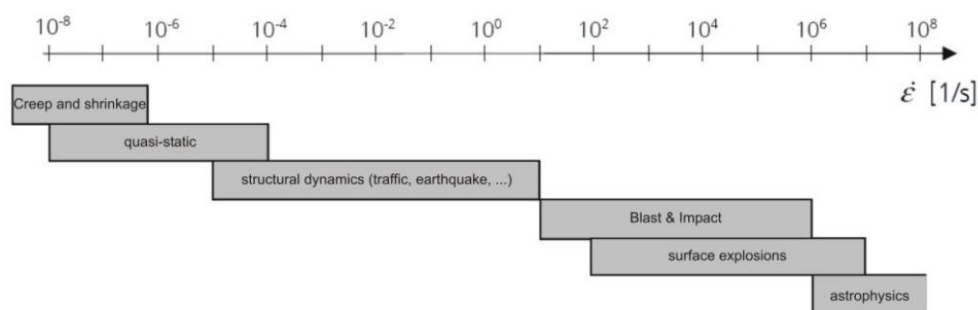


Figure 3.3: strain rate ranges for different types of load according to UFC 3-340-02

UFC 3-340-02 advises similar values for the DIF's as Model Code 2010. The big difference is that UFC 3-340-02 defines the DIF as the mean dynamic strength over the mean static strength. Whereas the MC2010 defines the DIF as the characteristic dynamic strength over the mean static strength. This is shown further on in this chapter. For simulating experiments with an engineering tool, the mean values must be taken as this should lead to a better approximation of the experimental results. For design purposes the characteristic values are more appropriate. UFC 3-340-02 helps the engineer in choosing an appropriate DIF by providing a table with DIF's. This table is rather conservative but useful for quick calculations. It is difficult to predict the DIF beforehand since the strain rate is usually required. The strain rate follows from the analysis and in theory changes throughout the analysis. However, adjusting the DIF based on the strain rate after each load-step in a non-linear time analysis is too detailed and hard to prove whether it is the correct way to approach the analysis. An average value for the strain rate should be taken to calculate the DIF's. UFC 3-340-02 provides a formulation of the average strain rate, namely (3.9) for concrete and (3.10) for reinforcement steel. The time to yield the reinforcement is denoted as t_{ϵ} . (3.9) is based on the concrete compressive stress being reached at a strain of 0.002.

$$\dot{\epsilon}_{c,avg} = 0.002/t_E \quad (3.9)$$

$$\dot{\epsilon}_{s,avg} = f_{dy}/(E_s t_E) \quad (3.10)$$

3.3.1 Concrete compressive strength

The DIF on the compressive strength (DIF_c) in both Model Code 2010 and UFC 3-340-02 is based on (Bischoff & Perry, 1991). The base formula for the DIF_c is given in (3.11), (3.12) and (3.13). Bischoff and Perry assembled data from existing studies taking into account the difference in compressive strength of the concrete specimen. They found a correlation between the strain rate and the DIF_c with a correction for the concrete compressive strength. Figure 3.4 is adopted from (Bischoff & Perry, 1991). The figure is plotted in log-log scale. Three lines are drawn in the figure: one for $f_c=20$ MPa, one for $f_c=50$ MPa and one for $f_c=90$ MPa. The first two are already included in the figure, the latter is what Model Code 2010 recommends. The graph of $f_c=50$ MPa is the one that UFC 3-340-02 recommends.

$$DIF_c = \begin{cases} (\dot{\epsilon}_c/\dot{\epsilon}_{c0})^{1.026\alpha} & \text{for } \dot{\epsilon}_c \leq 30 \text{ s}^{-1} \\ \gamma(\dot{\epsilon}_c)^{1/3} & \text{for } \dot{\epsilon}_c > 30 \text{ s}^{-1} \end{cases} \quad (3.11)$$

$$\dot{\epsilon}_{ct0} = 30 \cdot 10^{-6} \text{ s}^{-1} \quad (3.12)$$

$$\alpha = (5 + 3f_{cu}/4)^{-1} \quad (3.12)$$

$$\gamma = 6.156\alpha - 0.492 \quad (3.13)$$

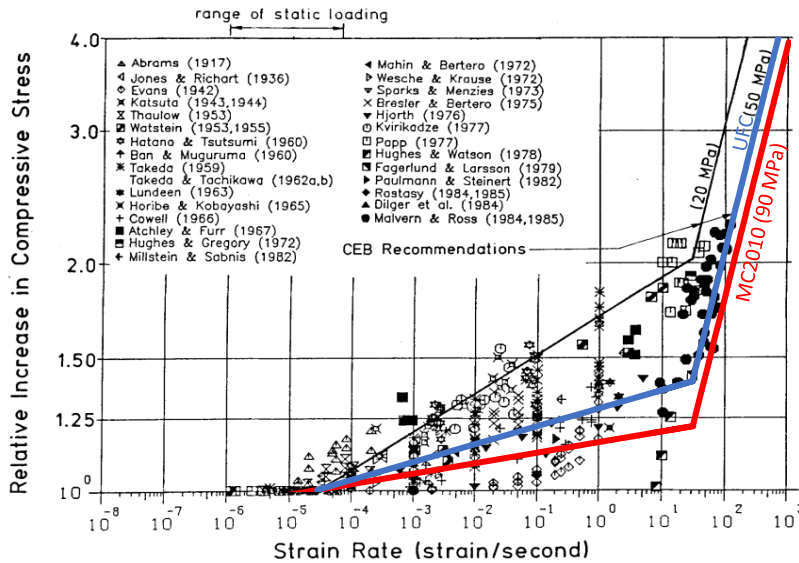


Figure 3.4: DIF_c at different strain rates

The recommended value for the DIF_c by UFC 3-340-02 is formulated in (3.14). The compressive strength of 50 MPa is predetermined as the value for α is already filled in. The DIF_c in the UFC 3-340-02 is defined as the dynamic mean compressive strength over the static mean compressive strength.

$$DIF_c = \frac{f_{dcm}}{f_{cm}} = \begin{cases} (\dot{\epsilon}_c/\dot{\epsilon}_{c0})^{0.024} & \text{for } \dot{\epsilon}_c \leq 30 \text{ s}^{-1} \\ 0.45(\dot{\epsilon}_c)^{1/3} & \text{for } \dot{\epsilon}_c > 30 \text{ s}^{-1} \end{cases} \quad (3.14)$$

$$\dot{\epsilon}_{ct0} = 30 \cdot 10^{-6} \text{ s}^{-1}$$

The recommended value for the DIF_c by Model Code 2010 in (3.15) is different formulated. It is defined as the dynamic characteristic compressive strength over the static mean compressive strength. The α value

is determined based on a compressive strength of 90 MPa. As seen in Figure 3.4 the line that represents the compressive strength of 90 MPa is slightly off the data points. This is because Model Code 2010 directly gives the designing value for the compressive strength.

$$DIF_c = \frac{f_{dck}}{f_{cm}} = \begin{cases} (\dot{\epsilon}_c / \dot{\epsilon}_{ct0})^{0.014} & \text{for } \dot{\epsilon}_c \leq 30 \text{ s}^{-1} \\ 0.012(\dot{\epsilon}_c / \dot{\epsilon}_{ct0})^{1/3} & \text{for } \dot{\epsilon}_c > 30 \text{ s}^{-1} \end{cases} \quad (3.15)$$

$$\dot{\epsilon}_{ct0} = 30 \cdot 10^{-6} \text{ s}^{-1}$$

3.3.2 Concrete compressive fracture energy

Many studies are focussing on DIF of the compressive strength, while only a few studies also paid attention to the energy absorption capacity. (Bischoff & Perry, 1991) dedicated a short chapter on the energy absorption capacity and concluded the following: “ (Watstein, 1953) measured energy absorption increases of up to 120% for a strain rate of about 10 s^{-1} (which was larger than the corresponding 85% increase in compressive strength), while (Takeda & Tachikawa, 1962) reported an increase between 20 and 80% for a strain rate of 1 s^{-1} (also greater than the corresponding increase in compressive strength). An increase between 37 and 42% was observed by (Atchley & Furr, 1967) for several strengths of concrete at a loading rate of about 3 s^{-1} .”

Considering this information, it is safe to assume that the DIF on the energy absorption capacity (DIF_{Gc}) is around the same value as DIF_c .

3.3.3 Concrete tensile strength

Concrete under tension is highly dependant on the strain rate. (Schuler et al., 2006) assembled existing experiments of concrete specimens in one paper. Figure 3.5 is one of the results he obtained in his research. It is clear that an exponential relation between the strain rate and the DIF is present. The DIF gets larger for strain rates above 10 s^{-1} , corresponding with impact load or near-field explosions. This range is strain rate is outside the scope of this research. The area of interest is indicated in Figure 3.5. The UFC 3-340-02 recommended DIF for concrete under tension (DIF_t) (3.16) has good agreement with the experimental data, whereas the graph belonging to the Model Code 2010 recommendation is shifted conservatively. This equation is given in (3.17). Unlike Figure 3.4, the vertical axis in Figure 3.5 is not in a logarithmic scale.

$$DIF_t = \begin{cases} (\dot{\epsilon}_{ct} / \dot{\epsilon}_{ct0})^{0.03} & \text{for } \dot{\epsilon}_{ct} \leq 10 \text{ s}^{-1} \\ 0.015(\dot{\epsilon}_{ct} / \dot{\epsilon}_{ct0})^{1/3} & \text{for } \dot{\epsilon}_{ct} > 10 \text{ s}^{-1} \end{cases} \quad (3.16)$$

$$\dot{\epsilon}_{ct0} = 1 \cdot 10^{-6} \text{ s}^{-1}$$

$$DIF_t = \begin{cases} (\dot{\epsilon}_{ct} / \dot{\epsilon}_{ct0})^{0.018} & \text{for } \dot{\epsilon}_{ct} \leq 10 \text{ s}^{-1} \\ 0.0062(\dot{\epsilon}_{ct} / \dot{\epsilon}_{ct0})^{1/3} & \text{for } \dot{\epsilon}_{ct} > 10 \text{ s}^{-1} \end{cases} \quad (3.17)$$

$$\dot{\epsilon}_{ct0} = 1 \cdot 10^{-6} \text{ s}^{-1}$$

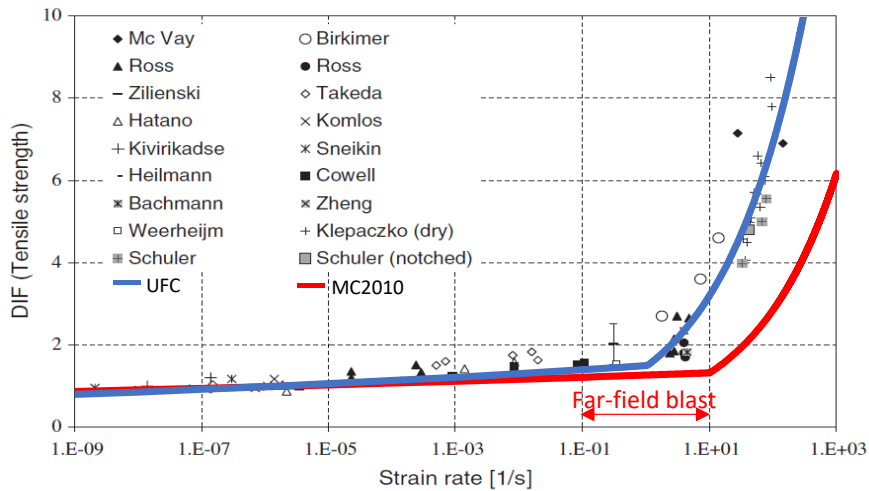


Figure 3.5: Experimentally obtained DIFs on concrete tensile strength

3.3.4 Tensile fracture energy

There are many studies and experiments done on the post-cracking behaviour of concrete. In many studies an exponentially decreasing curve is found. However, this does not necessarily mean that such a curve still holds for concrete under high strain rate. (Vegt & Weerheijm, 2016) studied the effect of dynamic strain rates on the tensile strength and fracture energy. Two types of concrete mixtures are presented in the paper, Portland cement (PC) concrete and Blast Furnace Slag cement (BFSC) concrete. Both types of concrete are tested under three conditions: normal, wet, and dry. Only the results under normal conditions are presented in this research. This is representative for the used experiments and the used case study. Figure 3.6 shows two graphs from (Vegt & Weerheijm, 2016) that show the influence of strain rate on the tensile behaviour of concrete. Table 3.1 gives the DIF's on the tensile strength and fracture energy. For strain rates around 1 1/s the tensile curve follows a similar trajectory as the curve obtained under static conditions. The tensile strength increases significantly, while the fracture energy does not change much. For strain rates higher than 40 1/s the trajectory is different. The post-cracking branch is still descending but the material keeps its tensile strength for much longer compared to the lower strain rates. The DIF on the fracture energy is higher than the DIF on the tensile strength.

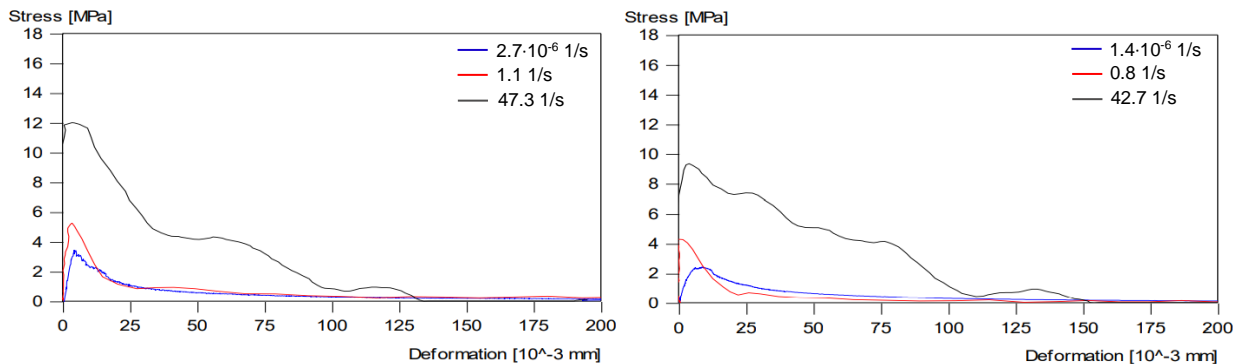


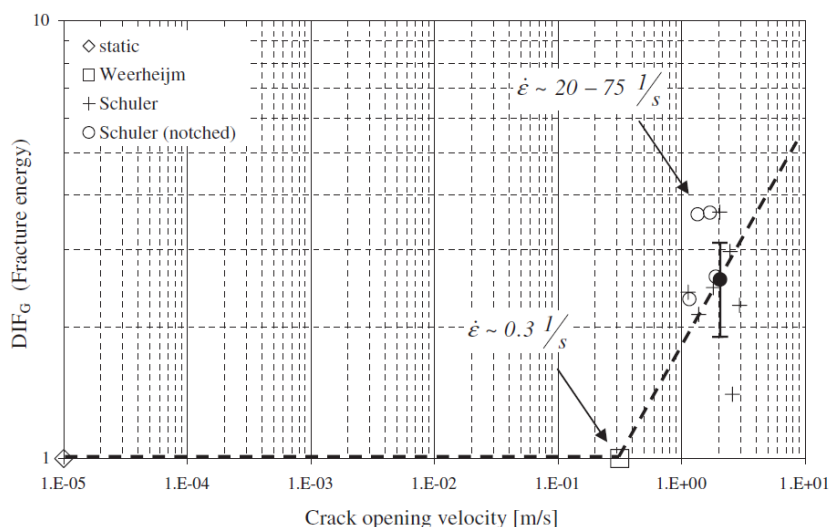
Figure 3.6: strain-stress curve for concrete under tension at different strain rates (left: PC, right: BFSC)

Table 3.1: DIF_t and DIF_G high strain rates (Vegt & Weerheijm, 2016)

Type of concrete	Strain rate [1/s]	DIF_t	DIF_G
Portland cement	1.1	1.7	1.1
	47.3	3.3	4.6
Blast Furnace Slag cement	0.8	1.6	1.0
	42.7	3.9	5.1

The observation that the DIF_G barely increases at the strain rates around 1 s^{-1} and increases much more at higher strain rates is in line with Figure 3.7. This figure is from (Schuler et al., 2006) and shows the correlation between the crack opening width and DIF_G . Based on the dashed line Schuler proposed (3.18) for the dependence of the specific fracture energy from the crack opening velocity. The DIF_G is taken as 1.0 in this research. Based on (Schuler et al., 2006) and (Vegt & Weerheijm, 2016), this is considered reasonable for strain rates between 10^{-1} and 10^1 .

$$DIF_G = \begin{cases} 1 & \text{for } \dot{\delta} \leq 0.33 \text{ m/s} \\ 1.74 \cdot \dot{\delta}^{0.5} & \text{for } \dot{\delta} > 0.33 \text{ m/s} \end{cases} \quad (3.18)$$

Figure 3.7: Relation between crack opening velocity and DIF_G

Little is known about the DIF_G apart from the cited studies in this chapter. Model Code 2010 states the following on the DIF_G : “The information available regarding the effect of stress or strain rate on the fracture energy is too incomplete to be included in this Model Code.”. This confirms that there is still a gap to be filled in on this topic.

3.3.5 Young’s modulus of concrete

Recent studies are scarce on the strain rate effect on the elastic modulus of concrete. fib Bullitin 42 (Task Group 8.2, 2008), a background document on (Fédération internationale du béton (fib), 2013), presents Figure 3.8. The relation between the DIF on the Young’s modulus (DIF_E) and the crack opening velocity is found by (Dargel, 1985).

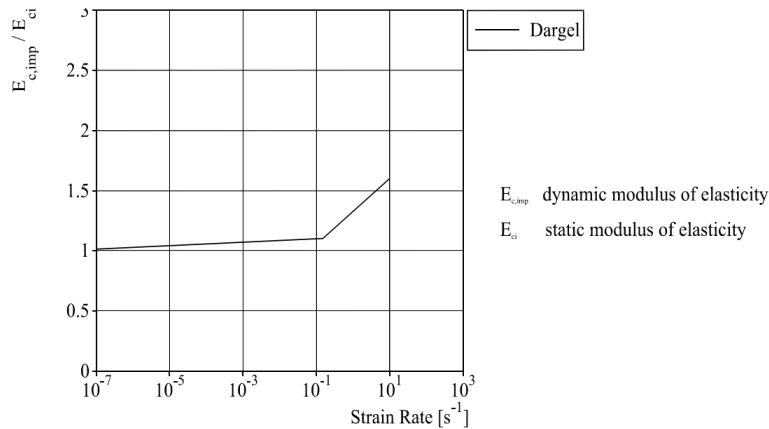


Figure 3.8: Influence of strain rate on the Young's modulus of concrete

Model Code 2010 gives (3.19) as an estimation of the DIF_E . This relationship is also mentioned in (Bischoff & Perry, 1991) and is based on Figure 3.4 (stress) and Figure 3.9 (strain).

$$DIF_E = (\dot{\epsilon}_c / \dot{\epsilon}_{c0})^{0.026} \tag{3.19}$$

$$\dot{\epsilon}_{ct0} = 1 \cdot 10^{-6} \text{ s}^{-1} \text{ for tension}$$

$$\dot{\epsilon}_{ct0} = 30 \cdot 10^{-6} \text{ s}^{-1} \text{ for compression}$$

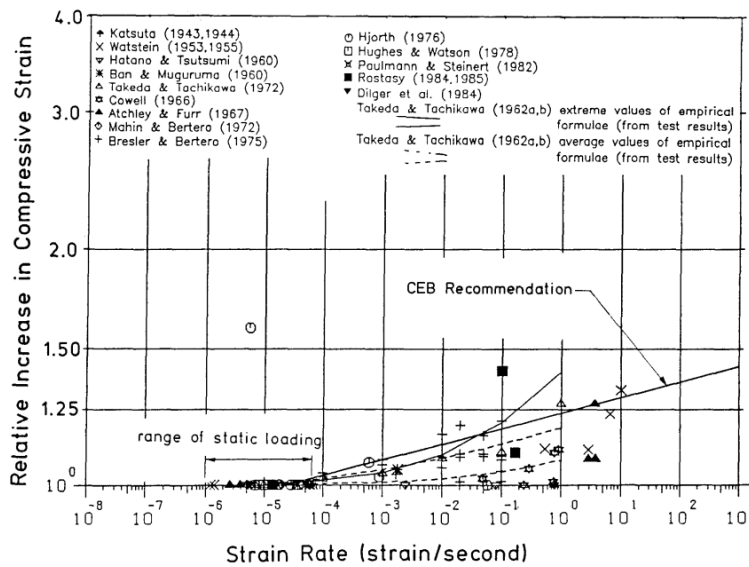


Figure 3.9: Influence of strain rate on the compressive strain

(Körmeling & Reinhardt, 1987) studied the strain rate effects on fibre reinforced concrete. The relevant results of that study are presented in Table 3.2. It appeared that the DIF_E for concrete under compression according to (3.19) has good agreement with the results of the experiments, especially for the plain concrete specimen.

Table 3.2: DIF_E for different strain rates

Strain rate [s^{-1}]	Fibre content [%]	Tensile strength [MPa]	Strain at tensile strength [%]	Elastic modulus [MPa]	DIF_E Experiment / MC2010 (compression)
$1.25 \cdot 10^{-6}$	0	3.3	0.0130	25385	Reference specimen
	1.5	3.8	0.0180	21111	Reference specimen
$2.5 \cdot 10^{-3}$	0	4.8	0.0170	28235	1.11 / 1.12
	1.5	5.4	0.0220	24545	1.16 / 1.12
1.5	0	5.5	0.0165	33333	1.31 / 1.32
	1.5	6.5	0.0225	28889	1.37 / 1.32

The DIF_E based on (3.19) for concrete under compression is considered as appropriate to use in this research. The modulus of elasticity is more relevant for concrete under compression, since concrete under tension cracks relatively quickly and therefore losing its stiffness.

3.3.6 Reinforcement steel strength

There is a large variety of steel types which makes it difficult to attach a DIF to. The DIF for reinforcement steel is not included in Model Code 2010 and UFC 3-340-02 gives merely a single design value in a table. Despite the lack of information in the design codes, the DIF on the reinforcement strength is of great importance. Most of the energy is dissipated through the yielding of the reinforcement.

A more detailed way of describing the increasing material properties due to high strain rates is by the Johnson-Cook (JC) model (Johnson & Cook, 1983). This model is only applicable on ductile metals, such as steel reinforcement bars. (3.20) provides the relation between the static behaviour (reference conditions), the influence of the strain rate and the temperature. A , B , C , n and m are material constant. These constants are experimentally determined by fitting a line between the data points of the experiment. The constants stand for the following:

- A is the yield stress of the material under reference conditions
- B is the strain hardening constant
- C is the strengthening coefficient of strain rate
- n is the strain hardening coefficient
- m is the thermal softening coefficient

ε^* is the equivalent plastic strain and is defined as $\varepsilon/\dot{\varepsilon}_0$. $\dot{\varepsilon}_0$ is the reference strain rate and is 1.0 by default, as prescribed in (Johnson & Cook, 1983). In some papers it might also relate to the static strain rate. T^* is the homogeneous temperature. Temperature effects are not included in this research.

$$\sigma_{true} = (A + B\varepsilon^n)(1 + C \ln \varepsilon^*)(1 - T^{*m}) \quad (3.20)$$

Note that the JC model gives the true stress instead of the engineering stress. The difference is that true stress considers the decrease in area of the specimen when it elongates. The engineering stress relates the applied force at any moment to the initial area of the specimen. (3.21) and (3.22) are giving the relation between the true stress, engineering stress, true strain, and engineering strain.

$$\sigma_{true} = \sigma_{eng}(\epsilon_{eng} + 1) \tag{3.21}$$

$$\epsilon_{true} = \ln(\epsilon_{eng} + 1) \tag{3.22}$$

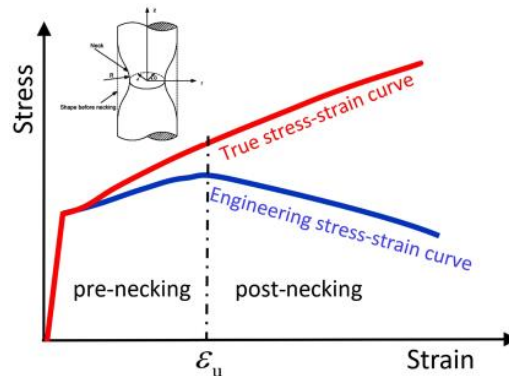


Figure 3.10: True stress-strain and engineering stress-strain

The true strain-stress curve is always increasing, while the engineering strain-stress curve has a maximum at the ultimate strain. At this point, the stress cannot increase anymore when the force is divided over the original area of the reinforcement bar (definition of the engineering stress). The point of the ultimate strain is the moment where necking occurs. Large strains then localise in a small region in the bar.

For an accurate non-linear model, it is important to specify the behaviour of the reinforcement steel in the post-necking region. This allows for analysis of the structure until failure of the reinforcement. A popular method to achieve the correct strain-stress curve in the post-necking region is by use the Bridgman (Bridgman, 1952) correction formula (3.23). The average axial stress is denoted as $\bar{\sigma}_x$.

$$\sigma_{eq} = k \bar{\sigma}_x \tag{3.23}$$

$$k = \frac{1}{\left(1 + \frac{2R}{a}\right) \ln\left(1 + \frac{a}{2R}\right)} \tag{3.24}$$

The stress state of steel is usually represented by the Von Mises stress, or sometimes called the equivalent stress. Before necking the shear components in the equivalent stress are 0. For a round bar, it then can be proven that the equivalent strain ϵ_{eq} is equal to the principal strain ϵ_1 . However, beyond the point of necking the shear component are not necessarily 0. When the shear component is non-zero, the true stress-strain curve based on ϵ_1 only is not following the right path anymore. This is depicted in Figure 3.11.

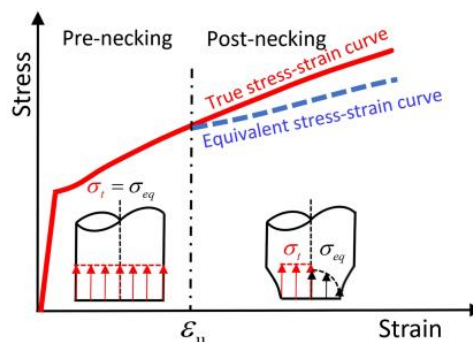


Figure 3.11: Correction of the true stress-strain curve

The correction factor k is mathematically derived and relates the radius R to radius a , as depicted in Figure 3.12. The values of R and a can be obtained by experiments or by using empirical relations. A widely used empirical relation is (3.25), found by (Le Roy et al., 1981). In this relation the corrected strain in the post-necking region is denoted as ε_{eq} and the ultimate strain as ε_u .

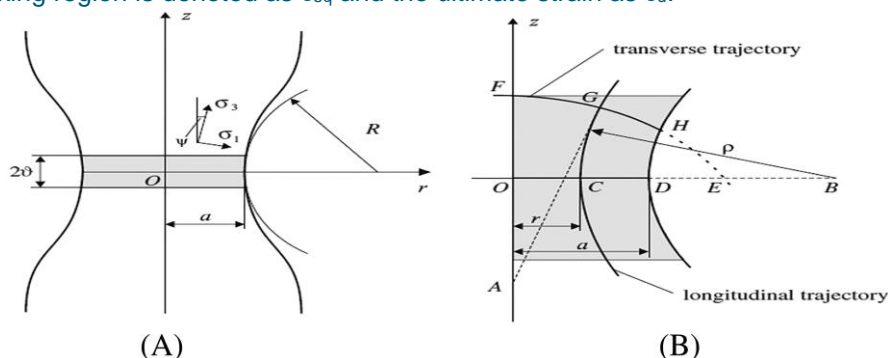


Figure 3.12: mathematical derivation of the Bridgman correction formula.

$$\frac{a}{R} = \begin{cases} 1.1(\varepsilon_{eq} - \varepsilon_u) & \text{for } \varepsilon_{eq} > \varepsilon_u \\ 0 & \text{for } \varepsilon_{eq} < \varepsilon_u \end{cases} \quad (3.25)$$

(Lin et al., 2016) did research on the dynamic strength of reinforcement steel. A comparison is made between an existing DIF formulation, the JC model and experiments. One of the conclusions of the study is that both the DIF formulations and the JC model are appropriate to use for strain rates below 75 s^{-1} . The JC model is chosen as the reinforcement model. The same parameters as in (Lin et al., 2016) are used and are included in Table 3.3. These values hold for reinforcement steel with the characteristic yield strength f_{yk} of 500 MPa. The regular design codes do not give a value for the mean yield strength f_{ym} of the reinforcement steel. The probabilistic model code (Joint Committee on Structural Safety, 2001) provides statistical parameters for reinforcement steel. The standard deviation is given as 30 MPa. Considering the fact that the characteristic value corresponds with a probability of 5%, the mean yield strength must be 550 MPa according to the normal distribution. The factor between the ultimate strength and the yield strength is 1.08, according to the design codes Model Code 2010 and NEN-EN 1992-1-1

Table 3.3: Johnson-Cook parameters for steel reinforcement

Rebar grade	$\dot{\varepsilon}_0$	A [MPa]	B [MPa]	n	C
HRB500 (Lin et al., 2016) (hot-rolled)	1.0	629.6	666.2	0.5976	0.030
B500B (Cadoni & Forni, 2015) (cold-worked)	0.001	571	643	0.720	0.02139

The difference between hot-rolled steel and cold-worked steel is the strength and ductility. Cold-worked steel is essentially hot-rolled steel with additional processing after cooling. Cold-worked steel is harder than hot-rolled steel for the same base material. This results in a higher yield stress and higher ultimate stress. Hot-rolled steel, on the other hand, is more ductile. The ultimate strain of cold-formed steel is around 5%, while for a hot-rolled bar it easily exceeds 10%.

The most common type of reinforcement in Europe is B500B. There is also B500A and B500C. The latter is mainly used in the Southern countries in Europe for earthquake resistant designing because of its ductility properties.

3.3.7 Reinforcement Young's modulus

Another conclusion of (Lin et al., 2016) is that no changes are found in the Young's modulus. Therefore, no DIF is considered for the Young's modulus of steel.

4 Cross-sectional behaviour of reinforced concrete elements

The nonlinear behaviour of a concrete beam or slab is described by the force-deflection (F-u) graph of the mid-span deflection. The F-u graph is calculated by a nonlinear finite difference model (FDM). In the finite difference method (FDM) the differential equations for beams and slabs are solved numerically. The structure is discretized, and the deflections are evaluated for each node. The stiffness is also bound to the node, this differs from finite element method (FEM), where the stiffness is bound to the element between the nodes. The bending stiffness per node is evaluated by the bending moment and corresponding curvature in the node.

4.1 Moment-curvature relationship

Constructing the moment-curvature graph for a RC cross section gives the resistance of the cross section. The moment-curvature relationship is derived by force equilibrium in the cross section. The curvature of the cross section is gradually increased under the assumption that straight cross sections remain straight. The strain is therefore proportional to the curvature. Knowing the strain in the cross section, the stress can be interpreted from the strain-stress relationship of the material. After each increase of the curvature, the neutral line is shifted in order to make force equilibrium between the compressive and tensile forces.

The forces are derived from the stress distribution in the cross section. When the concrete cracks, the tensile stress reduces, and the compressive force is greater than the tensile forces. The neutral line must shift up to make force equilibrium. Convergence is reached after the tensile force is approximately equal to the compressive forces.

The cross-section fails when the moment-curvature graph drops drastically. The area under the moment-curvature graph is the amount of strain energy the cross section can dissipate. Evaluating every cross section along the beam axis or slab area gives the total energy dissipation capacity. In other words, integrating the moment-curvature relationship over the length or area gives the energy dissipation capacity.

The procedure is summarised in the flowchart in Figure 4.1. In this figure an example is given with 2 different widths in the cross section and 3 reinforcement layers. This represents the edge nodes in the case study where the supporting beam is present.

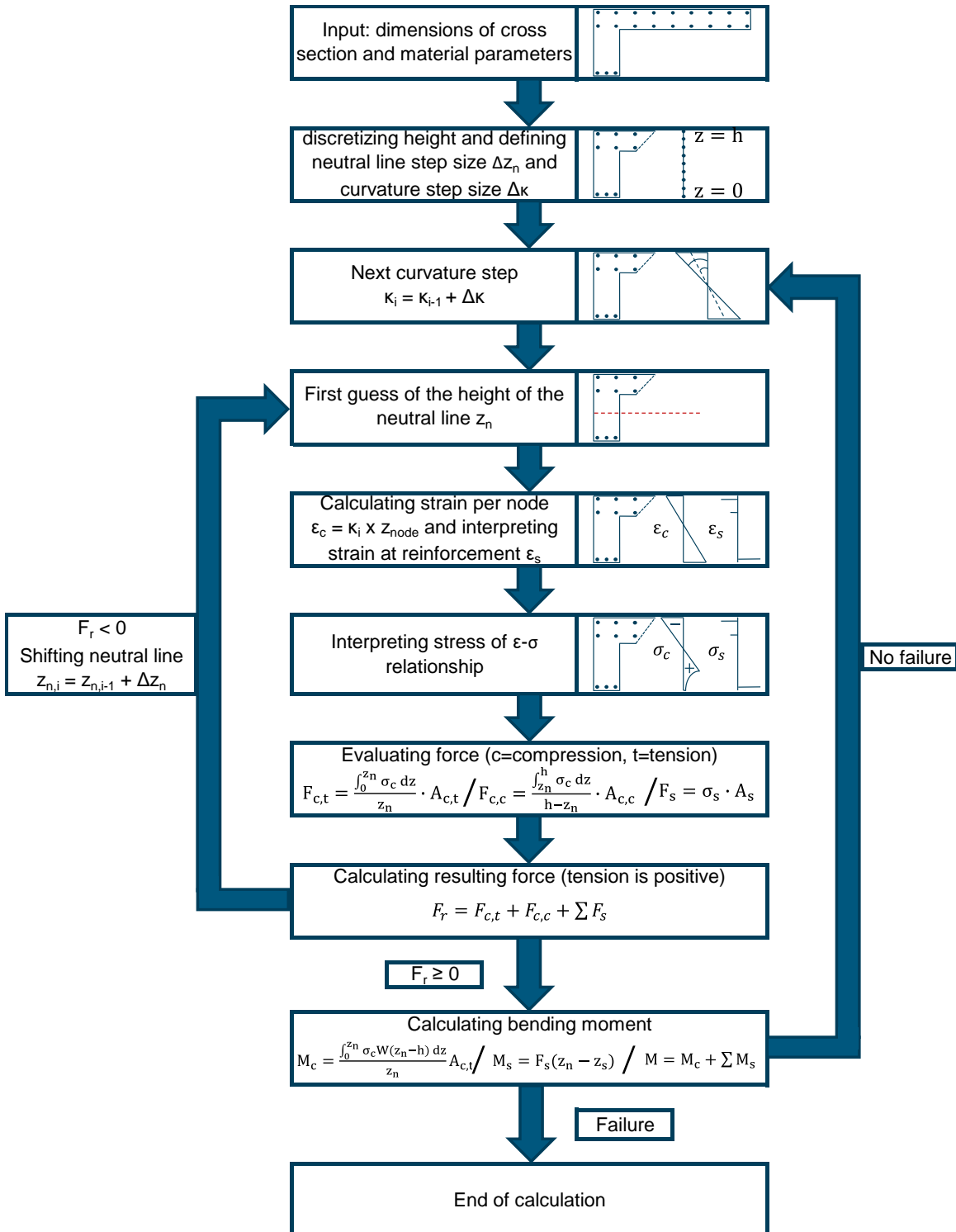


Figure 4.1: Flowchart for the moment-curvature relation

4.2 Failure criteria

In principle, the element fails when the curvature exceeds the limit according to the M- κ graph. The M- κ graph is based on an assumption which holds for a support rotation up to 2 degrees. After this support rotation, the element might behave differently than predicted. The UFC 3-340-02 expresses the failure of the element as a function of the support rotation. Depending on the support rotation, the cross-section is categorised in type I, type II, or type III:

- Type I: The cross-section works as predicted. The F-u graph represents the behaviour of the RC element accurately up to the support rotation of 2 degrees. After the support rotation of 2 degrees the concrete may be considered crushed. No shear reinforcement is required and only the reinforcement at the tension side is considered.
- Type II: The concrete is considered crushed, but the concrete cover remains intact. Compression reinforcement is required to take over the compressive force of the crushed concrete. The compression reinforcement should be sufficiently laterally restrained in order to work properly. When this is the case, a support rotation up to 6 degrees is possible. Without the lateral restraint, the compression reinforcement may buckle prematurely and cause failure of the element. When no stirrups are applied, the direct shear capacity should be checked.
- Type III: The concrete cover is completely disengaged. The bending moment resisting relies on the tension and compression reinforcement. A support rotation up to 12 degrees is possible.

5 Static behaviour of reinforced concrete elements

In this chapter, the static behaviour of concrete is described. By use of the finite difference model (FDM) for a one-way element and two-way element, the force-deflection (F-u) graph is obtained. The F-u graph represents the nonlinearity in a mass-spring system, which is addressed in chapter 6.

5.1 Finite difference method

There are several assumptions made in the FDM model:

- The Euler-Bernoulli theory is applied on beams and the Kirchhoff theory on slabs
- The structure is symmetric and in case of a slab double symmetric
- A discrete crack is assumed through the middle of the beam and slab
- The beam is rigidly supported on the outer nodes, the slab is rigidly supported on the corners
- The structure is loaded by an equally distributed load

In the FDM the solution is approximated by a differentiation scheme. The most basic approaches are the forward difference scheme, the backward difference scheme, and the central difference scheme and formulated in (5.1), (5.2) and (5.3) respectively.

$$\frac{d}{dx} w(x) \approx \frac{w_{i+1} - w_i}{\Delta x} \quad (5.1)$$

$$\frac{d}{dx} w(x) \approx \frac{w_i - w_{i-1}}{\Delta x} \quad (5.2)$$

$$\frac{d}{dx} w(x) \approx \frac{w_{i+1} - w_{i-1}}{2\Delta x} \quad (5.3)$$

It is possible to include more nodes for a better approximation. By approximating the differential equation an error remains between the approximation and the exact solution. This error is called the truncation error. A good approximating scheme will result in a smaller error. However, in this research the central difference scheme is used as indicated in (5.4) - (5.11).

$$\frac{d^2}{dx^2} w(x) \approx \frac{w_{i+1} - 2w_i + w_{i-1}}{(\Delta x)^2} \quad (5.4)$$

$$\frac{d^3}{dx^3} w(x) \approx \frac{w_{i+2} - 2w_{i+1} + 2w_{i-1} - w_{i-2}}{2(\Delta x)^3} \quad (5.5)$$

$$\frac{d^4}{dx^4} w(x) \approx \frac{w_{i+2} - 4w_{i+1} + 6w_i - 4w_{i-1} + w_{i-2}}{(\Delta x)^4} \quad (5.6)$$

The central difference scheme is applied similarly for the deflection function in 2 directions.

$$\frac{\partial}{\partial x} w(x, y) \approx \frac{w_{i+1, j} - w_{i-1, j}}{2\Delta x} \quad (5.7)$$

$$\frac{\partial^2}{\partial x \partial y} w(x, y) \approx \frac{\frac{w_{i+1, j+1} - w_{i-1, j+1}}{2\Delta x} - \frac{w_{i+1, j-1} - w_{i-1, j-1}}{2\Delta x}}{2\Delta y} \quad (5.8)$$

$$\frac{\partial^3}{\partial x^2 \partial y} w(x, y) \approx \frac{\frac{w_{i+1,j+1} - 2w_{i,j+1} + w_{i-1,j+1}}{(\Delta x)^2} - \frac{w_{i+1,j-1} - 2w_{i,j-1} + w_{i-1,j-1}}{(\Delta x)^2}}{2\Delta y} \quad (5.9)$$

$$\frac{\partial^4}{\partial x^2 \partial y^2} w(x, y) \approx \frac{\frac{w_{i+1,j+1} - 2w_{i,j+1} + w_{i-1,j+1}}{(\Delta x)^2} - 2\frac{w_{i+1,j} - 2w_{i,j} + w_{i-1,j}}{(\Delta x)^2} + \frac{w_{i+1,j-1} - 2w_{i,j-1} + w_{i-1,j-1}}{(\Delta x)^2}}{(\Delta y)^2} \quad (5.10)$$

$$\frac{\partial^4}{\partial x^4} w(x) \approx \frac{w_{i+2,j} - 4w_{i+1,j} + 6w_{i,j} - 4w_{i-1,j} + w_{i-2,j}}{(\Delta x)^4} \quad (5.11)$$

5.2 One-way elements

5.2.1 Finite difference model

The Euler-Bernoulli equation that describes the deflection of a beam is formulated in (5.12). This equation is discretized according to the central difference scheme. The deformation of the node of is denoted as w_i and is isolated on the left-hand side of (5.14).

$$EI \frac{d^4}{dx^4} w(x) = -q \quad (5.12)$$

$$EI \frac{w_{i+2} - 4w_{i+1} + 6w_i - 4w_{i-1} + w_{i-2}}{(\Delta x)^4} = -q \quad (5.13)$$

$$w_i = \frac{1}{6} \left(-\frac{q (\Delta x)^4}{EI} - w_{i+2} + 4w_{i+1} + 4w_{i-1} - w_{i-2} \right) \quad (5.14)$$

For the deflection of the first 2 nodes and last 2 nodes, so-called 'ghost' nodes need to be specified. The ghost nodes are located beyond the physical boundary conditions and their properties depend on the boundary conditions. This is illustrated by an example. Figure 5.1 displays one half of a symmetric beam. On the left side the support is hinged, clamped or something in between. On the right side the symmetry conditions are applied.

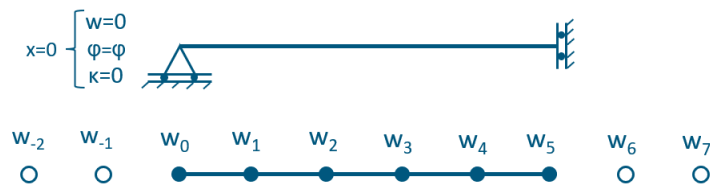


Figure 5.1: FDM beam example

The beam is loaded by a distributed load. For this case it is known that the shear force is 0 in the middle of the beam. It is also known that the rotation is 0 in the elastic stage.

$$w(x = 0) = w_0 \rightarrow w_i = w_0 \quad (5.15)$$

$$\frac{d}{dx} w(x)|_{x=0} = 0 \rightarrow w_{-1} = w_1 \quad (5.16)$$

$$\frac{d^2}{dx^2} w(x)|_{x=0} = 0 \rightarrow w_{-1} = 2w_0 - w_1 \quad (5.17)$$

When the reinforcement bars start to yield, a plastic hinge forms in the middle of the beam, causing a rotation at this location. The amount of rotation lies somewhere between the uncracked cross section (boundary condition (5.18)) and a complete plastic hinge (boundary condition (5.19)) and is defined by the factor ζ according to (5.21).

$$\frac{d}{dx}w(x)|_{x=L/2} = 0 \rightarrow w_6 = w_4 \quad (5.18)$$

$$\frac{d^2}{dx^2}w(x)|_{x=L/2} = 0 \rightarrow w_6 = 2w_5 - w_4 \quad (5.19)$$

$$w_6 = 2w_5 - w_4 + \zeta * (w_4 - w_5) \quad (5.20)$$

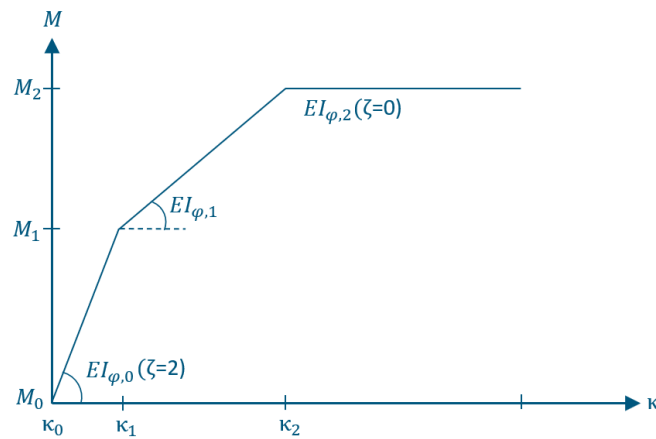


Figure 5.2: illustration of rotational stiffness at the discrete crack

$$\zeta = 2 * \frac{EI_{\varphi,i}}{EI_{\varphi,0}} \quad (5.21)$$

$$EI_{\varphi,i} = \frac{M_{i+1} - M_i}{\kappa_{i+1} - \kappa_i} \quad (5.22)$$

$$EI_{\varphi,0} = \frac{M_1 - M_0}{\kappa_1 - \kappa_0} = \frac{M_1}{\kappa_1} \quad (5.23)$$

The symmetry condition (5.20) represents a discrete crack in the middle of the beam. The reinforcement only yields at the location of the discrete crack in the model. Other smaller cracks in the beam are represented by a reduction of the secant bending stiffness, where the limit is set on the bending stiffness that belongs to the moment where the reinforcement start to yield, as shown in Figure 5.3.

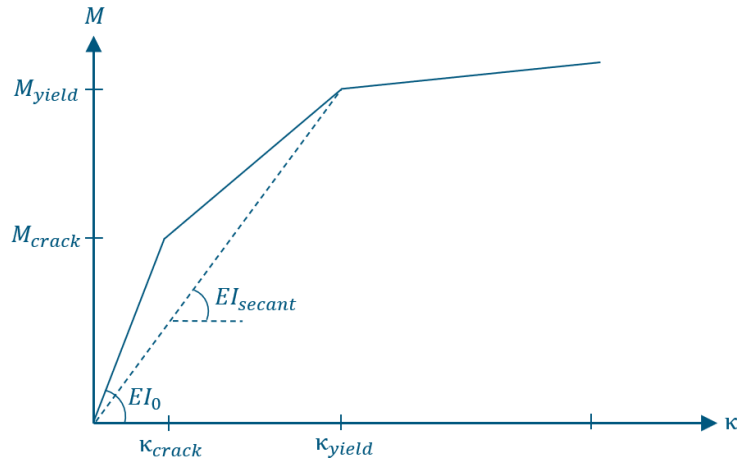


Figure 5.3: Secant bending stiffness

After each load step, the bending moment is derived based on the converged deflection. The corresponding curvature is read off in the moment-curvature graph. The bending stiffness of the node in the next iteration is based on the bending moment and curvature of the previous load step. Figure 5.4 illustrates this. After the first load step the node is still in the elastic stage. Therefore, the bending stiffness in the next load step is equal to the initial stiffness. After the second load step the bending moment is found in the elasto-plastic stage. This leads to a reduction of the bending stiffness in the next load step.

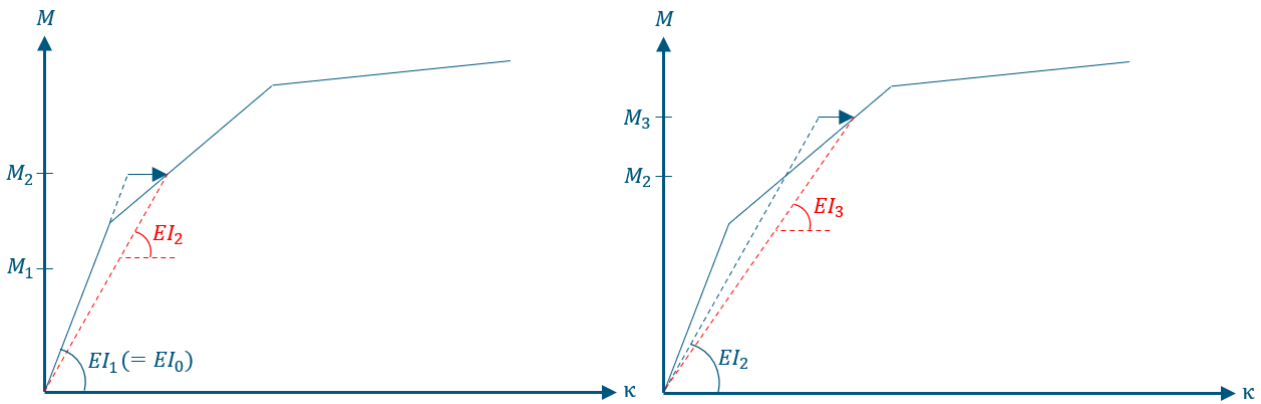


Figure 5.4: Change in Secant stiffness after an iteration

After each load step a set of nodal deflection is found. This is used arrive at the mass factor and load factor to approach the beam as a lumped mass spring system.

$$K_M = \frac{\sum_{nodes} M_i \phi_i^2}{\sum_{nodes} M_i} \tag{5.24}$$

$$K_L = \frac{\sum_{nodes} M_i \phi_i}{\sum_{nodes} M_i} \tag{5.25}$$

5.2.2 Force-deflection relationship

A output of the FDM model is the force-deflection (F-u) relationship at mid-span. This is extensively described further on in the research. Roughly, the F-u relationship has three branches: the elastic branch, the cracked branch, and the yielding branch. These are indicated in Figure 5.5.

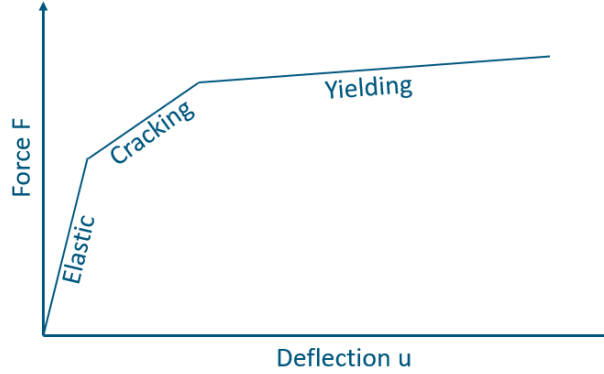


Figure 5.5: Roughly graphed F-u relationship

5.3 Two-way elements

(Blaauwendraad, 2010) is used for the derivation of the two-way element FDM model.

5.3.1 Finite difference model

The FDM for a slab is more complicated than the FDM applied on a beam. The load in a slab is carried by the bending moment m_{xx} , m_{yy} and m_{xy} , as formulated in (5.26).

$$\frac{\partial^2}{\partial x^2} m_{xx} + 2 \frac{\partial^2}{\partial x \partial y} m_{xy} + \frac{\partial^2}{\partial y^2} m_{yy} = -p \quad (5.26)$$

Furthermore, there is interaction between the curvatures κ_{xx} and κ_{yy} . This interaction is defined by rigidity D_v . The formulation of D_v is based on (Blaauwendraad, 2010), which gives (5.28) as practical value, since it is not clear what rigidity must be used. This leads to the correct term for the isotropic case. For the same reason, (Blaauwendraad, 2010) gives an expression for rigidity D_{xy} , which connects the torsional moment m_{xy} and torsional deformation ρ_{xy} , and is formulated as (5.29).

$$\begin{bmatrix} m_{xx} \\ m_{yy} \\ m_{xy} \end{bmatrix} = \begin{bmatrix} D_{xx} & D_v & 0 \\ D_v & D_{yy} & 0 \\ 0 & 0 & D_{xy} \end{bmatrix} \begin{bmatrix} \kappa_{xx} \\ \kappa_{yy} \\ \rho_{xy} \end{bmatrix} \quad (5.27)$$

$$D_v = \nu \sqrt{D_{xx} D_{yy}} \quad (5.28)$$

$$D_{xy} = \frac{1}{2} (1 - \nu) \sqrt{D_{xx} D_{yy}} \quad (5.29)$$

Formulating the curvatures and torsional deformation as (5.30), (5.31) and (5.32) the equilibrium equation (5.33) is derived. Simplifying the equilibrium equation (5.34) is obtained. As mentioned before, this equilibrium equation is valid for an isotropic slab. When this equation is applied on an anisotropic slab the results might differ from the analytical solution.

$$\kappa_{xx} = \frac{\partial^2}{\partial x^2} w(x, y) \quad (5.30)$$

$$\kappa_{yy} = \frac{\partial^2}{\partial y^2} w(x, y) \tag{5.31}$$

$$\rho_{xy} = 2 \frac{\partial^2}{\partial x \partial y} w(x, y) \tag{5.32}$$

$$\frac{\partial^2}{\partial x^2} \left(D_{xx} \frac{\partial^2}{\partial x^2} w(x, y) + D_v \frac{\partial^2}{\partial y^2} w(x, y) \right) + 2 \frac{\partial^2}{\partial x \partial y} \left(2D_{xy} \frac{\partial^2}{\partial x \partial y} w(x, y) \right) + \frac{\partial^2}{\partial y^2} \left(D_{yy} \frac{\partial^2}{\partial y^2} w(x, y) + D_v \frac{\partial^2}{\partial x^2} w(x, y) \right) = -p \tag{5.33}$$

$$D_{xx} \frac{\partial^4}{\partial x^4} w(x, y) + 2 \sqrt{D_{xx} D_{yy}} \frac{\partial^4}{\partial x^2 \partial y^2} w(x, y) + D_{yy} \frac{\partial^4}{\partial y^4} w(x, y) = -p \tag{5.34}$$

The boundary conditions for a double symmetric slab are similar to that of a beam. However, the discrete crack over the symmetry lines is treated differently. Considering the example in Figure 5.6, if one node on the symmetry axis is past the cracking bending moment while the other nodes are still in the uncracked region, the stiffness of the whole cross section lends itself to the stiffest node. In other words, if ζ is evaluated at each node, the largest value of ζ is governing for the whole symmetry line.

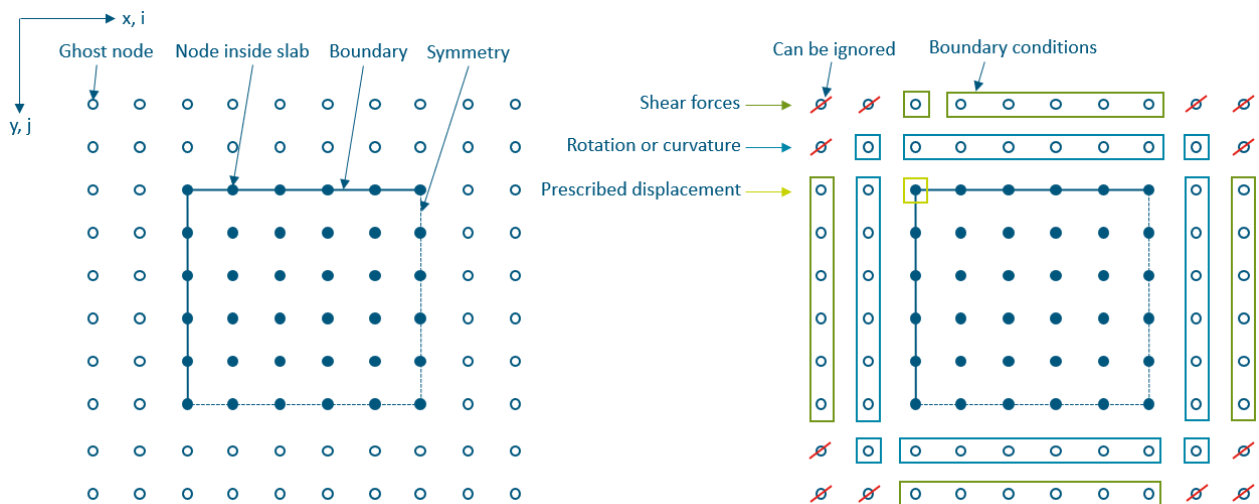


Figure 5.6: FDM for a 2D case

The general equation of force equilibrium at the edges is defined as (5.35), where f is a support reaction (illustrated in Figure 5.7).

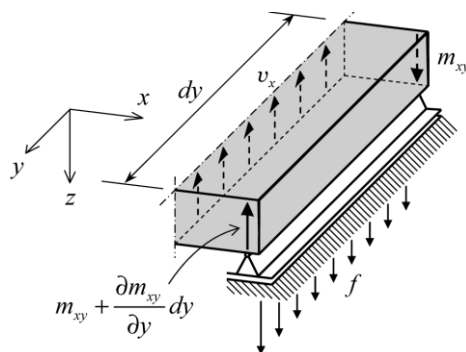


Figure 5.7: general boundary condition

$$\frac{\partial}{\partial x} m_{xx} + \frac{\partial}{\partial y} m_{xy} = f \quad (5.35)$$

Simply supported edge condition

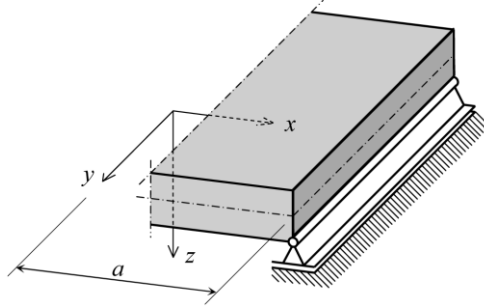


Figure 5.8: Simply supported edge condition

$$\begin{cases} w(x, y) = 0 \\ m_{xx} = 0 \end{cases} \rightarrow \begin{cases} w_{i,j} = 0 \\ w_{i-1,j} = 2w_{i,j} - w_{i+1,j} - v \frac{(\Delta x)^2}{(\Delta y)^2} (w_{i,j+1} - 2w_{i,j} + w_{i,j-1}) \end{cases} \quad (5.36)$$

Clamped edge condition

Initially, a clamped boundary condition has no translation and no rotation and the constrained nodes. When cracking occurs, the nodes start to allow some rotation around the y-axis in Figure 5.9.

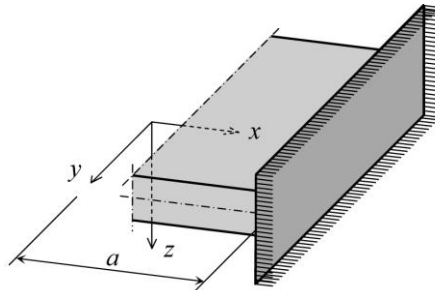


Figure 5.9: Clamped edge condition

$$\begin{cases} w(x, y) = 0 \\ \frac{\partial}{\partial x} w(x, y) = 0 \end{cases} \rightarrow \begin{cases} w_{i,j} = 0 \\ w_{i-1,j} = w_{i+1,j} \end{cases} \quad (5.37)$$

$$\begin{cases} w(x, y) = 0 \\ crack \end{cases} \rightarrow \begin{cases} w_{i,j} = 0 \\ w_{i-1,j} = 2w_{i,j} - w_{i+1,j} - v \frac{(\Delta x)^2}{(\Delta y)^2} (w_{i,j+1} - 2w_{i,j} + w_{i,j-1}) + \zeta \left(w_{i+1,j} - w_{i,j} + v \frac{(\Delta x)^2}{(\Delta y)^2} (w_{i,j+1} - 2w_{i,j} + w_{i,j-1}) \right) \end{cases} \quad (5.38)$$

Free edge condition

On a free edge the force equilibrium is formulated as (5.39), since there is no support reaction.

$$\left\{ \begin{array}{l} m_{xx} = 0 \\ \frac{\partial}{\partial x} m_{xx} + \frac{\partial}{\partial y} m_{xy} = 0 \end{array} \right. \rightarrow \left\{ \begin{array}{l} \frac{w_{i+1,j} - 2w_{i,j} + w_{i-1,j}}{(\Delta x)^2} + \nu \frac{w_{i,j+1} - 2w_{i,j} + w_{i,j-1}}{(\Delta y)^2} = 0 \\ \frac{w_{i+2,j} - 2w_{i+1,j} + 2w_{i-1,j} - w_{i-2,j}}{2(\Delta x)^3} + \frac{\frac{w_{i+1,j+1} - 2w_{i+1,j} + w_{i+1,j-1}}{(\Delta y)^2} - \frac{w_{i-1,j+1} - 2w_{i-1,j} + w_{i-1,j-1}}{(\Delta y)^2}}{2\Delta x} = 0 \end{array} \right. \quad (5.39)$$

Symmetry conditions (discrete crack)

In a double symmetric slab supported in the corners it is known that the torsional bending moment m_{xy} is 0 at every position. Also, there is no support reaction present. This means that the symmetry condition for a discrete crack is defined as (5.40).

$$\left\{ \begin{array}{l} w(x, y) = 0 \\ crack \end{array} \right. \rightarrow \left\{ \begin{array}{l} w_{i,j} = 0 \\ w_{i-1,j} = 2w_{i,j} - w_{i+1,j} - \nu \frac{(\Delta x)^2}{(\Delta y)^2} (w_{i,j+1} - 2w_{i,j} + w_{i,j-1}) + \zeta \left(w_{i+1,j} - w_{i,j} + \nu \frac{(\Delta x)^2}{(\Delta y)^2} (w_{i,j+1} - 2w_{i,j} + w_{i,j-1}) \right) \end{array} \right. \quad (5.40)$$

Poisson's ratio

The Poisson's ratio for cracked concrete is not easy to determine. However, a good approximation can be made by looking at the physical behaviour of concrete. Before any crack arises, it is widely accepted to take the Poisson's ratio as 0.2, shown in the element on the left in Figure 5.10. The lower limit of the Poisson's ratio in reinforced concrete is 0. It is assumed that the lower limit is reached at the onset of yielding of the reinforcement. In the cracked stage an interpolation is made according to (5.41).

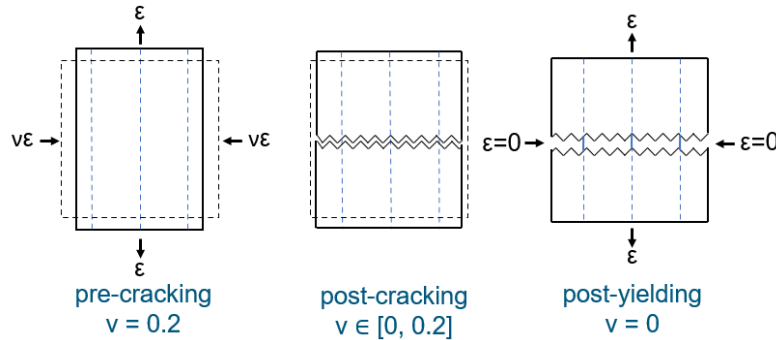


Figure 5.10: Poisson's ratio after cracking

$$\nu = \begin{cases} 0.2 & \text{if } |\kappa| \leq \kappa_{crack} \\ 0.2 \frac{|\kappa| - \kappa_{crack}}{\kappa_{yield} - \kappa_{crack}} & \text{if } \kappa_{crack} \leq |\kappa| \leq \kappa_{yield} \\ 0 & \text{if } |\kappa| \geq \kappa_{yield} \end{cases} \quad (5.41)$$

5.3.2 Force-deflection relationship

The F-u graph for a two-way element is similar to that of the one-way element. It can also be identified by the three branches as mentioned in chapter 5.2.2.

6 Dynamic behaviour of reinforced concrete elements

In this chapter, the structural response to a blast load is described by means of a mass-spring system. The mass-spring system is then applied on a one-way element and a two-way element. They represent the single degree of freedom (SDOF) approach and the two degrees of freedom (2DOF) approach, respectively.

6.1 Structural response to a blast load

6.1.1 Mass-spring-damper system

The use of the mass-spring(-damper) system in this research is illustrated by the deflection of a simply supported beam. The mass in the mass-spring-damper system represents the mass of the beam, the spring represents the stiffness of the beam, and the damper represents the structural damping. The mass is connected to the spring and damper and the other end of the spring and damper is attached to a rigid surface. When an impact load hits the beam, it starts oscillating. It is assumed that only the first eigenmode has contribution to the vibration of the beam. That way, the mass-spring-damper in Figure 6.1 should behave the same when the correct parameters are chosen. The general equation of motion of a mass-spring-damper system is formulated in (6.1). In this equation, the M stands for the dynamic mass, the C for the structural damping, and k for the structural damping

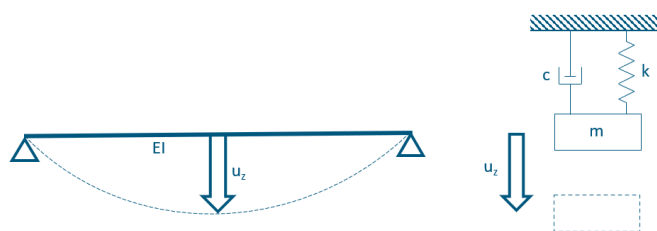


Figure 6.1: Mass-spring-damper system for a beam

$$M\ddot{u}_z + C\dot{u}_z + ku_z = F(t) \quad (6.1)$$

6.1.2 Inertia effects

The difference between a static analysis and a dynamic analysis is the inclusion of damping and inertia. Typically, the influence of damping is small while the inertia effects is significantly larger and can dominate in the structural response. This is especially true when the duration of the load is much shorter than the structural response time.

6.1.3 Structural damping

In blast analysis it is accepted to disregard damping for the following reasons, according to UFC 3-340-02:

- Damping has very little effect on the first peak of response, which is usually the only cycle of response that is of interest.
- The energy dissipated through plastic deformation is much greater than that dissipated by normal structural damping.
- Ignoring damping is a conservative approach.

If damping has to be considered in an analysis the UFC recommends to express it as some percentage of the critical damping. For free vibration, this is the amount of damping that would remove all vibration from the system and allow it to return to its neutral position. The critical damping is expressed as (6.2).

$$C_{cr} = 2 \sqrt{kM} \quad (6.2)$$

UFC 3-340-02 states: "For steel structures, c should be taken as $0.05 C_{cr}$ and $0.01 C_{cr}$ for reinforced concrete structures."

6.2 One-way elements as a single degree of freedom mass-spring system

6.2.1 Equation of motion and equivalent parameters

Not all the mass of the one-way element contributes to the SDOF representation of the one-way slab. The mass in the middle contributed much more than the mass close to the supports. The same principle holds for the distributed load on the one-way slab. The percentage of the mass and the load that is activated are called the mass factor K_M and the load factor K_L , respectively. The equation of motion without damping is thereby defined as (6.3).

$$K_M M \ddot{u}_z + K_L k u_z = K_L F(t) \quad (6.3)$$

The mass factor and load factor are calculated with the normalised deflection function ϕ . They are defined as (6.4) and (6.5).

$$K_M = \frac{\int_0^L m \phi(x)^2 dx}{mL} \quad (6.4)$$

$$K_L = \frac{\int_0^L p \phi(x) dx}{pL} \quad (6.5)$$

The equation of motion can also be written as (6.6). Here the load-mass factor is denoted as K_{LM} and is formulated as (6.7).

$$K_{LM} M \ddot{u}_z + k u_z = F(t) \quad (6.6)$$

$$K_{LM} = \frac{K_M}{K_L} \quad (6.7)$$

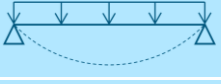
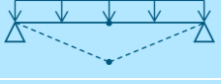



The mass factor and load factor can be approximated by a theoretical deflection function $\Phi(x)$. (Biggs, 1964) uses the deflection functions in Table 6.1. This table is partially adopted from (Biggs, 1964). The load factor K_L is included in the dynamic spring constant. For each load diagram the dynamic spring constant is given for the deflection function.

For the simply supported beam a comparison is made between the deflection function according to (Biggs, 1964) and (6.15). Both dynamic spring constants result in a similar, but not exactly equal, value. For example, at the first loading diagram the factors on the spring constant are $384/5 \cdot 0.64 = 49.15$ and $\pi^4/2 = 48.70$. This difference is barely noticeable in the results of the mass-spring system.

The mass factor, load factor and load-mass factor in Table 6.1 indicate the upper and lower limits for the corresponding loading diagrams. For a clamped beam the mass factor starts at 0.41. It gradually climbs up to 0.50 as the plastic hinge forms. However, the mass factor can only reach 0.50 if the plastic hinge has fully developed at the supports while the middle part is still fully elastic. This is unlikely to happen in a

concrete beam since cracking in the middle of the beam occurs not to long after the cracks at the supports when the load is applied in equal load steps.

Table 6.1: participating mass and load factor for different loading diagrams.

Loading diagram	Strain range	$\Phi(x)$	K_M	K_L	K_{LM}	Dynamic spring constant
	Elastic	$\frac{16}{5L^4}(L^3x - 2Lx^3 + x^4)$ or (5.1)	0.50	0.64	0.78	$\frac{384}{5}K_L \frac{EI}{L^4}$ or $\frac{\pi^4 EI}{2 L^4}$
	Plastic	$\frac{2x}{L}$ for $x < \frac{L}{2}$	0.33	0.50	0.66	0
	Elastic	$\frac{16}{L^4}(L^2x^2 - 2Lx^3 + x^4)$	0.41	0.53	0.77	$384K_L \frac{EI}{L^4}$
	Elastic-plastic	$\frac{16}{5L^4}(L^3x - 2Lx^3 + x^4)$	0.50	0.64	0.78	$\frac{384}{5}K_L \frac{EI}{L^4}$
	Plastic	$\frac{2x}{L}$ for $x < \frac{L}{2}$	0.33	0.50	0.66	0

6.2.2 Analytical solution

There are several methods to arrive at the deflection of a SDOF system. One method is to analytically solve the second order differential equation. This might be the way to go when the force-deflection relationship is simple. Figure 6.2 shows the approach of the response of a single-mass-spring system to a pulse loading. The shown force-deflection is typical for a simply supported steel beam. Appendix IV illustrates how such a SDOF mass-spring system can be solved.

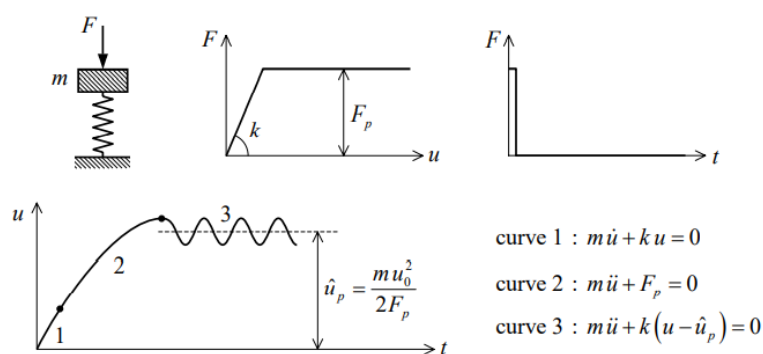


Figure 6.2: Analytical approach for a SDOF mass-spring system

The force-deflection relationship of reinforced concrete is more complicated than the one shown in Figure 6.2. In that case much more curves need to be added to analytically describe the deflection in time. This would unnecessarily complicate the solution. Approach it numerically is in that case more convenient and is therefore used in further research.

6.2.3 Numerical solution

Another method of arriving at the deflection of a SDOF system is by solving the equation of motion using direct numerical time integration of the equilibrium equation. With this method, it is easier to include a more complex nonlinear behaviour. Direct time integration can be subdivided into explicit integration methods and implicit integration methods. The main advantage of the implicit methods over the explicit methods is that implicit methods can be unconditionally stable, whereas explicit methods need a small enough time step to be stable. The unconditional stability depends on the type of implicit method that has been chosen. The Newmark method is such a type of implicit method. It should be noted that the Newmark method does not guarantee the unconditional stability in nonlinear analysis. This is especially true for long term simulation, as stated in (Saieni, 2012). The main point of interest in this research is the first peak in the time-deflection graph. Therefore, the risk of instability of the solution is small and does not weigh against the advantages of the Newmark method.

The acceleration is predicted by an iterative procedure. In this research the Newton-Raphson method is chosen as the iterative procedure. In general, the Newton-Raphson method leads to the converged solution in relatively few iterations. After each iteration, the tangent stiffness matrix \mathbf{K}_t is updated and thereby getting closer to the solution after each iteration. This is illustrated in Figure 6.3.

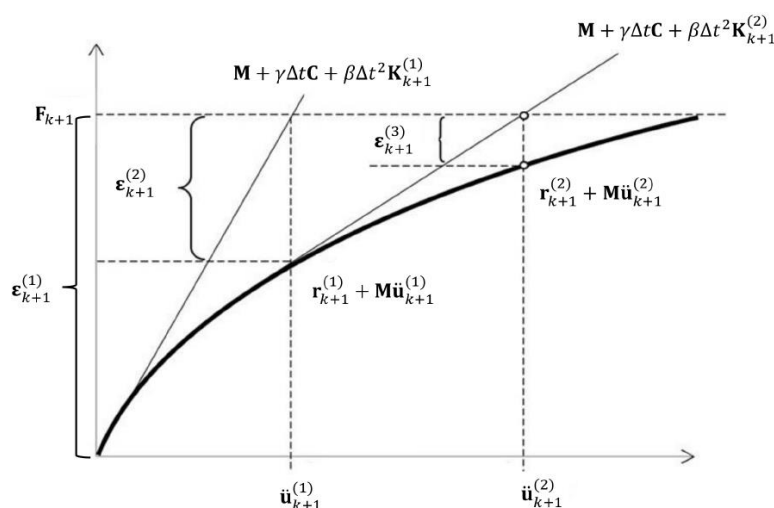


Figure 6.3: Newton-Raphson iteration

The procedure of the Newmark and Newton-Raphson procedure is summarised in Figure 6.4. This is the general approach for multiple degrees of freedom. The matrices should be considered as scalars. An appropriate time step size should be chosen from which the acceleration, velocity and deflection is calculated in the next timestep. The velocity is calculated with (6.8) and the deflection with (6.9). The acceleration is calculated using the Newton-Raphson iteration method. The acceleration at $t=0$ is determined by (6.14), where v_0 and u_0 are respectively the initial velocity and deflection. This is the first prediction of the acceleration in the next time step. This first prediction is refined by adding (6.12), where the residual force is divided by the tangent stiffness. The newly discovered acceleration is plugged in to (6.10) again, which leads to the better approximation of the acceleration. This process is repeated until (6.12) approaches 0. The γ and β values are 0.5 and 0.25 respectively. For completeness the contribution of damping is included in the equations.

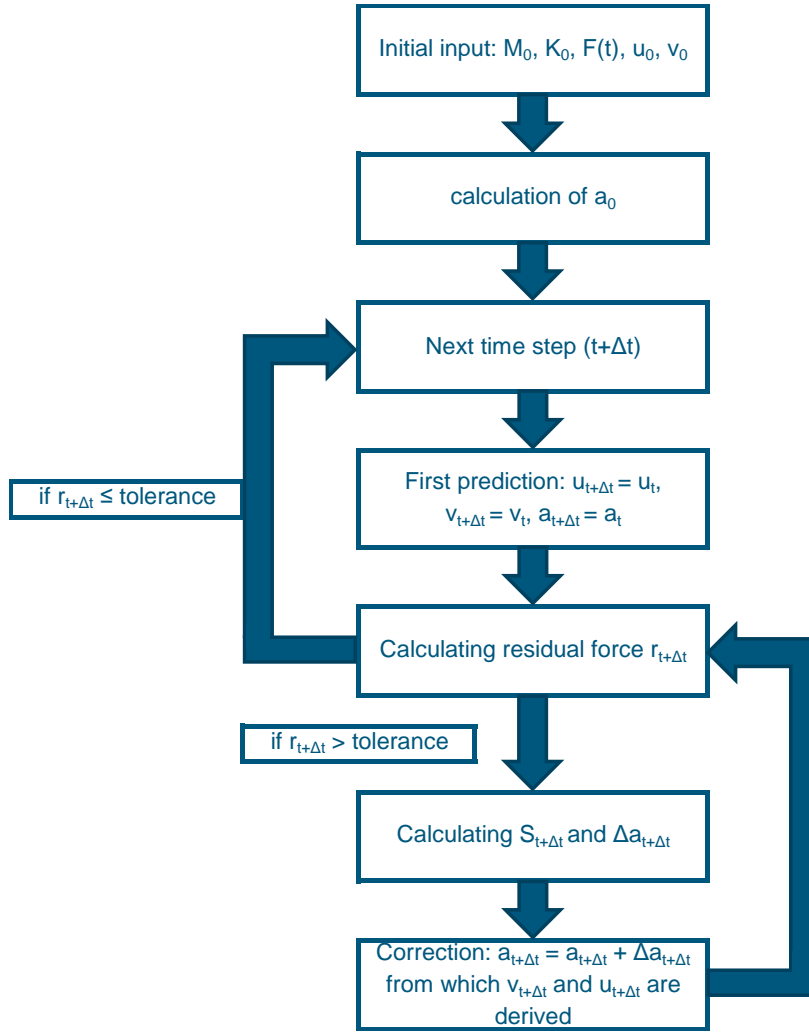


Figure 6.4: Flowchart SDOF time-marching Newton-Raphson scheme

$$v_{t+\Delta t} = v_t + \Delta t((1 - \gamma)a_t + \gamma a_{t+\Delta t}) \quad (6.8)$$

$$u_{t+\Delta t} = u_t + \Delta t v_t + \frac{1}{2}(\Delta t)^2((1 - 2\beta)a_t + 2\beta a_{t+\Delta t}) \quad (6.9)$$

$$r_{t+\Delta t} = K_M M a_{t+\Delta t} + C v_{t+\Delta t} + K_L F_{S,t+\Delta t} - K_L F_{t+\Delta t} \quad (6.10)$$

$$S_{t+\Delta t} = K_M M + \gamma \Delta t C + \beta (\Delta t)^2 \left(K_L \frac{F_{S,t+\Delta t} - F_{S,t}}{u_{t+\Delta t} - u_t} \right) \quad (6.11)$$

$$\Delta a_{t+\Delta t} = -\frac{r_{t+\Delta t}}{S_{t+\Delta t}} \quad (6.12)$$

$$a_{t+\Delta t,n} = a_{t+\Delta t} + \Delta a_{t+\Delta t} \quad (6.13)$$

$$a_0 = \frac{K_L F_0 - C v_0 - K_L K_0 u_0}{K_M M} \quad (6.14)$$

The spring force (F_s) is a characteristic of the one-way slab, which can be determined by a static analysis. The DIFs should be taken into account for the correct force-deflection graph that represents the one-way slab behaviour under blast load. In the design the strain rate is yet unknown. Thus, a verification of the assumed strain rate beforehand is needed after the blast analysis is performed.

6.3 Two-way elements as a two degrees of freedom mass-spring system

6.3.1 Equations of motion and equivalent parameters

In the two-degree of freedom representation the deflection of the beam is taken as the additional degree of freedom. It is not directly clear how the equations of motion should look like. There is coupling between the beams and the slab that makes it more complicated than 2 separate systems. The derivation of the correct equations of motion are demonstrated by an example. The example is based on section 4.6 of (Biggs, 1964), where a beam is supported by 2 girders as shown in Figure 6.5.

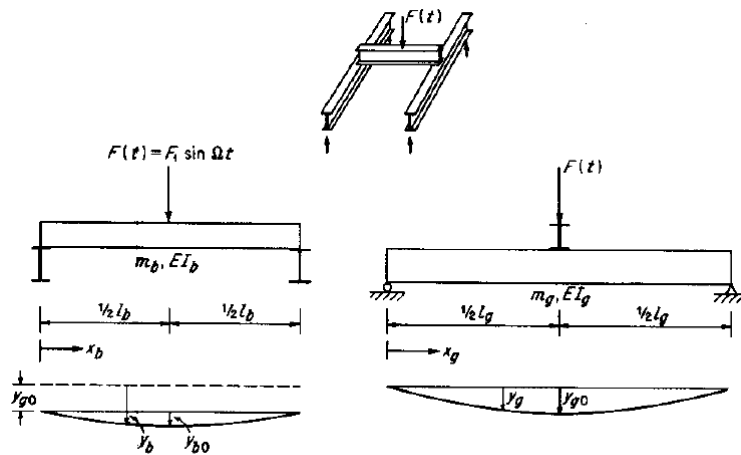


FIGURE 4.14 Beam-girder system—notation.

$$y_g = y_{g0} \sin \frac{\pi x_g}{l_g}$$

$$y_b = y_{g0} + y_{b0} \sin \frac{\pi x_b}{l_b}$$

Figure 6.5: Used example

The static deflection function of the girder is sine shaped. The deflection function of the beam is also sine shaped with the addition of the midspan deflection of the girders. The same principle is applied on the case study, only here the deflection function of the slab goes in 2 directions.

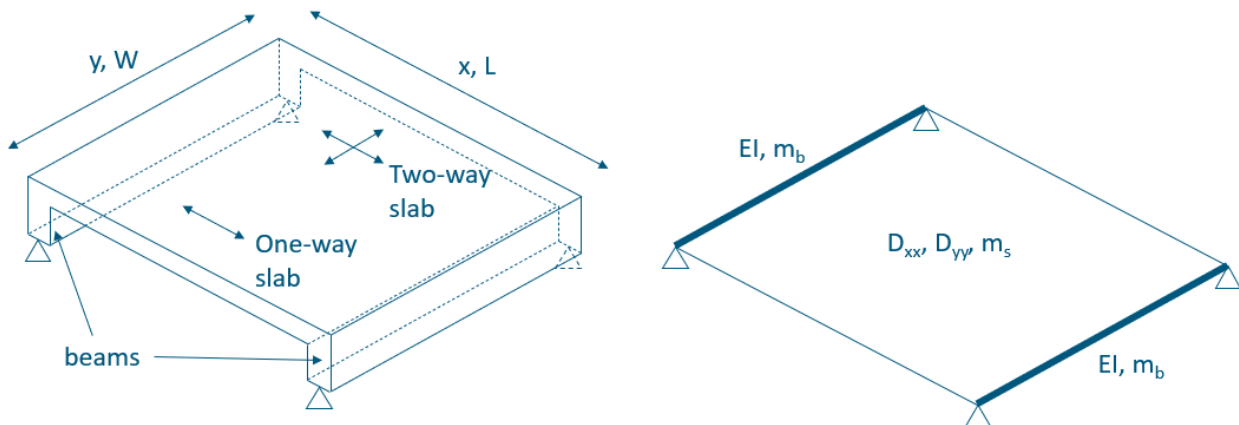


Figure 6.6: 2DOF system

$$w_b = w_{b,0} \sin\left(\frac{\pi x}{L}\right) \quad (6.15)$$

$$w_s = w_b + w_{s,0} \sin\left(\frac{\pi x}{L}\right) \sin\left(\frac{\pi y}{W}\right) \quad (6.16)$$

There are two main methods in engineering to derive the equations of motion. One method is following the Newtonian mechanics and the other method is following the Lagrangian mechanics. Newtonian mechanics can be convenient for simple cases that lead to a lumped mass matrix. The mass matrix is lumped when there are non-zero terms only on the diagonal. The masses do not interact with each other. The interaction might take place in the stiffness matrix. When there is coupling in the mass matrix the Newtonian method to derive the equations of motion becomes rather complicated. In that case, Lagrangian mechanics is the better choice. This method solves almost every mechanics problem and is in many cases faster than Newtonian mechanics.

The Lagrangian \mathcal{L} is defined as (6.17). The \mathcal{K} in this equation is the kinetic energy in the system and depends on the velocities of the masses. \mathcal{U} is the strain energy and depends on the movement of the masses.

$$\mathcal{L} = \mathcal{K} - \mathcal{U} \quad (6.17)$$

The Euler-Lagrange equation is formulated in (6.18). Essentially, this equation is a reformulation of Newton's second law ($F=ma$).

$$\frac{d}{dt} \left(\frac{\partial \mathcal{L}}{\partial \dot{w}_i} \right) = \frac{\partial \mathcal{L}}{\partial w_i} \quad (6.18)$$

The right-hand side of (6.18) are called the generalized forces. The Euler-Lagrange equation only incorporates conservative forces. Conservative forces are independent of the path taken. A spring force is an example of a conservative force. Non-conservative forces do depend on the path taken and cannot be derived from the energy in the system. An applied force is an example of a non-conservative force. They must be included manually in the Euler-Lagrange equation. After inserting (6.17) in (6.18) and including the work done by the applied force, (6.19) is obtained. The work done by the applied force is denoted as \mathcal{W} .

$$\frac{d}{dt} \left(\frac{\partial \mathcal{K}}{\partial \dot{w}_i} \right) + \frac{\partial \mathcal{U}}{\partial w_i} = \frac{\partial \mathcal{W}}{\partial w_i} \quad (6.19)$$

The kinetic energy in the system is determined and evaluated in (6.20). A coupling between the mass of the beams and the mass of the slab becomes visible after evaluating the integral.

$$\begin{aligned} \mathcal{K} &= 2 \cdot \frac{1}{2} m_b \int_0^W \dot{w}_b^2 dy + \frac{1}{2} m_s \int_0^W \int_0^L \dot{w}_s^2 dx dy \\ \mathcal{K} &= \frac{W}{2} m_b \dot{w}_{b,0}^2 + \frac{LW}{4} m_b \left(\dot{w}_{b,0}^2 + \dot{w}_{s,0}^2 + \frac{16}{\pi^2} \dot{w}_{b,0} \dot{w}_{s,0} \right) \end{aligned} \quad (6.20)$$

The strain energy in the system is the integral of moment-curvature relationship over the length and width of the slab and beam. This involves the Poisson's ratio ν and rigidities D_ν and D_{xy} . The meaning of those parameters is further explained in chapter 6. When evaluating the integrals, it happens that those parameters cancel out.

$$\begin{aligned}
 u &= 2 \cdot \frac{1}{2} \int_0^W EI \left(\frac{d^2 w_b}{dy^2} \right)^2 dy + \frac{1}{2} \int_0^W \int_0^L D_{xx} \left(\frac{d^2 w_p}{dy^2} \right)^2 + D_{yy} \left(\frac{d^2 w_p}{dy^2} \right)^2 + 2\nu D_{xy} \frac{d^4 w_p}{dx^2 dy^2} + 2(1-\nu) D_{xy} \left(\frac{d^2 w_p}{dx dy} \right)^2 dx dy \\
 \mathcal{U} &= \frac{\pi^4}{2W^3} EI w_{b,0}^2 + \frac{\pi^4}{4L^3 W^3} (D_{xx} W^4 w_{s,0}^2 + D_{yy} L^4 w_{b,0}^2)
 \end{aligned} \quad (6.21)$$

The amount of work done is only dependant on the area on which the distributed pressure acts. The work is formulated and evaluated in (6.22).

$$\begin{aligned}
 \mathcal{W} &= p \int_0^W \int_0^L w_s^2 dx dy \\
 \mathcal{W} &= \frac{2LW}{\pi} p w_{b,0} + \frac{2LW}{\pi} p w_{s,0}
 \end{aligned} \quad (6.22)$$

After applying Lagrange's equation (6.17) the equations of motion in (6.23) are obtained. The equations are displayed in matrix form. The first matrix on the left-hand side is called the mass matrix **M**. The second matrix on the left-hand side is called the stiffness matrix **K**. The right-hand side vector is the force vector **F**.

$$\begin{bmatrix} 2 \cdot \frac{1}{2} W m_b + \frac{1}{2} L W m_s & \frac{4}{\pi^2} L W m_s \\ \frac{4}{\pi^2} L W m_s & \frac{1}{2} L W m_s \end{bmatrix} \begin{bmatrix} \ddot{w}_{b,0} \\ \ddot{w}_{s,0} \end{bmatrix} + \begin{bmatrix} 2 \frac{\pi^4 EI}{2 W^3} + \frac{\pi^4 L D_{yy}}{2 W^3} & 0 \\ 0 & \frac{\pi^4 W D_{yy}}{2 L^3} \end{bmatrix} \begin{bmatrix} w_{b,0} \\ w_{s,0} \end{bmatrix} = \begin{bmatrix} \frac{2}{\pi} L W p \\ \frac{2}{\pi} L W p \end{bmatrix} \quad (6.23)$$

The mass matrix, stiffness matrix and force matrix are generalized in (6.24), (6.25) and (6.26). This is proven by following the modal analysis approach as described in chapter 3.5 in (Biggs, 1964).

$$\mathbf{M} = \begin{bmatrix} 2K_{M,b,y} W m_b + K_{M,s,y} L W m_s & K_{M,s,xy} L W m_s \\ K_{M,s,xy} L W m_s & K_{M,s,xx} L W m_s \end{bmatrix} \quad (6.24)$$

$$\mathbf{K} = \begin{bmatrix} 2K_{L,b} W k_b + K_{L,s} L W k_{s,yy} & 0 \\ 0 & K_{L,s} L W k_{s,xx} \end{bmatrix} \quad (6.25)$$

$$\mathbf{F} = \begin{bmatrix} K_{L,s} L W p \\ K_{L,s} L W p \end{bmatrix} \quad (6.26)$$

The shape of the slab deflection is approached as the superposition of the deflection function of the beam independent of the slab and the deflection function of the slab independent of the beam. Both deflection functions can be considered as 2 separate modal shapes. Therefore, the shape of the slab deflection can be expressed in the discretised form (6.27). ϕ_{ra} is the assumed deflection of mass r . ϕ_{rm} is the deflection coordinate for the m^{th} mode and ψ_m is the participation factor for the m^{th} mode

$$\phi_{ra} = \sum_{m=1}^N \psi_m \phi_{rm} \quad (6.27)$$

If both sides of (6.27) are multiplied by $M_r \phi_{rq}$, where ϕ_{rq} is the deflection coordinate for the q^{th} mode, and summed up over all masses, (6.28) is obtained.

$$\sum_{r=1}^j M_r \phi_{ra} \phi_{rq} = \sum_{r=1}^j \sum_{m=1}^N \psi_m M_r \phi_{rm} \phi_{rq} \quad (6.28)$$

The right-hand side of (6.28) is the effective mass. This is specified for a slab with indices i and j for x -direction and j -direction respectively. N runs from 1 to 2.

$$M_{s,q=1}^* = \sum_{i=0}^{N_i} \sum_{j=0}^{N_j} \sum_{m=1}^2 K_{M,s,mq} M_{i,j} \phi_{i,j,m} \phi_{i,j,q} = \sum_{i=0}^{N_i} \sum_{j=0}^{N_j} K_{M,s,11} M_{i,j} \phi_{i,j,1}^2 + K_{M,21} M_{i,j} \phi_{i,j,2} \phi_{i,j,1} \quad (6.29)$$

$$M_{s,q=2}^* = \sum_{i=0}^{N_i} \sum_{j=0}^{N_j} \sum_{m=1}^2 K_{M,s,mq} M_{i,j} \phi_{i,j,m} \phi_{i,j,q} = \sum_{i=0}^{N_i} \sum_{j=0}^{N_j} K_{M,s,12} M_{i,j} \phi_{i,j,1} \phi_{i,j,2} + K_{M,s,22} M_{i,j} \phi_{i,j,2}^2 \quad (6.30)$$

$$M_{b,q=1}^* = \sum_{i=0}^{N_i} \sum_{j=0}^{N_j} \sum_{m=1}^1 K_{M,b,mq} M_{0,j} \phi_{i,j,m} \phi_{i,j,q} = \sum_{i=0}^{N_i} \sum_{j=0}^{N_j} K_{M,b,11} M_{0,j} \phi_{0,j,1}^2 \quad (6.31)$$

6.3.2 Numerical solution

The numerical solution for a 2DOF mass-spring system is similar to the numerical solution for a SOD mass-spring system. The difference is that now matrix operation must be performed. The tangent matrix K_t (6.36) is introduced. This matrix includes the amount of change in stiffness after each time-step. Equations (6.32) - (6.39) are similar to (6.8) - (6.14), but written in matrix form notation

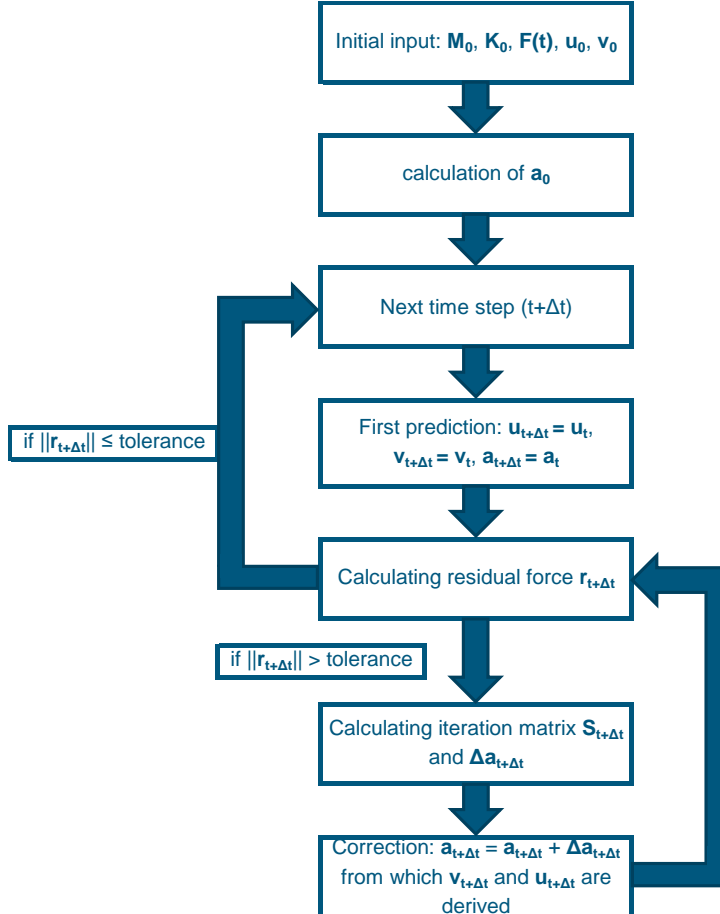


Figure 6.7: Flowchart 2DOF time-marching Newton-Raphson scheme

$$\mathbf{v}_{t+\Delta t} = \mathbf{v}_t + \Delta t((1 - \gamma)\mathbf{a}_t + \gamma\mathbf{a}_{t+\Delta t}) \quad (6.32)$$

$$\mathbf{u}_{t+\Delta t} = \mathbf{u}_t + \Delta t\mathbf{v}_t + \frac{1}{2}(\Delta t)^2((1 - 2\beta)\mathbf{a}_t + 2\beta\mathbf{a}_{t+\Delta t}) \quad (6.33)$$

$$\mathbf{r}_{t+\Delta t} = \mathbf{K}_M\mathbf{M}\mathbf{a}_{t+\Delta t} + \mathbf{C}\mathbf{v}_{t+\Delta t} + \mathbf{K}_L\mathbf{F}_{s,t+\Delta t} - \mathbf{K}_L\mathbf{F}_{t+\Delta t} \quad (6.34)$$

$$\mathbf{S}_{t+\Delta t} = \mathbf{K}_M\mathbf{M} + \gamma\Delta t\mathbf{C} + \beta(\Delta t)^2\mathbf{K}_t \quad (6.35)$$

$$\mathbf{K}_t = \begin{bmatrix} 2K_{L,b}W \frac{F_{s,b,t+\Delta t} - F_{s,b,t}}{u_{b,t+\Delta t} - u_{b,t}} + K_{L,s}LW \frac{F_{s,s,t+\Delta t} - F_{s,s,t}}{u_{s,t+\Delta t} - u_{s,t}} & 0 \\ 0 & K_{L,s}LW \frac{F_{s,s,t+\Delta t} - F_{s,s,t}}{u_{s,t+\Delta t} - u_{s,t}} \end{bmatrix} \quad (6.36)$$

$$\Delta\mathbf{a}_{t+\Delta t} = -\mathbf{S}_{t+\Delta t}^{-1} \cdot \mathbf{r}_{t+\Delta t} \quad (6.37)$$

$$\mathbf{a}_{t+\Delta t,n} = \mathbf{a}_{t+\Delta t} + \Delta\mathbf{a}_{t+\Delta t} \quad (6.38)$$

$$\mathbf{a}_0 = \mathbf{M}_0^{-1} \cdot (\mathbf{F}_0 - \mathbf{C}_0\mathbf{v}_0 - \mathbf{K}_0\mathbf{w}_0) \quad (6.39)$$

7 Experimental validation and calibration

The presented method in chapter 5 (finite difference model) and chapter 6 (mass-spring system) are validated by an experimental study. The full reports of the validation are included in Appendix I, Appendix II, and Appendix III. A compact version of the appendices is presented in this chapter

7.1 Validation experiment 1

In this validation experiment, numerous experiments are performed and compared with engineering tools. The experiments are conducted at the Ernst-Mach-Institut (EMI) in Germany using a shock tube. A shock tube simulates a blast load under controlled conditions. Two types of experiments are performed: one that represents a close-in detonation and one that represents far field detonations. The far field detonation is what this research focusses on. The engineering tool used for the far field detonations is a pressure-impulse diagram.

7.1.1 Experiment observations

Four beams are analysed by (Riedel et al., 2009) of which one fails. The failed beam is the bottom picture in Figure 7.1. The top picture is the damaged plate, as indicated in the graph. The last two beams remain intact, according to the graph.

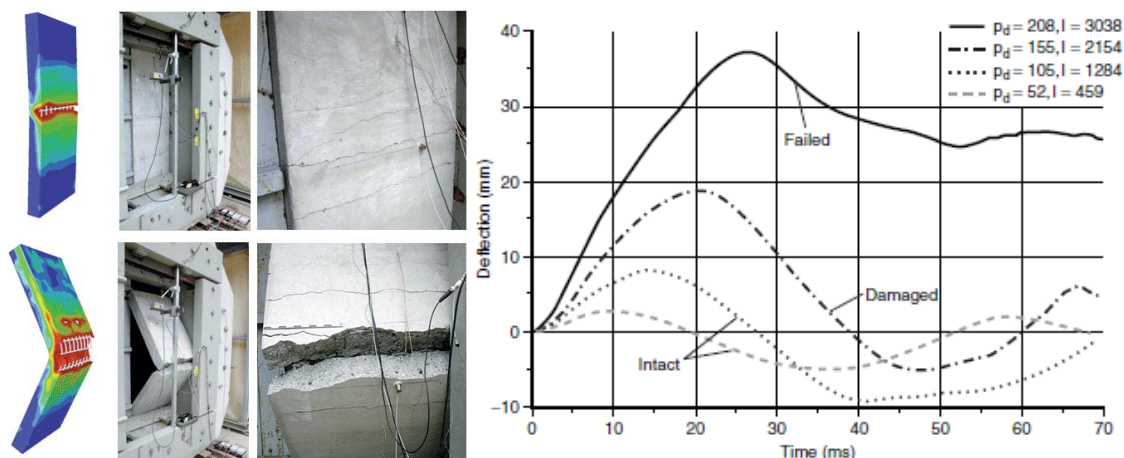


Figure 7.1: Walls after the blast. Top wall: NRC-3. Bottom wall: NRC-4

7.1.2 Moment-curvature relationship

The constructed M- κ graph as described in chapter 4.1 is compared with the M- κ graph retrieved from FEM analysis. The comparison is showed in Figure 7.2. The M- κ graph stops, in this case, when the reinforcement fails. This is due to the relative ultimate strain of the applied reinforcement steel type BSt 500S.

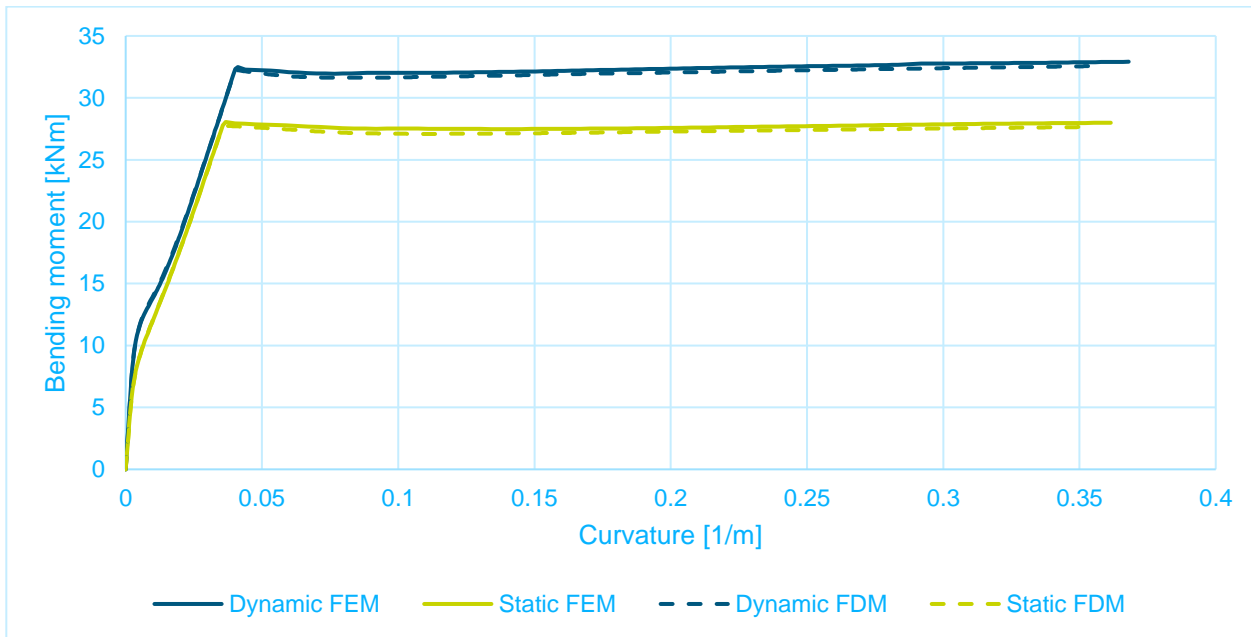


Figure 7.2: Moment-curvature relationship EPR4 (dynamic) and static

7.1.3 Force-deflection relationship

The M- κ graph is an input for the FDM model, which constructs the F-u graph. The F-u graph in the FDM model and the FEM model are similar, but the FDM model stops earlier. The FDM model stops all the available energy according to the M- κ graph is used. The F-u graph is constructed in a force-controlled manner. Therefore, the bending moment can only increase or remain equal. The M- κ graph is slightly adjusted in such a way that it is always increasing while retaining the same area under the M- κ graph.

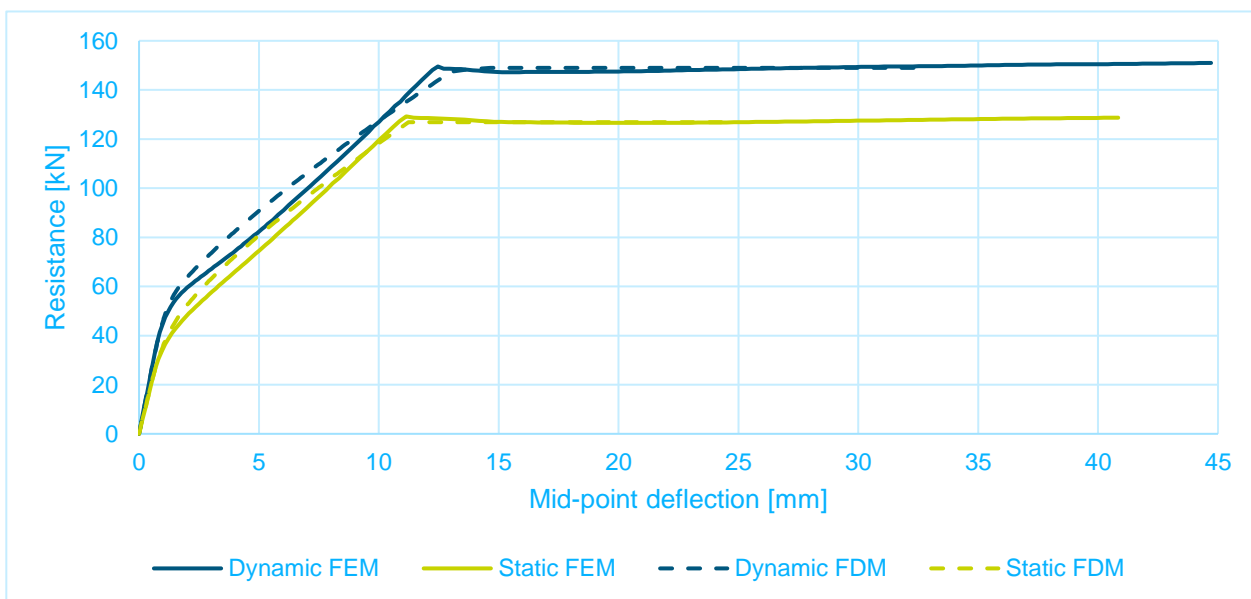


Figure 7.3: F-u graph for NRC-4 (dynamic) and the static case

7.1.4 Nonlinear time history analysis

Figure 7.4 presents the results of the SDOF mass-spring system analyses compared to the experimental results. Figure 7.5 present the NLTH analyses in DIANA compared to the SDOF mass-spring system results

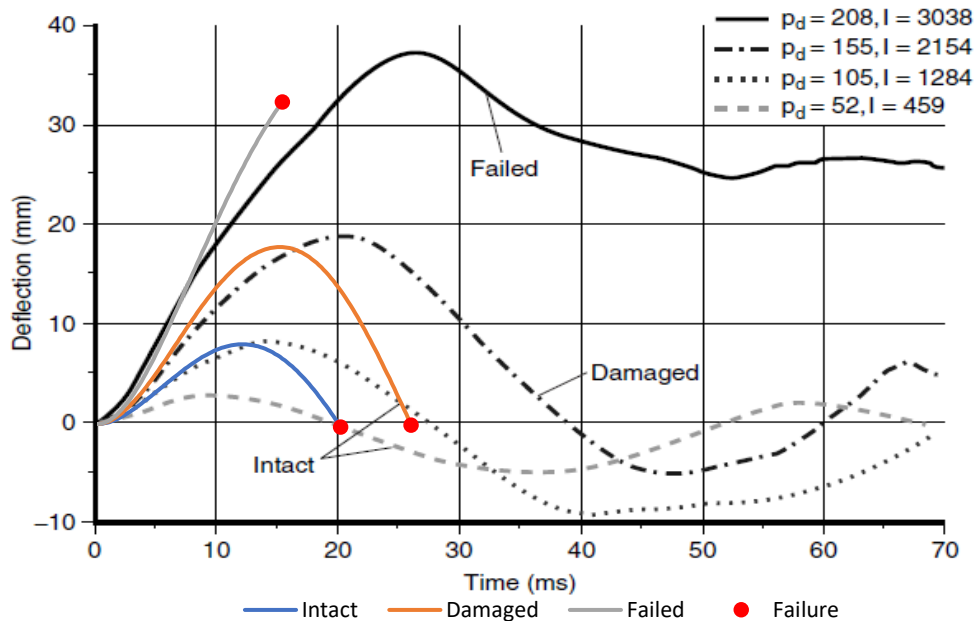


Figure 7.4: Comparison with the experiment

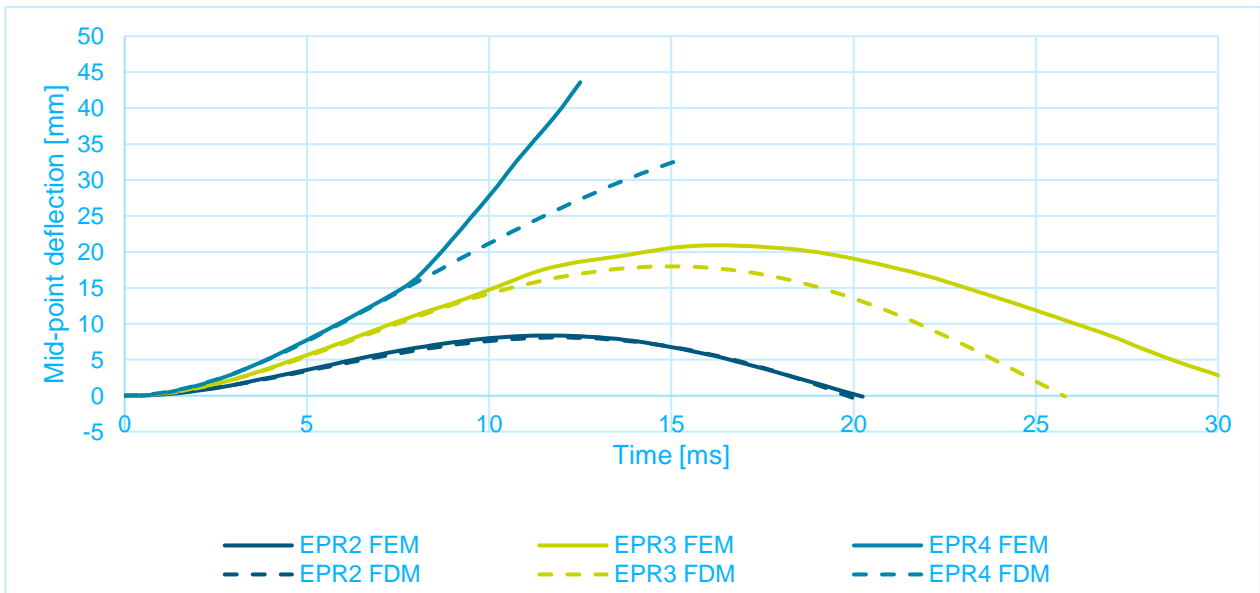


Figure 7.5: NLTH analyses

7.2 Validation experiment 2

This validation experiment presents the results of the experiment conducted in Woomera, Australia in 2004 (Ngo, Mendis, & Krauthammer, 2007). The goal of the experiment is to investigate the structural behaviour of concrete for heavy explosions. The blast is generated by a 6 tonnes TNT equivalent explosion with a standoff distance of 40 m. This is equivalent to the scaled distance Z of $2.3 \text{ m/kg}^{1/3}$, high enough to be considered 'far field'.

7.2.1 Experiment observations

There is no deflection-time history graph available for panel 4. Some observations are described in (Ngo, Mendis, & Krauthammer, 2007):

- Concrete is crushed and a cavity of 100 mm width and 30 mm depth is formed vertically at the midspan
- A permanent deflection of 142 mm is measured.
- At the rear surface, an approximately 8-mm-wide crack at the midspan is observed.

The concrete panel after the blast trial is shown in Figure 7.6. Figure 7.7 is a scaled illustration of the observations. At the given permanent deflection, the support rotation is 8° .



Figure 7.6: Panel 4 after the blast

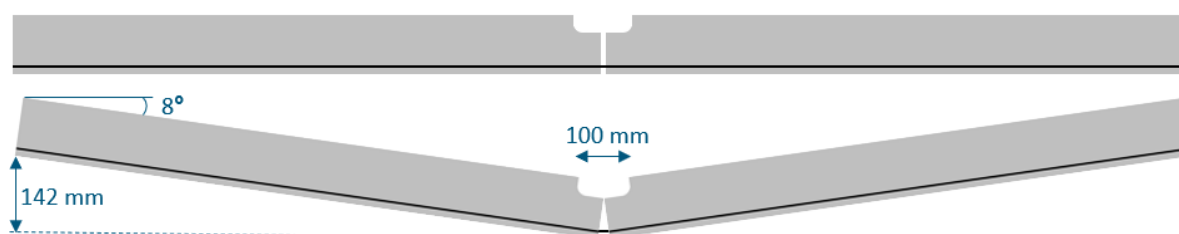


Figure 7.7: Scaled illustration of the observations

7.2.2 Moment-curvature relationship

The M- κ graph is manually constructed and shown in Figure 7.8. Noticeable is that the manually constructed M- κ graph fails earlier than the M- κ graph obtained in FEM. This is because the concrete crushes before the reinforcement fails, whereas the failure mechanism in the FEM analysis is reinforcement failure.

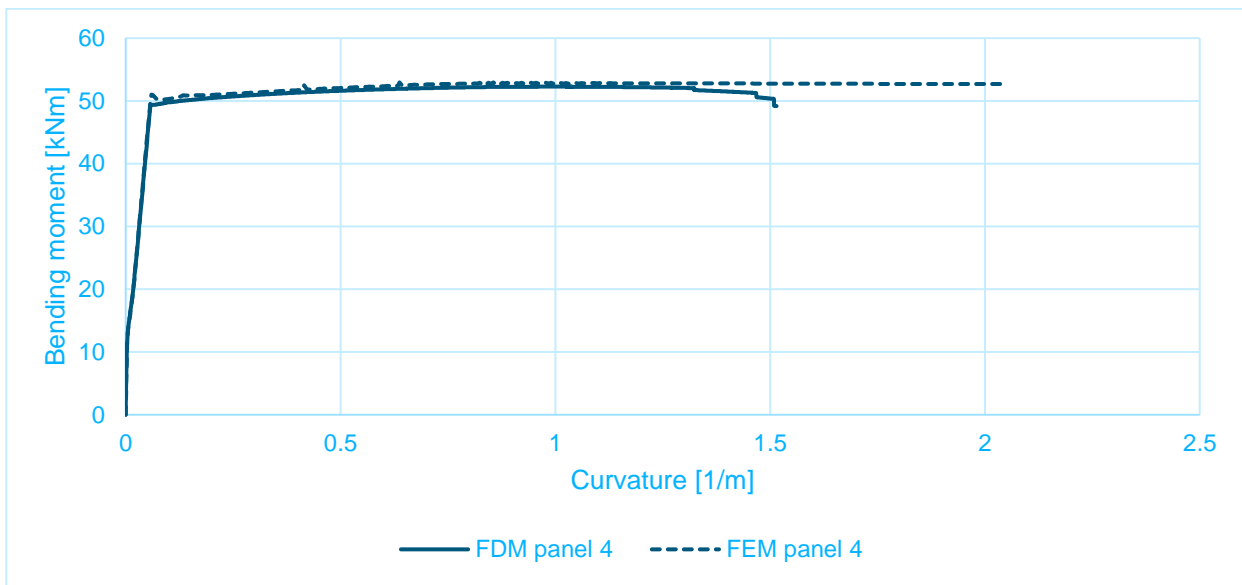


Figure 7.8: M- κ graph for panel 4

7.2.3 Force-deflection relationship

The force-deflection (F-u) is shown in Figure 7.9. The permanent deflection is 142 mm, which does not lead to failure according to the F-u graph.

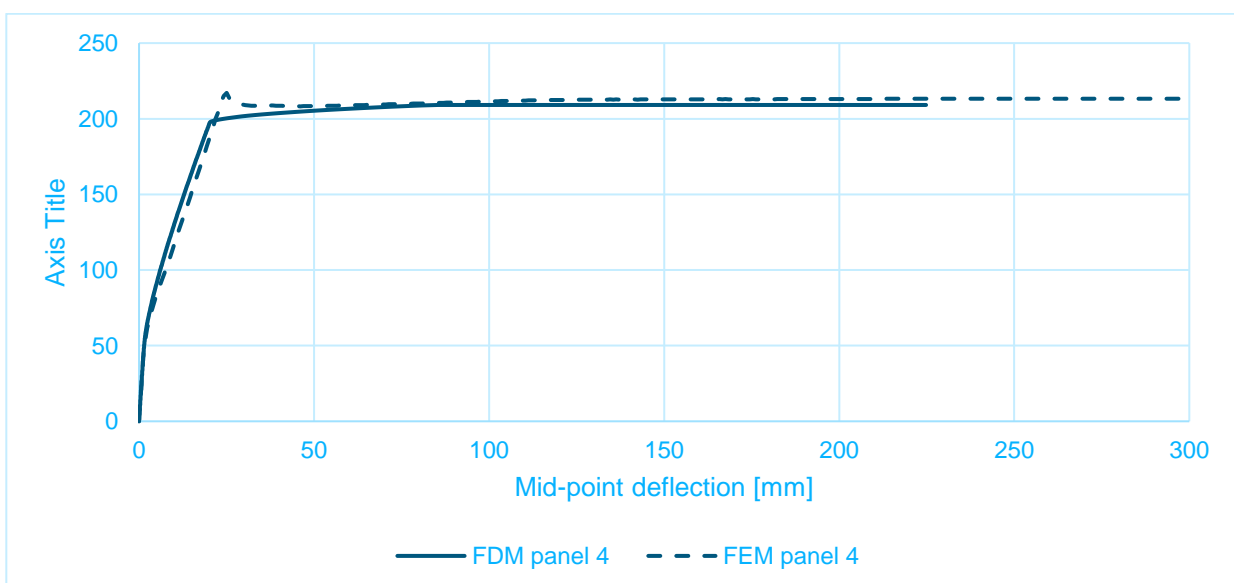


Figure 7.9: F-u graph for panel 4

7.2.4 Nonlinear time history analysis

The result of the mass-spring system analysis is shown in Figure 7.10. The results of the SDOF mass-spring system are close to the results of the nonlinear time history analysis performed in DIANA. The deflection goes beyond the permanent deflection, which is as expected. Due to the inward acceleration after reaching the maximum deflection and possible effects of the negative phase of the blast (partial vacuum), the slab moves back.

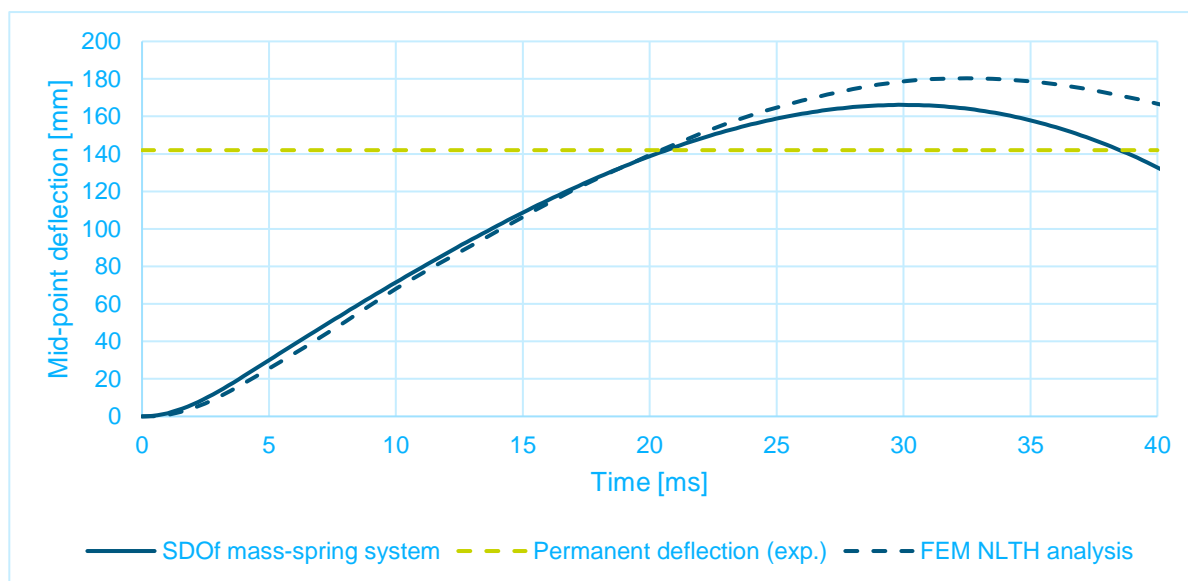


Figure 7.10: Deflection-time history graph of the mass-spring system

7.3 Validation experiment 3

In this validation experiment, the treatment of relatively low scaled distances according to the Hopkinson-Cranz scaling law (2.2) are analysed. Detonations with low scaled distances result in a nonlinear pressure distribution over the beam. The reviewed scaled distance is large enough to be considered as far field detonation.

7.3.1 Experiment observations

The UFC 3-340-02 (Department of Defence, US, 2008) considers scaled distances above $1.2 \text{ m/kg}^{1/3}$ explosions in the 'far field' design range. This does not necessarily mean that blast load categorised in the far field design range leads to a uniform pressure distribution. This is showed in (Wu et al., 2009), where the pressure is measured in the middle of the beam and near the support. These pressure measurements are used to predict the pressure distribution for the beam reported in (Pham, 2015).

The load is more concentrated on the middle of the beam, leading to a different load factor and mass factor. The simplification shown in Figure 7.11 is used in the analysis. The influence of the nonlinear pressure distribution in Figure 7.11 is illustrated in equations (7.1) - (7.4).

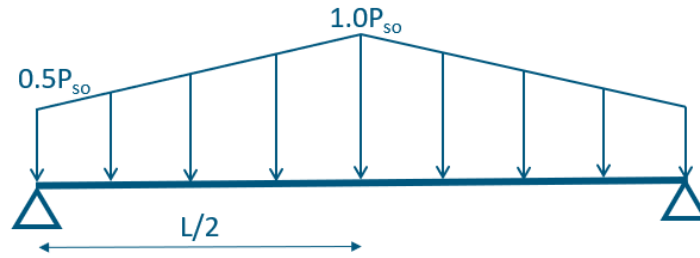


Figure 7.11: simplification of the nonlinear pressure distribution

$$P(x, P_{so}) = \frac{P_{so}}{2} + \frac{P_{so}}{2} \frac{2x}{L} \quad (7.1)$$

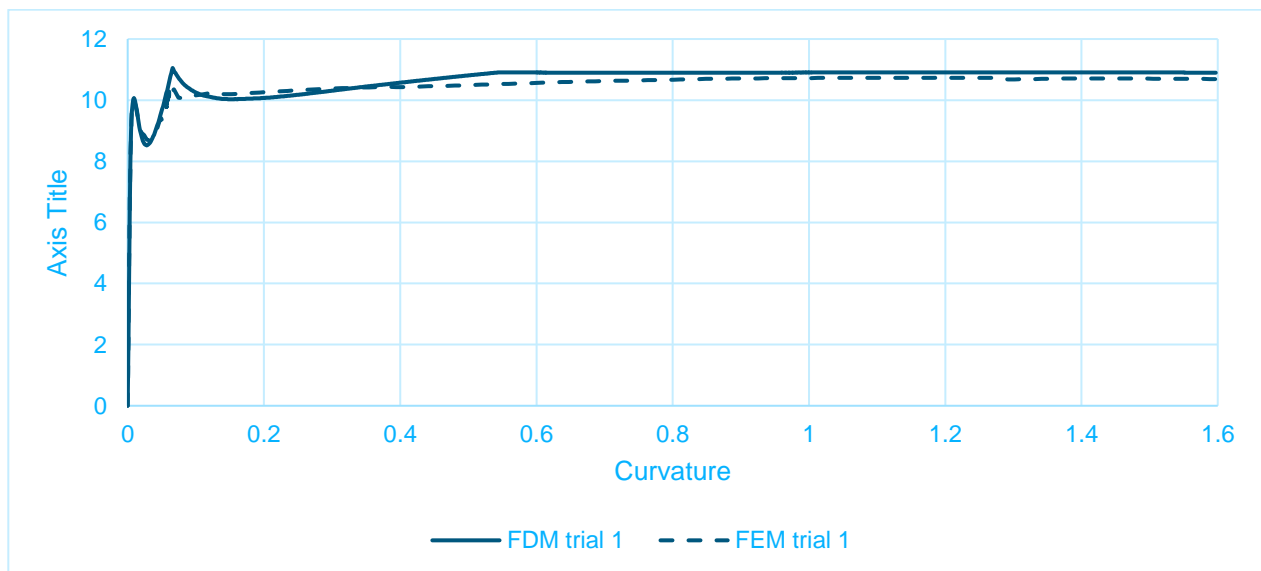
$$\phi(x) = \frac{2x(16x^4 + 40Lx^3 - 120L^2x^2 + 65L^4)}{41L^5} \quad (7.2)$$

$$K_L = \frac{\int_0^{L/2} P(x, P_{so} = 1) \phi(x) dx}{\int_0^{L/2} P(x, P_{so} = 1) dx} = 0.696 \quad (7.3)$$

$$K_M = \frac{\int_0^{L/2} \phi(x)^2 dx}{L/2} = 0.502 \quad (7.4)$$

7.3.2 Moment-curvature relationship

The M- κ graph is manually constructed and shown in Figure 7.12. The first dip indicates cracking. The second dip is where the reinforcement is yielding.

Figure 7.12: M- κ graph for Trial 1

7.3.3 Force-deflection relationship

The F-u graph is shown in Figure 7.13. The FEM analysis is force-controlled with arc-length turned on. This allows for local dips in the F-u graph. The FDM model is force-controlled without arc-length. This limits the accuracy of the F-u graph obtained in the FDM model.

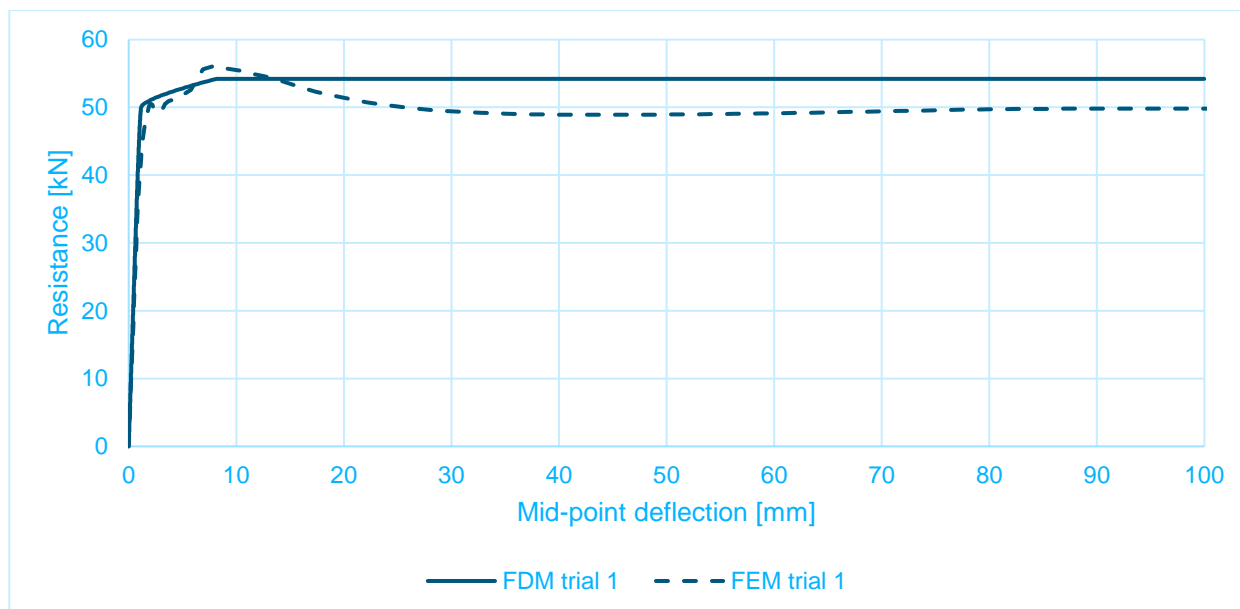


Figure 7.13: F-u graph for Trial 1

7.3.4 Nonlinear time history analysis

Three ways of specifying the unloading stiffness are considered and compared, as indicated in Figure 7.14 and the mass-spring results in Figure 7.15. Based on this research, the unloading path 2 is the best choice. For unloading stiffness 2, the deflection is slightly overestimated for the maximum inward and maximum outwards deflection. It should be noted that this requires more in-depth research for better insight in the unloading branch.

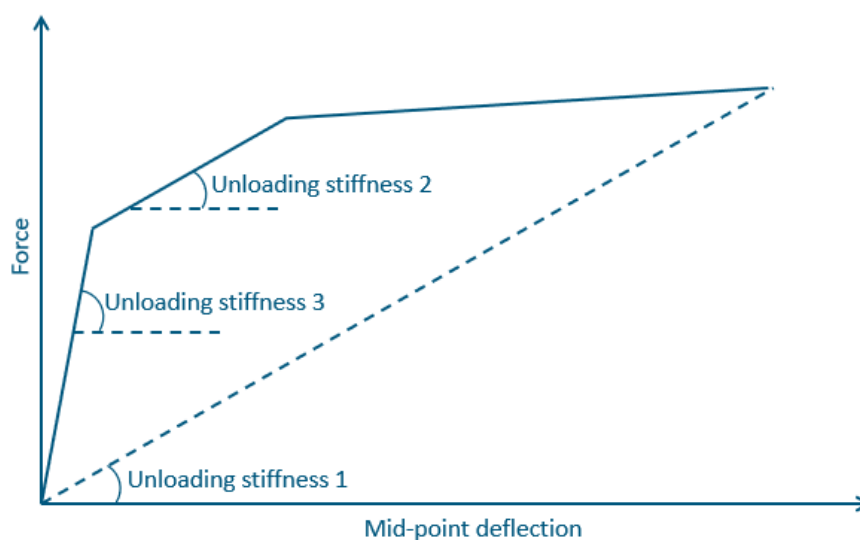


Figure 7.14: Unloading stiffnesses

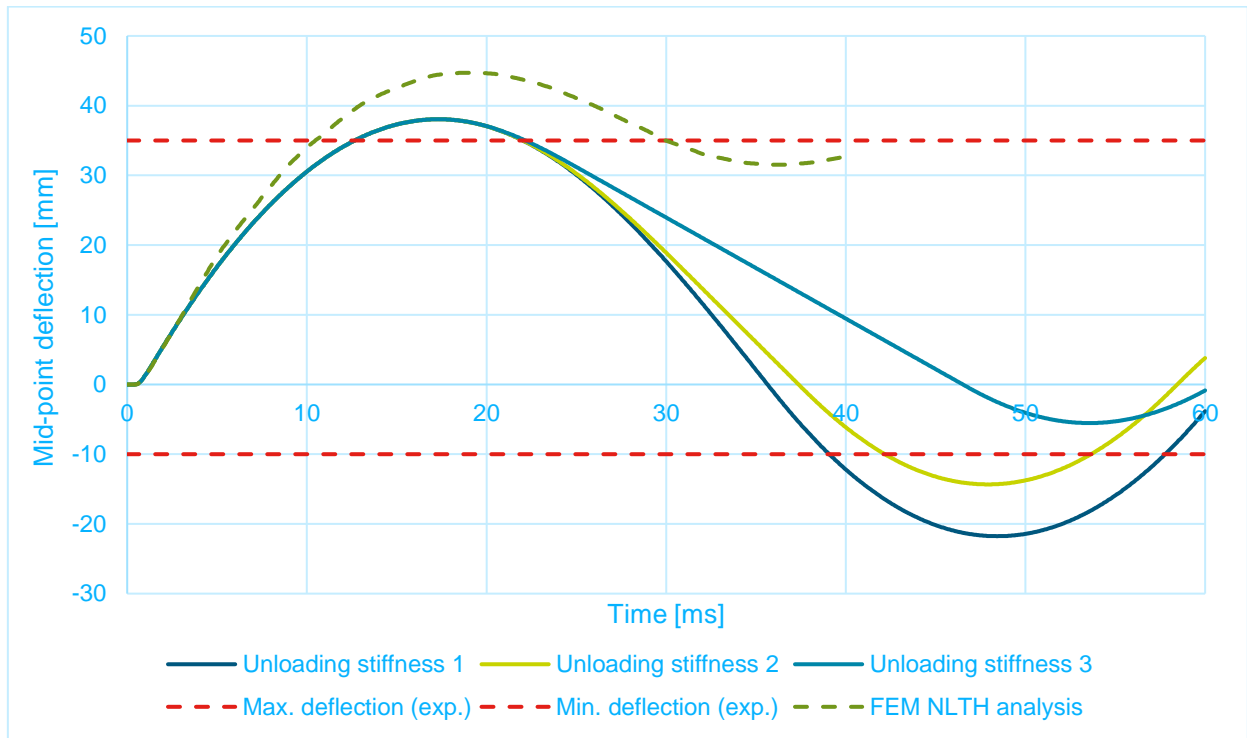


Figure 7.15: Mass-spring system deflection for Trial 1

The load factor and mass factor that follows from the analysis in Appendix III is shown in Figure 7.16. The load factor and mass factor have the initial value as predicted in equations (7.3) and (7.4). This is where the one-way element is still elastic.

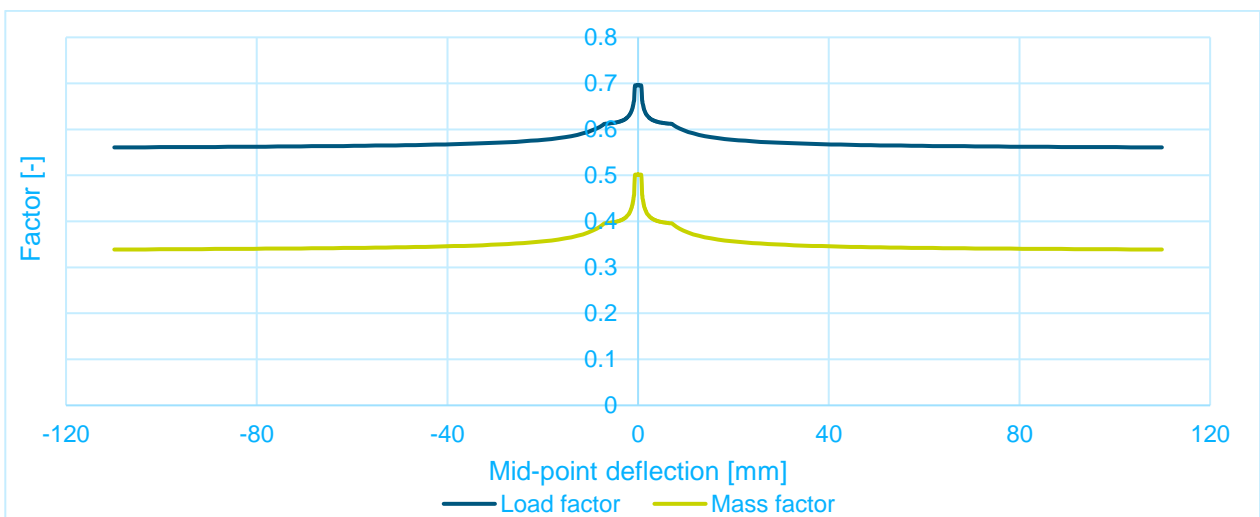


Figure 7.16: mass factor and load factor for Trial 1

8 Case study

This chapter contains the blast resistance assessment of building Admin Old. This building section is constructed in 1960 and has an in-situ cast reinforced concrete structural system.

A risk of a blast scenario is present in the area of Admin Old. The resulting blast loads are not incorporated in the original design. In 2017, Royal HaskoningDHV performed a high-level blast assessment of the building mainframe and concluded that based on the simplified analysis the main structure is not sufficient to withstand the specified blast load.

The drawings of the building are given in Figure 8.1, Figure 8.2 and Figure 8.3. Figure 8.4 shows the vertical load bearing system

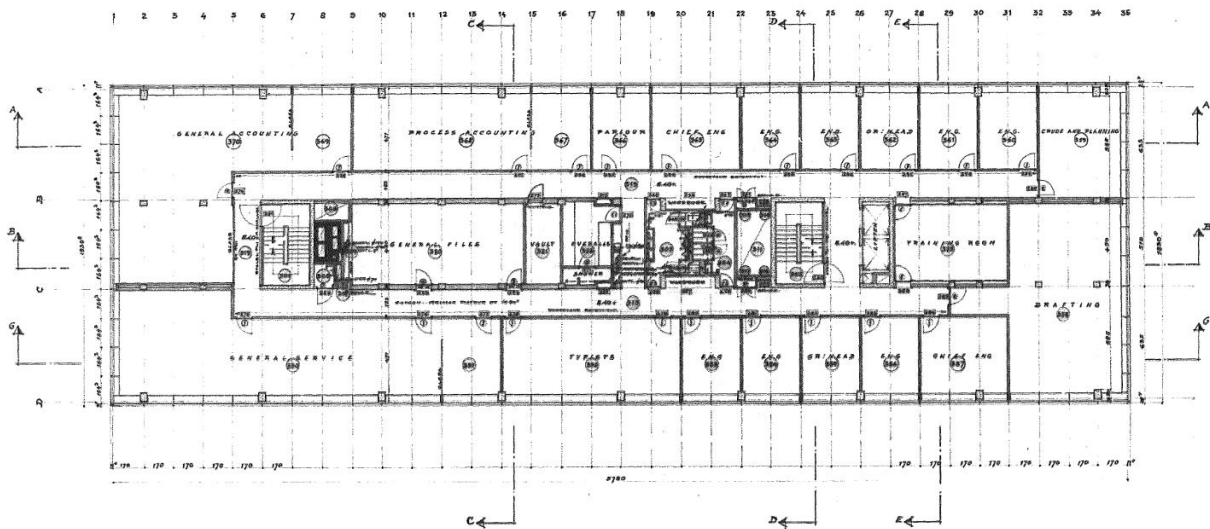


Figure 8.1: Floor plan Admin Old

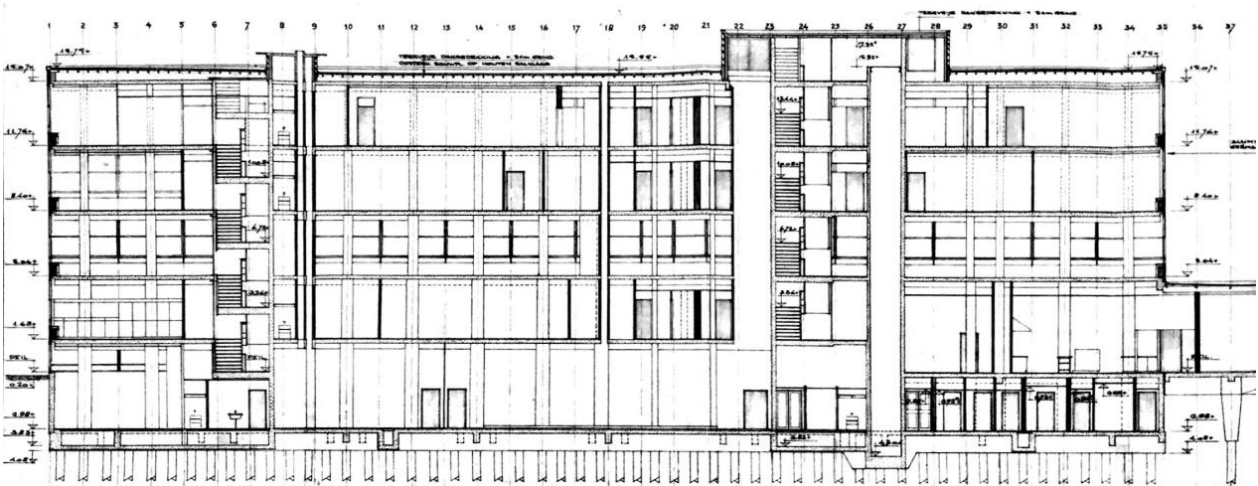


Figure 8.2: Cross section Admin Old

The goal of this research is to compare the existing assessment of the building with the experimental observations and methods described in throughout this report. The focus is on the roof slab, which is supported by beams. When the beams are infinitely stiff, the slab will behave as a one-way slab. In that case, a SDOF mass-spring system will suffice. When the deflection of the beams has a considerable contribution to the mid-point deflection of the slab, the total system must be approached as a 2DOF mass-spring system. The beam stiffness which can be considered as infinitely stiff is determined in this chapter.

The geometry of the concrete roof slab is indicated in Figure 8.6

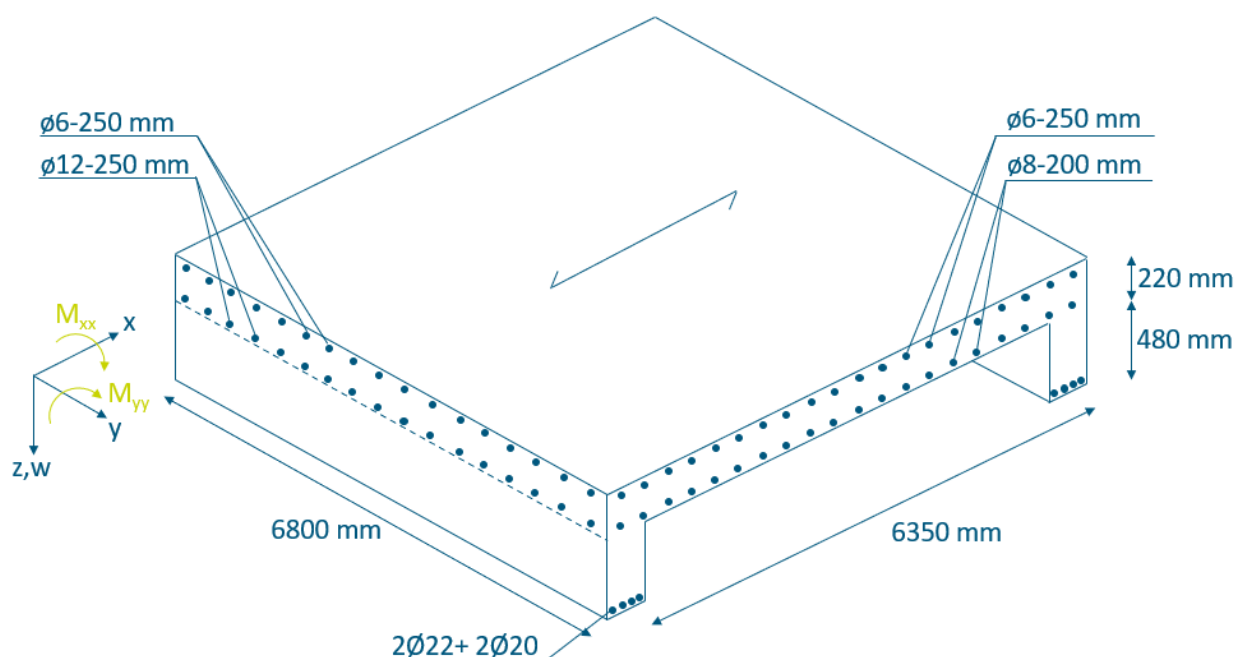


Figure 8.6: Geometry of the slab (not scaled)

8.1 Method

The roof is subjected to its dead weight. This has significant influence on the results since the dead weight already creates cracks in the roof without any load being applied yet. Since the building is constructed in 1960, the structural elements are most likely more cracked due to previous loading of the structure, such as a layer of snow on the roof. For convenience, the load history, apart from dead weight, is not accounted for in the initial stiffness state. This is justified by the following counteractive choices in the analysis of the roof:

- Concrete gets stronger in time. By using the 28-days material parameters, the calculation is on the safe side.
- The roof is slightly fixed at the supports. The structural scheme of the roof is simply supported. This is a conservative choice

The dead weight of the roof may be incorporated as described in chapter 4-26.1 in UFC 3-340-02. The dead weight is subtracted from the total resistance of the roof. This is further explained in chapter 8.6.1. The dead weight has a negative effect on the outwards resistance and a positive effect for the rebound resistance.

In the parametric study, the slab dimensions remain the same while the supporting beams change in height and mass. For each beam used in the parametric study, a separate M- κ graph is setup. The reinforcement percentage remains equal in for all beams.

8.2 Original results

The original results are presented in Figure 8.7 (vertical deflection) and Figure 8.8 (reinforcement stress). The supporting beams do not contribute much to the total deflection of the slab. The reinforcement is clearly yielding, but only in the span direction. The deformation is scaled 20 times larger than the actual deformation.

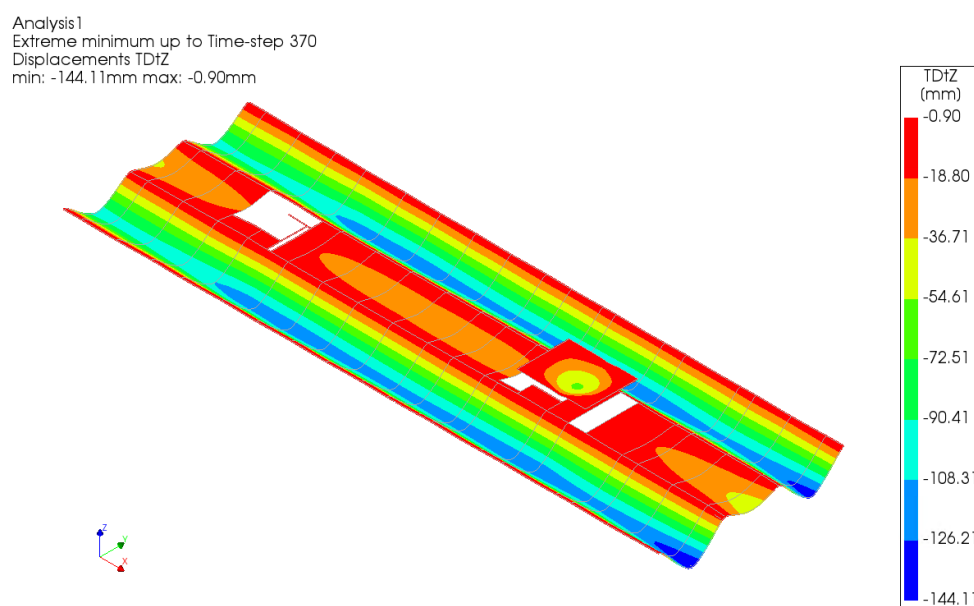


Figure 8.7: Deflection in the original results

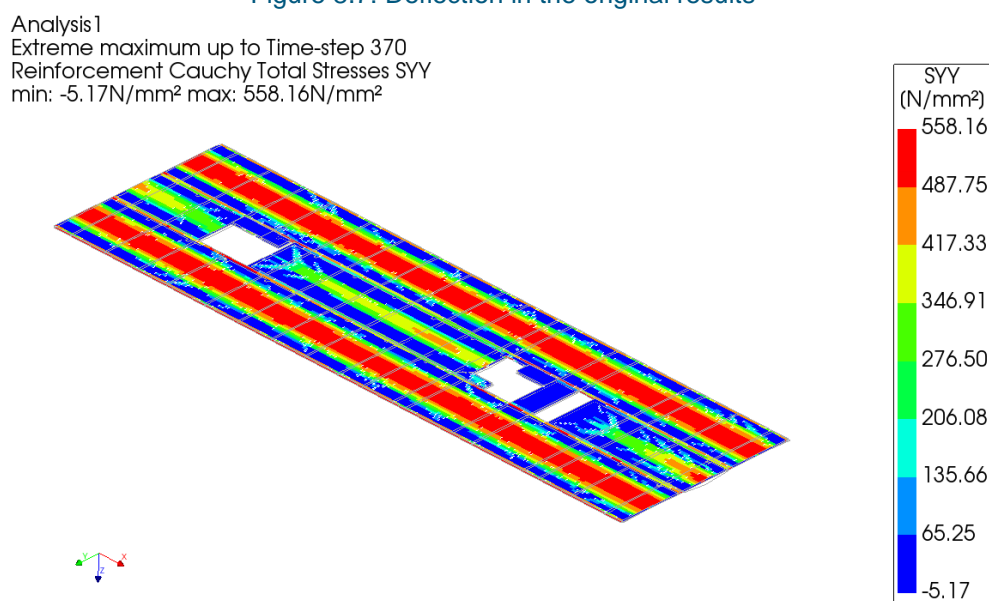


Figure 8.8: reinforcement stress in the main span direction

8.3 Parameters

The parameters used in the M- κ graph are included in Table 8.1, Table 8.2, and Table 8.3, and visualised in Figure 8.9 and Figure 8.10.

Table 8.1: Dynamic properties

Parameter	Units	Case study
Time to yield t_E	s	± 0.07
Concrete strain rate $\dot{\epsilon}_{c,avg}$	s ⁻¹	± 0.03
Steel strain rate $\dot{\epsilon}_{s,avg}$	s ⁻¹	± 0.03
DIF _c	-	1.18
DIF _t	-	1.00
DIF _E	-	1.20
DIG _{GF}	-	1.00
DIF _{GC}	-	1.18

Table 8.2: Concrete properties

Parameter	Units	Case study
Young's modulus (static / dynamic)	MPa	29962 / 35954
Initial Poisson's ratio	-	0
Mass density	Kg/m ³	2500
Tensile curve	-	Hordijk
Tensile strength (static/dynamic)	MPa	2.21 / 2.21
Crack bandwidth	mm	454
Fracture energy	N/m	133
Poisson's ratio reduction	-	Damage based
Compression curve	-	Parabolic
Compressive strength	MPa	28.00 / 33.04
Compressive fracture energy	N/m	33250 / 39235

Table 8.3: Reinforcement steel properties

Parameter	Units	Case study
Young's modulus	MPa	200000
Yield stress (static / dynamic)	MPa	550 / 613
Ultimate engineering stress (static / dynamic)	MPa	594 / 657
Ultimate engineering strain	-	0.05

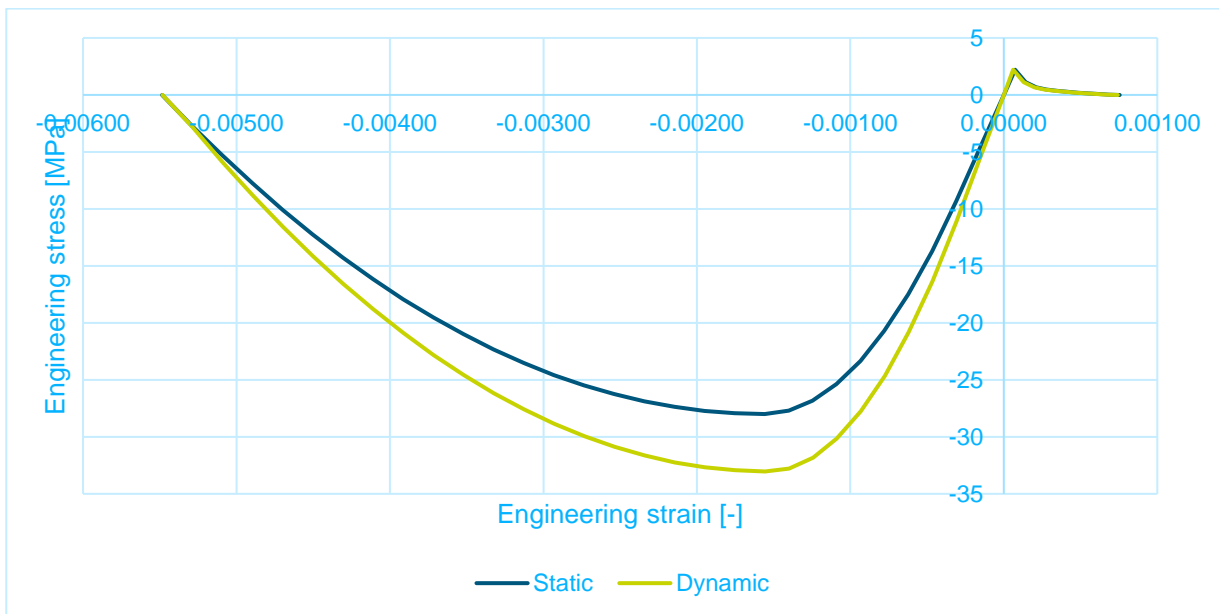


Figure 8.9: Stress-strain relationship for the concrete (h=454 mm)

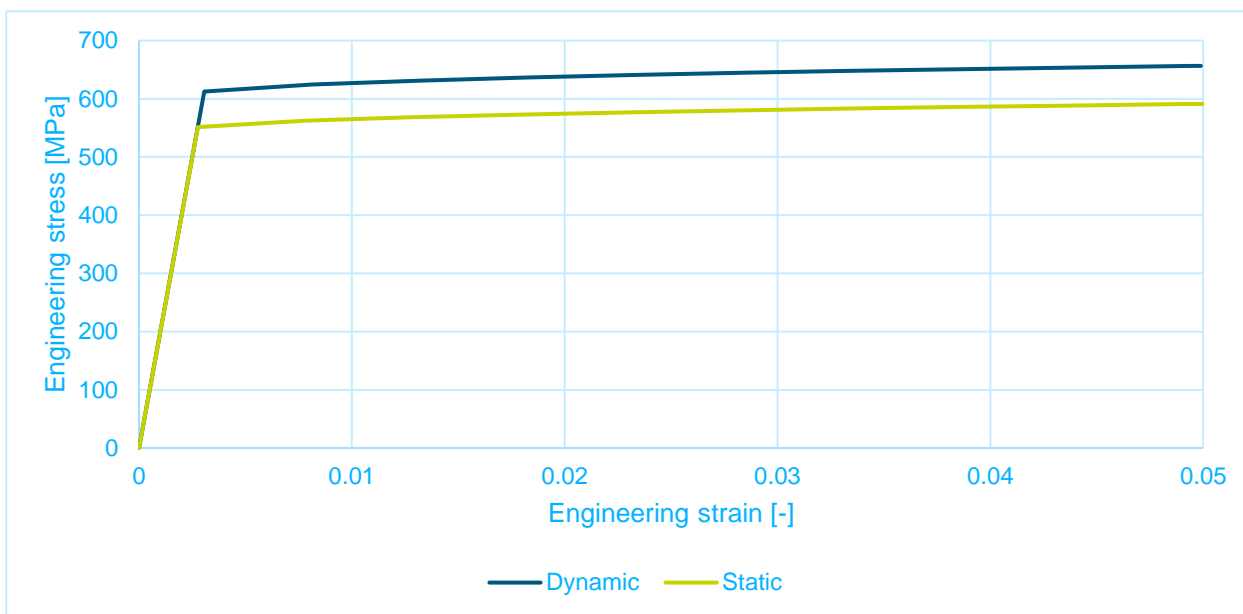


Figure 8.10: Stress-strain relationship for the reinforcement

8.4 Applied force

The applied force is shown in Figure 8.11. The peak incident overpressure is 13.38 kPa. The positive phase duration is 106 ms, resulting in an impulse of 700.05 kPa ms.

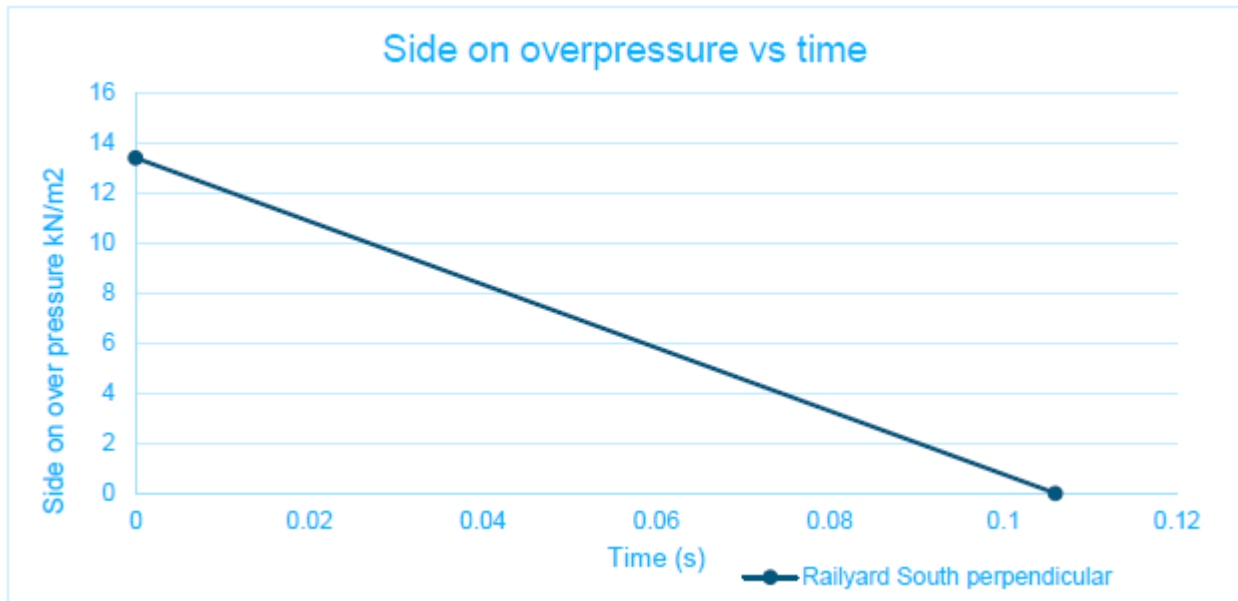


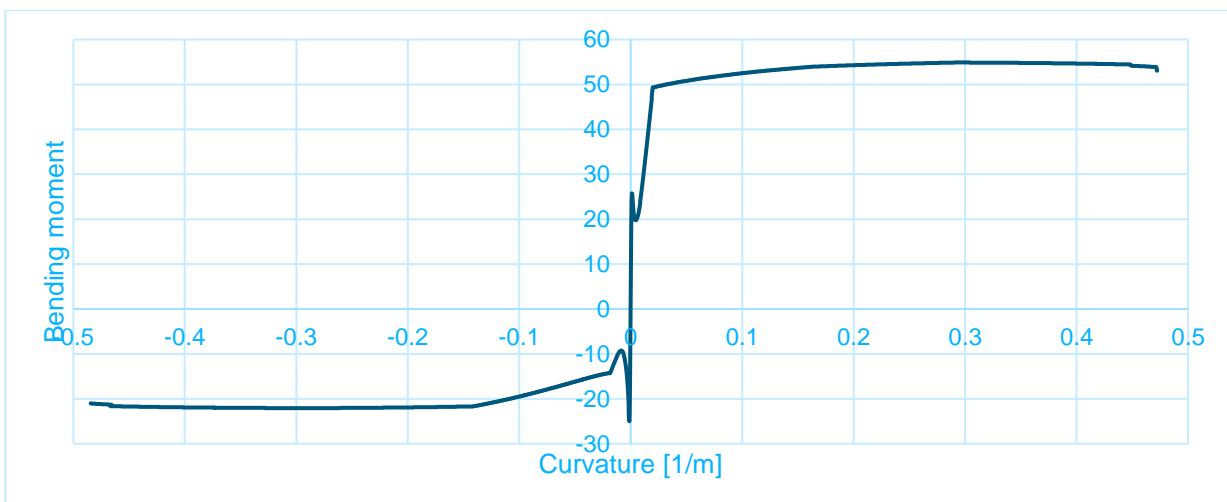
Figure 8.11: Applied force in the original calculation

8.5 Moment-curvature relationship

The moment-curvature (M- κ) graph for the main span is given in Figure 8.12. The M- κ is obtained in a deflection-controlled manner, allowing to have local snap-throughs. This is observable, for example, at the point of cracking.

The top reinforcement is considerably smaller than the bottom reinforcement. This causes the difference in the positive and negative side of the M- κ graph. The maximum moment on the positive side of the M- κ graph is reached before cracking theoretically occurs. At around the curvature of 0.45 1/m, the bending moment starts to drop. This is due to reinforcement failure.

The FDM model is force-controlled, meaning that the force can only increase. For that reason, the M- κ graph is adjusted for the FDM model in such a way that it only increases in bending moment while retaining the area under the M- κ graph.

Figure 8.12: M- κ graph in the main span direction

The direction perpendicular (secondary span) to the main span direction is relatively stiff, due to the supporting beams. Figure 8.13 shows the M- κ graph of the slab for the secondary span direction. Figure 8.14 shows the M- κ graph for the beams. Interesting to see is that the cracking moment of the beams is far beyond the ultimate moment of the slab. Therefore, it is convenient to treat the beams elastically and do a post-analysis check on the maximum bending moment in the beams to confirm that the beams are still in the elastic stage.

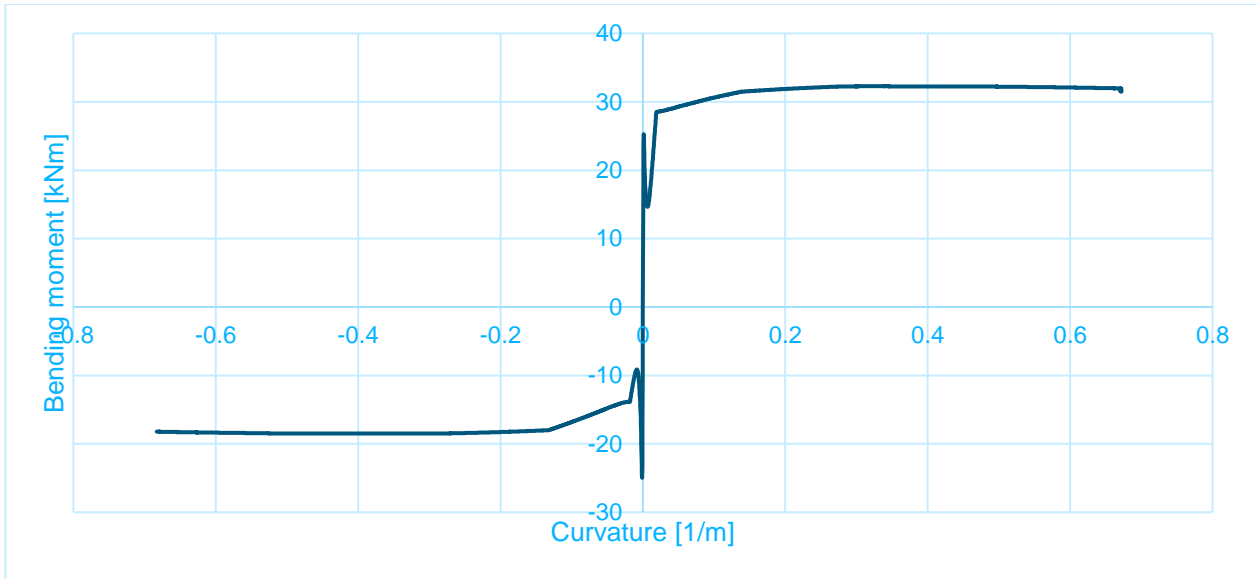


Figure 8.13: M- κ graph in the secondary span direction

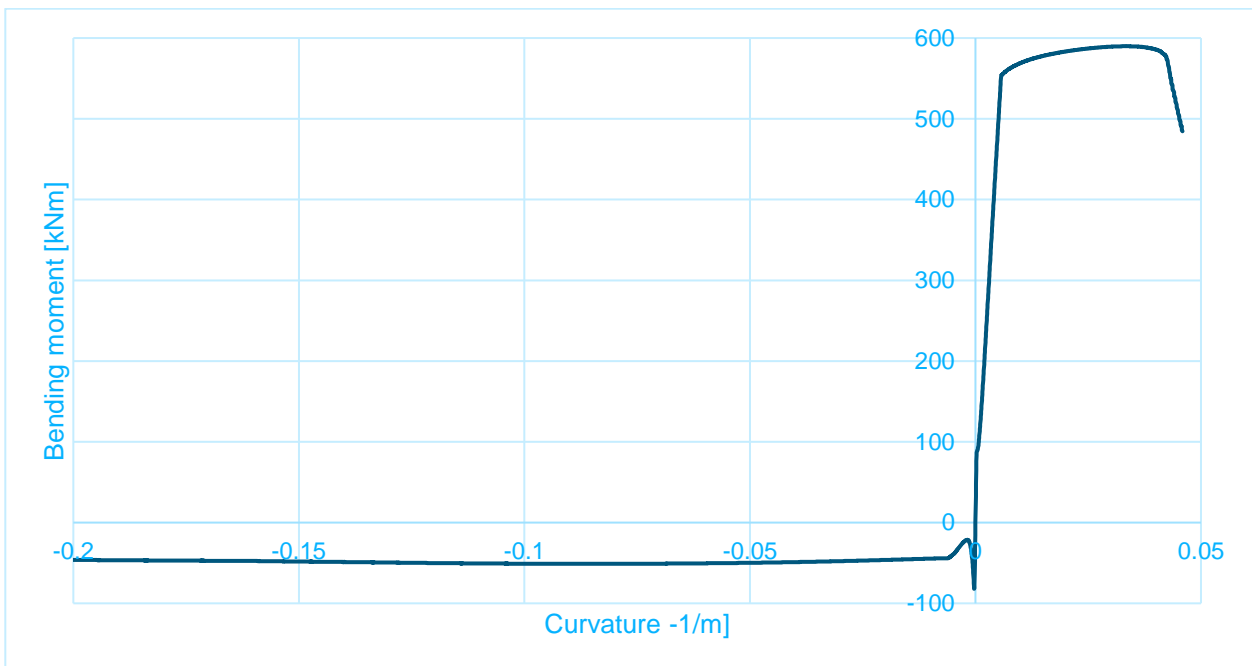


Figure 8.14: M- κ graph in the beams

8.6 Single degree of freedom mass-spring system

8.6.1 Force-deflection relationship

The F-u graph used in the analysis is shown in Figure 8.15 on the right. The dead weight is accounted for in the F-u graph.

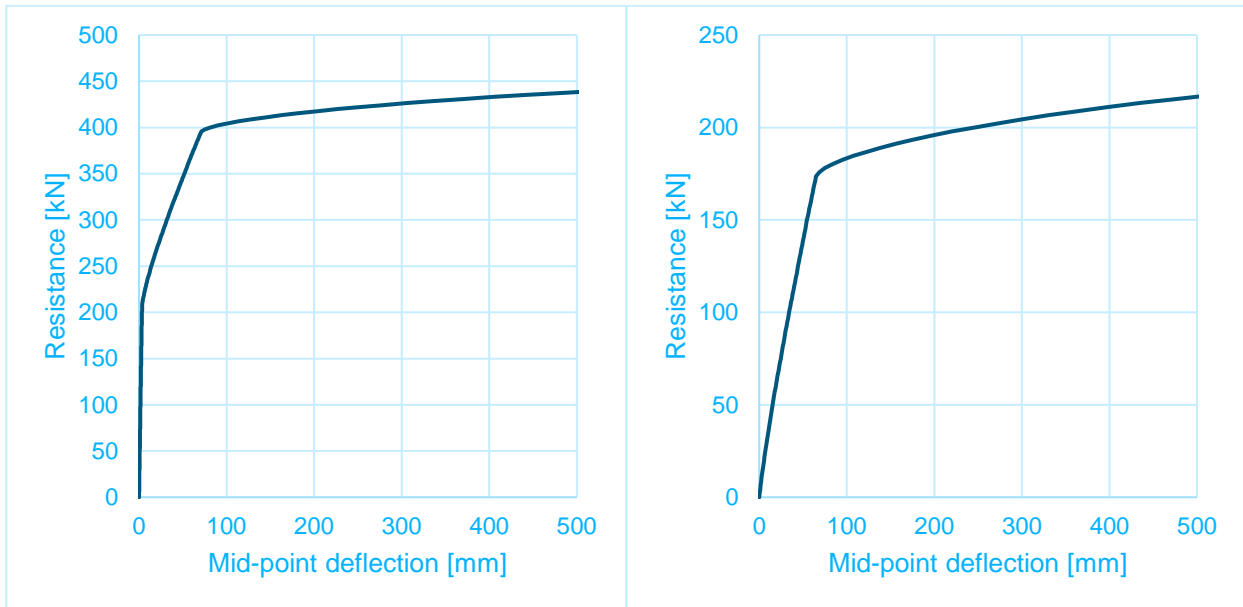


Figure 8.15: F-u graph for the SDOF mass-spring system. On the left: total F-u. On the right: Dead weight subtracted.

8.6.2 Deflection-time history

The result of the SDOF mass-spring system analysis is shown in Figure 8.16. The maximum displacement is 151 mm. The SDOF mass-spring system has decent agreement with NLTH analysis in FEM.

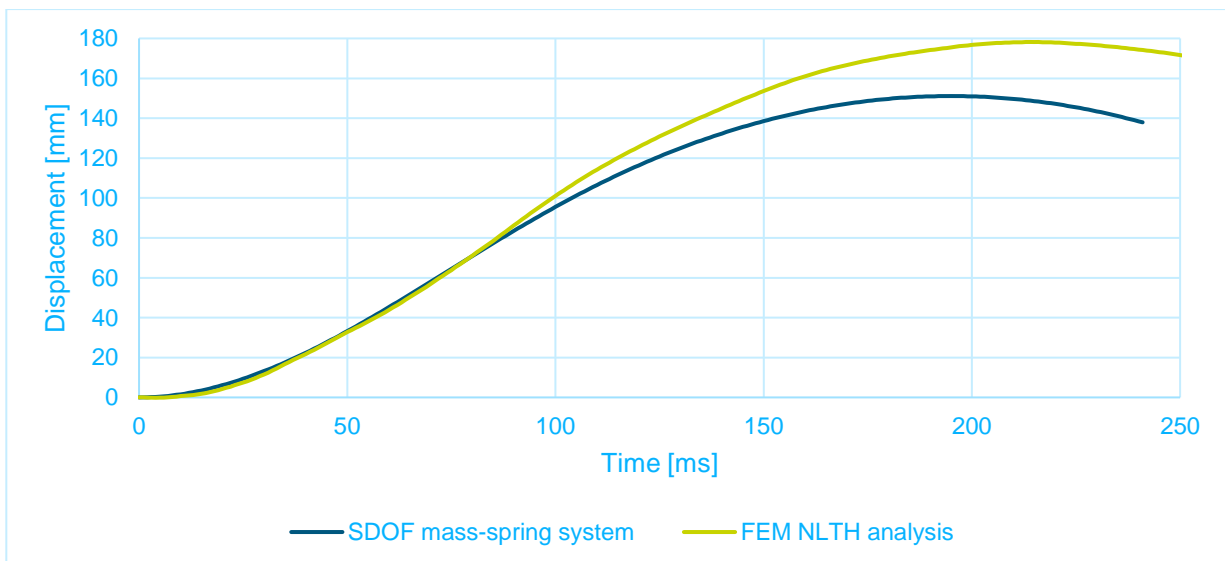


Figure 8.16: Deflection-time history graph for the SDOF mass-spring system

8.7 Two degrees of freedom mass-spring system

This paragraph presents the results of the parametric study on the influence of the edge beams on the slab. This is done by analysing the two degrees of freedom (2DOF) mass-spring system. The second degree of freedom is the deflection of the beams. The slab dimensions are fixed in the parametric study. Variations are made in the beam stiffness and beam mass.

8.7.1 Case

8.7.1.1 Force-deflection relationship

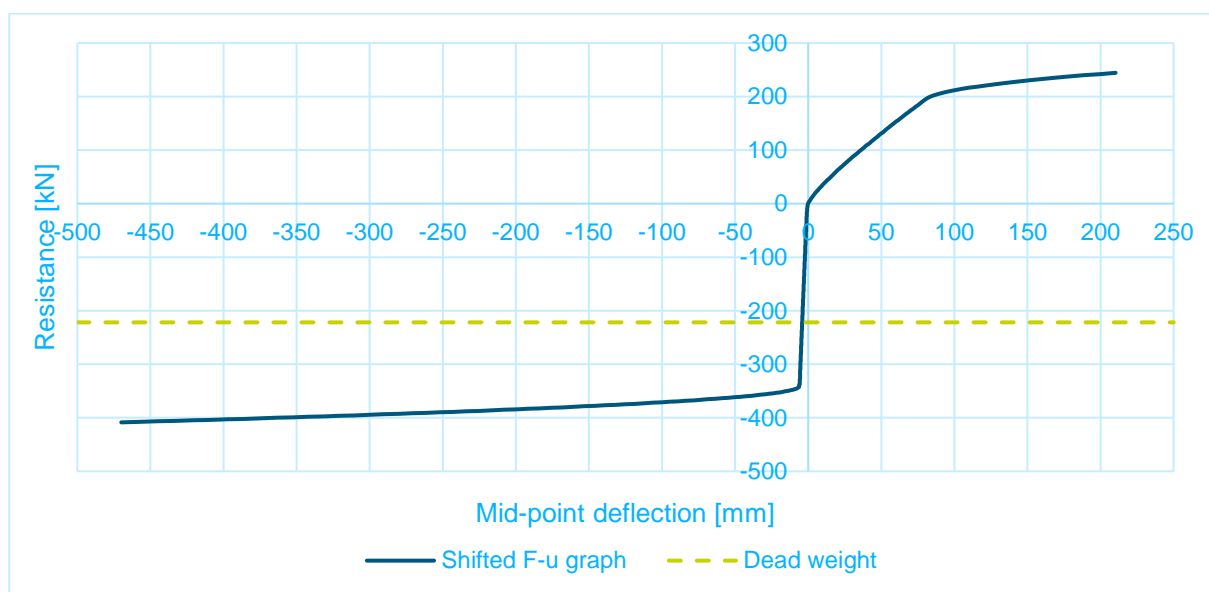


Figure 8.17: F-u graph for the 2DOF mass-spring system

The F-u graph for the beams represent the beam behaviour inside the system. Although it seems like the beam stiffness reduces at around the deflection of 2 mm because of cracking, this is not the case. The beams are rigidly connected to the slab edge and therefore the F-u graph for the beams cannot be derived manually based on a simply supported beam. Cracking might influence the F-u graph of the beams inside the system, but this is hard to distinguish.

8.7.1.2 Deflection-time history

The results of the 2DOF mass-spring analysis are shown in Figure 8.18 and Figure 8.19. The maximum and minimum total deflections are 155.6 mm and -24.9 mm, respectively. The maximum and minimum slab deflections are 184.7 mm and -79.6 mm. The beams have little influence on the total deflection.

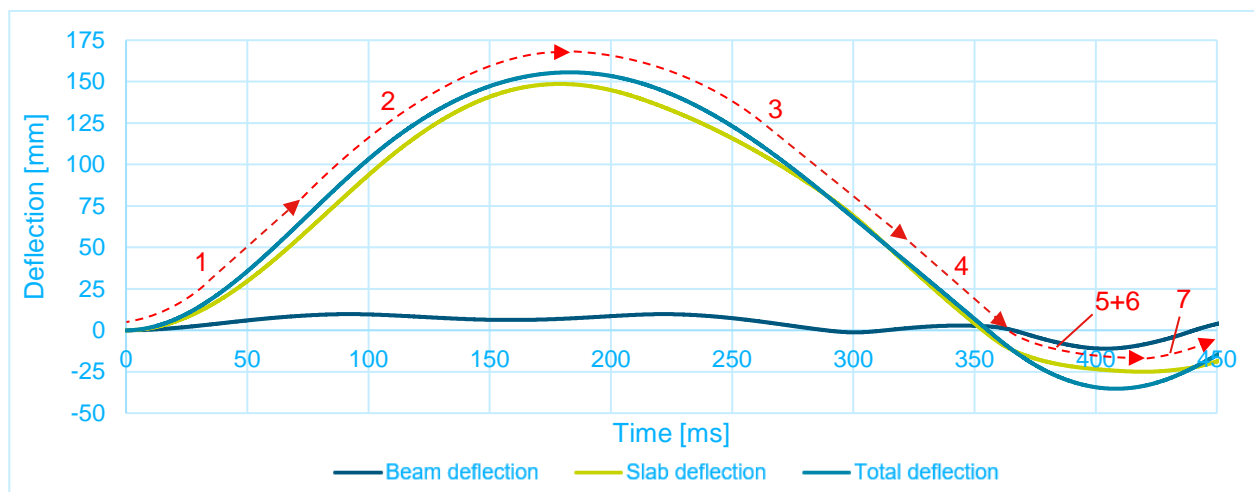


Figure 8.18: mass-spring system results of the case

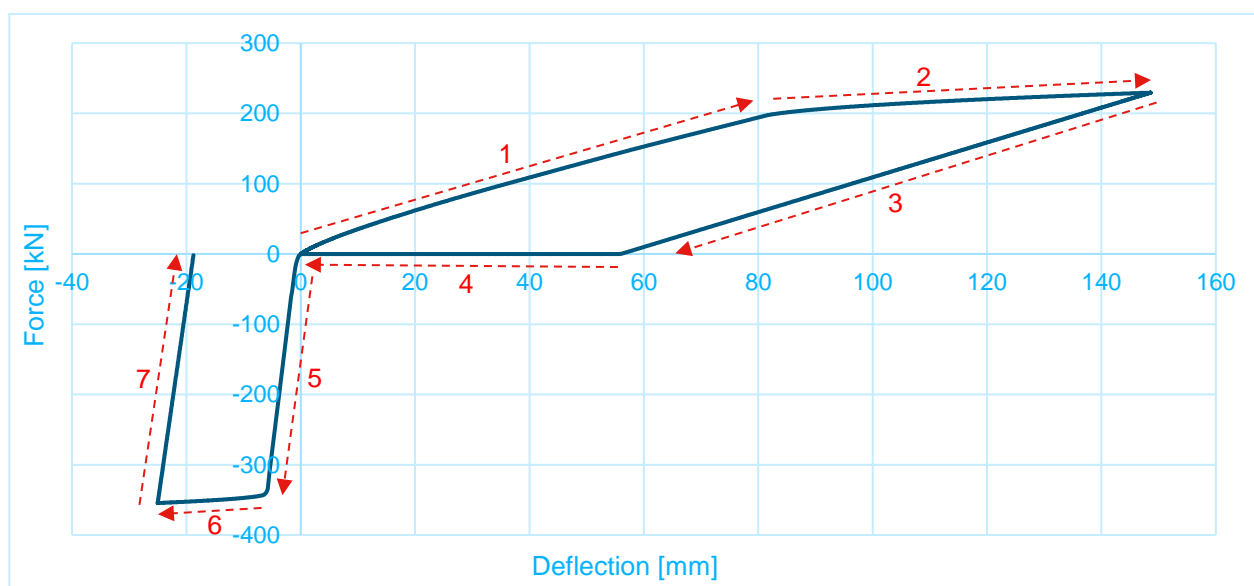


Figure 8.19: F-u graph in the mass-spring system of the case

Branches:

1. The deflection starts at the initial deflected state due to dead weight
2. The bottom reinforcement starts to yield
3. After reaching the maximum deflection, the unloading branch is followed
4. The remaining deflection is pushed back to the initial deflection state without resistance
5. The initial deflection is pushed back to the zero-deflection state
6. The upwards resistance is activated
7. The top reinforcement starts to yield

8.7.2 Parametric study

The case study shows that when the beams are 12 times stiffer relative to the slab, it has little influence in the dynamic analysis. Not only the stiffness of the beams has influence on the results, but also the mass of the beams. The stiffness of the beams determines the magnitude of the deflection, while the mass of the beams determines the response time of the beams. A higher mass leads to a slower response due to the inertia effects.

The parametric study is performed according to the flowchart in Figure 1.2, but without the experiment calibration. By comparing the presented method (FDM / mass-spring system) with FEM results, the 2DOF mass-spring system is verified.

The following variations are made:

1. SDOF and 2DOF mass-spring system comparison
 - 1.1. Beam stiffness = 1000x the edge stiffness, beam mass = 1x cross-section mass. This represents the SDOF case.
2. Beam stiffness effect
 - 2.1. Beam stiffness = 8x the edge stiffness, beam mass = 1x cross-section mass.
 - 2.2. Beam stiffness = 5x the edge stiffness, beam mass = 1x cross-section mass.
 - 2.3. Beam stiffness = 2.5x the edge stiffness, beam mass = 1x cross-section mass.
3. Beam mass effect
 - 3.1. Beam stiffness = 5x the edge stiffness, beam mass = 0.1x cross-section mass.
 - 3.2. Beam stiffness = 5x the edge stiffness, beam mass = 10x cross-section mass.

8.7.2.1 Variation 1: SDOF and 2DOF mass-spring system comparison

There are two ways to modify the 2DOF mass-spring system to get the SDOF mass-spring system results. The first is to make the beam much stiffer than the plate. This way, the beams does not deflect. The other way it to significantly increase the mass of the beam. Due to the inertia effect the beam's response is much slower than that of the slab. In the timespan of interest, the period of the first positive and first negative peak deflection of the slab, the beam will not accelerate and thereby remains on its original position.

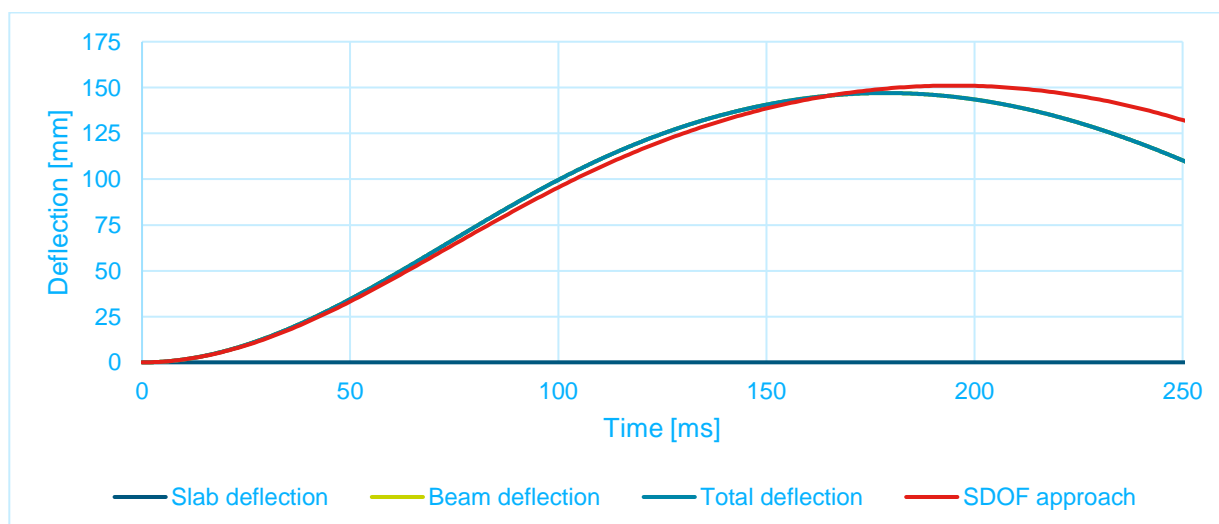


Figure 8.20: Variation 1.1: 12x the edge stiffness, beam mass = 1e6x cross-section mass

8.7.2.2 Variation 2: Beam stiffness effect

The results of the 2DOF mass spring system for variation 2 are shown in Figure 8.21, Figure 8.22, and Figure 8.23. In the latter, it is seen that the slab behaves slightly different compared to the first two graphs.

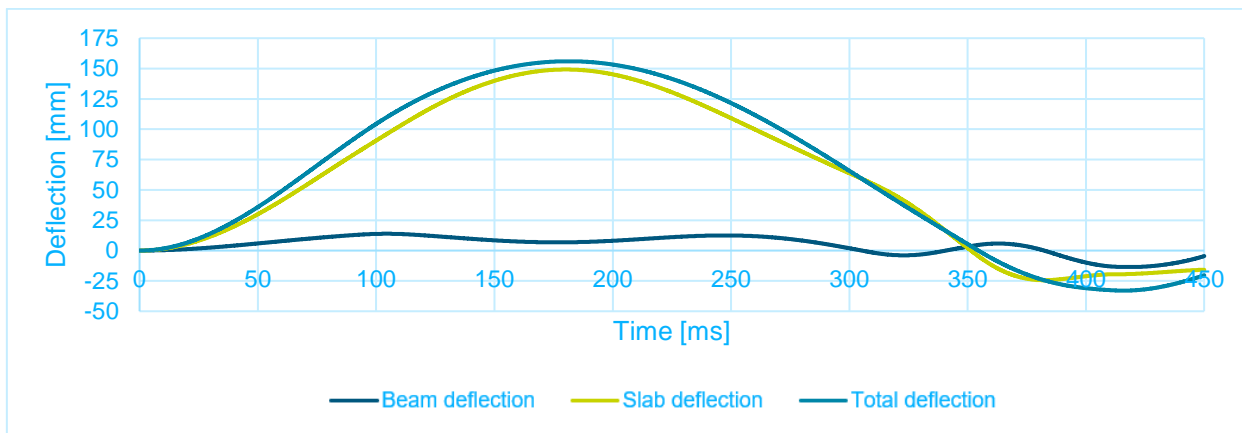


Figure 8.21: Variation 2.1: 8x the edge stiffness, beam mass = 1x cross-section mass

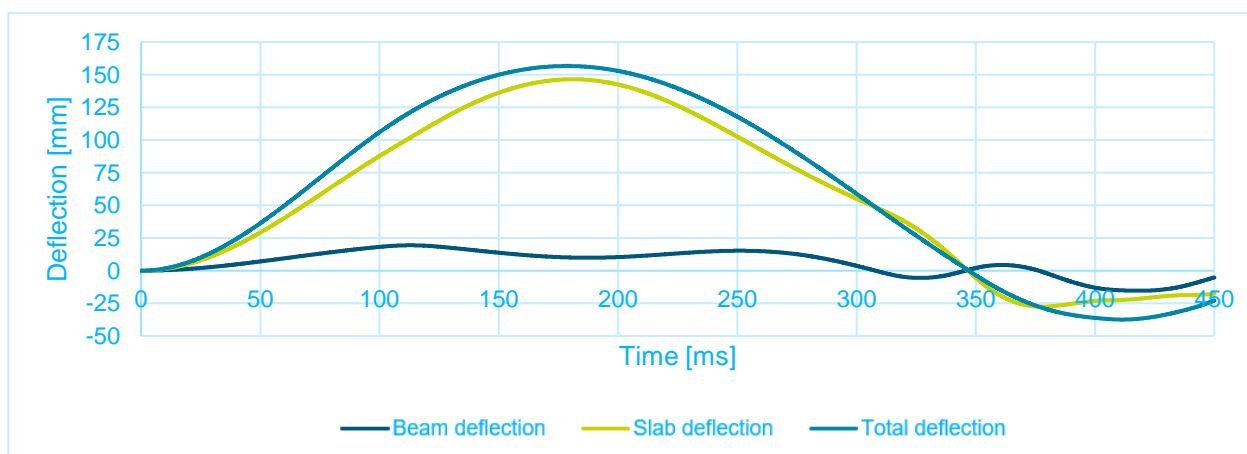


Figure 8.22: Variation 2.2: 5x the edge stiffness, beam mass = 1x cross-section mass

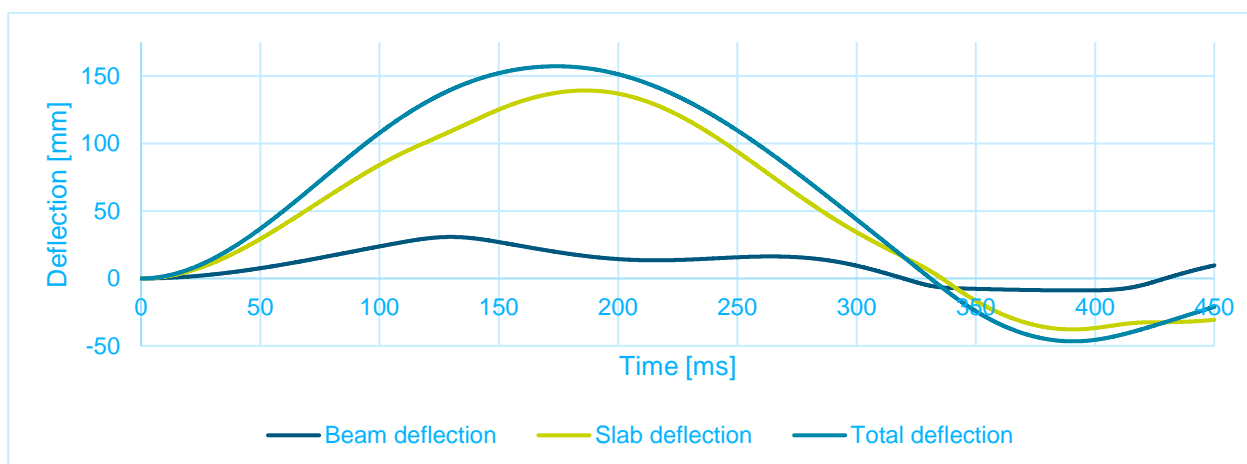


Figure 8.23: Variation 2.1: 2.5x the edge stiffness, beam mass = 1x cross-section mass

8.7.2.3 Variation 3: Beam mass effect

The results of the 2DOF mass spring system for variation 3 are shown in Figure 8.24 and Figure 8.25. The weight of the beams does not have a significant influence on the results. The beam with a larger mass has a slower response, while a smaller mass leads to a faster response.

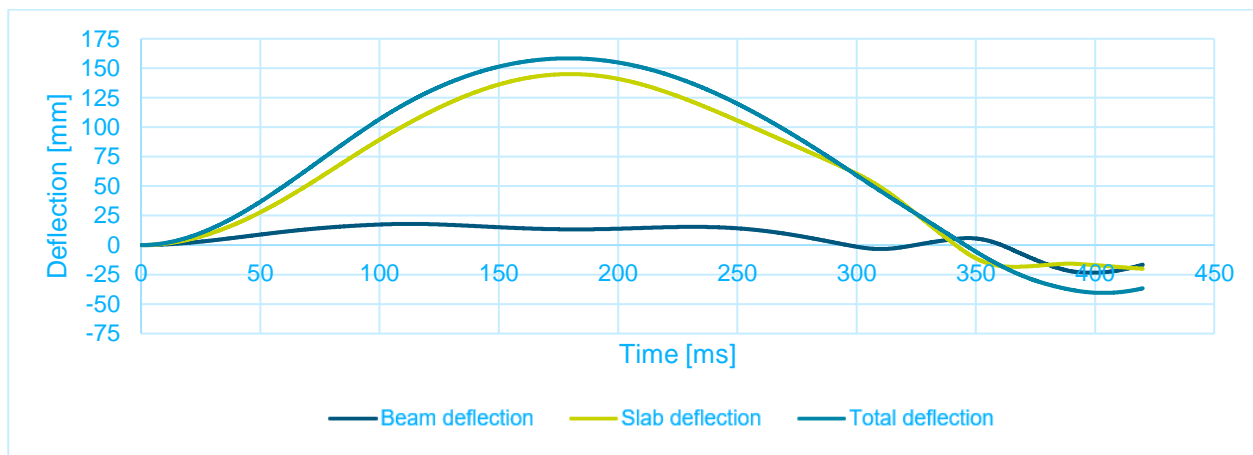


Figure 8.24: Variation 3.1: 5x the edge stiffness, beam mass = 0.1x cross-section mass

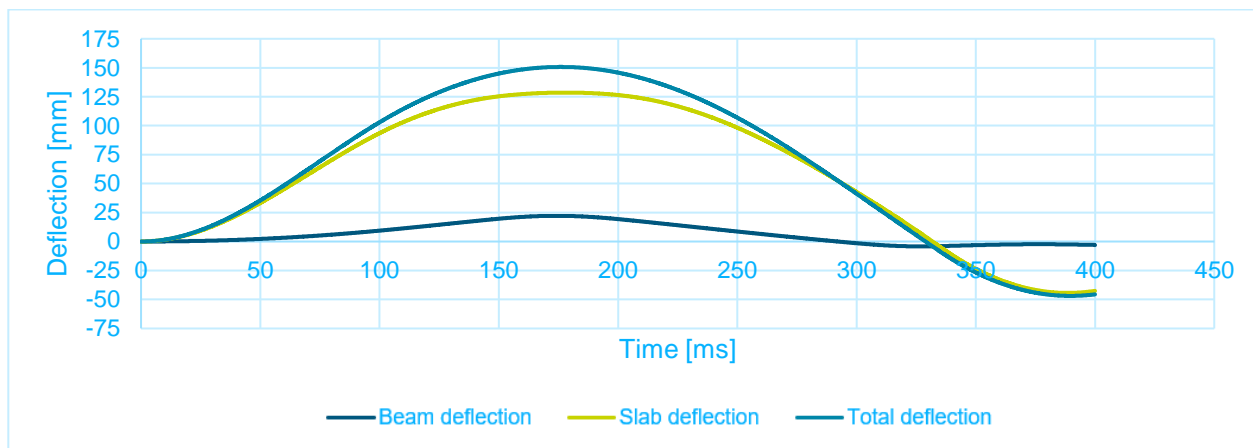


Figure 8.25: Variation 3.2: 5x the edge stiffness, beam mass = 10x cross-section mass

9 Discussion

In this chapter, the results are discussed. This discussion section is subdivided in different topics that are discussed in the Appendices. This is supplemented by the discussion of the case study results.

9.1 Nonlinear pressure distribution

Experiment 3 (Appendix III) is about the nonlinear pressure distribution. UFC 3-340-02 (Department of Defence, US, 2008) considers scaled distances above $1.2 \text{ m/kg}^{1/3}$ explosions in the 'far field' design range. The current research has shown that this does not necessarily mean that the blast load categorised in the far field design range leads to a uniform pressure distribution. Rather, the scaled distance boundary of $1.2 \text{ m/kg}^{1/3}$ says something about the failure mechanism. Below the scaled distance boundary, local failure can occur such as cratering and spalling. For close-in detonation, the blast load might cause a crater on the front face of the concrete element. On the other side (the tension side), the concrete might break off, what is called spalling. Spalling can also occur on the compressive side when high compressive forces are reached.

For scaled distances above $1.2 \text{ m/kg}^{1/3}$, flexural failure is much more likely in the blast analysis. Although the pressure on the panel in experiment 3 is more concentrated in the middle (Figure 7.7), the panel still fails on bending. For clear local failure the pressure needs to be more concentrated in the middle.

9.2 Dynamic increase factors

When a material is loaded at a high strain rate, it tends to increase the strength. The increase in strength under high strain rate conditions is called the dynamic increase factor (DIF). Sufficient information about this effect is available in literature. In general, a distinction is made for the DIF in the far field design range and the near field design range. A clear rise in DIF is observable in the found correlations between the strain rate and the DIF outside of the far field design range, as shown in chapter 3. In the far field design range, the scatter of the DIFs is small. This makes it easier to predict the DIFs beforehand. The actual DIF comes from the dynamic analysis. In the validation experiments it is concluded that the applied DIFs in each experiment do not differ much from each other, because all the experiments are in the far field design range. When the assumed DIF before the analysis is within $\pm 2\%$ compared to the actual DIF that is derived after the analysis, the changes in results are neglectable.

The DIFs in the original results of the case study are 1.1 for concrete and 1.17 for the reinforcement steel. Based on this research, the used DIFs in the analysis of the case study are 1.18 for concrete and 1.11 for reinforcement steel. This means that the DIF for reinforcement steel is slightly overestimated in the original analysis of Admin Old while the DIF for concrete is underestimated. The DIF for the reinforcement has the most effect on the results since most energy is dissipated through the plasticity of the reinforcement steel. The DIF for concrete mainly affects the compressive fracture energy. The concrete needs to be strong enough to create a lever arm in the cross-section, allowing it to resist bending moment.

9.3 Unloading stiffness

Both the outwards deflection and the inward deflection (rebound) are given in experiment 3. For this reason, the unloading stiffness needs to be defined after obtaining the maximum outwards deflection (first peak). Based on this research, the unloading stiffness equal to the cracking branch (before reinforcement yielding) fits the experimental results well. For this unloading stiffness, the deflection is slightly overestimated for the maximum inward and maximum outwards deflection. It should be noted that this requires more in-depth research for better insight in the unloading branch.

9.4 Failure mechanism

According to UFC 3-340-02, the failure criterion for elements with flexural behaviour is related to the support rotation. For elements with only actively participating reinforcement on the tension side and no possibility for membrane action, the UFC 3-340-02 limits the support rotation on 2 degrees. This is the point where crushing of the concrete may occur and thereby losing the flexural integrity of the element.

Experiment 1 (Appendix I) fails at the support rotation of 2 degrees due to reinforcement failure. The reinforcement type BSt 500S is used, which is equivalent to B500A. The ultimate strain of this type of reinforcement may be 2.5%. In contrast to the commonly used reinforcement type B500B, BSt 500S is much less ductile. There are no clear signs of failure due to crushing. At the point of failure, the strain in the outer compression fibre is slightly above 3.5 ‰. This is the strain where NEN-EN 1992-1-1 indicates crushing. The concrete compression model in NEN-EN 1992-1-1 corresponds to a discretised element length of 670 mm. This is determined by fitting the compressive stress-strain curve according to the parabolic relationship in DIANA over the NEN-EN 1992-1-1 concrete compression model, while retaining the compressive fracture energy.

The structural scheme of the element in experiment 2 (Appendix II) is the same as in experiment 1: a simply supported beam with only reinforcement on the tension side. Yet, the element in experiment 2 reaches a much higher support rotation, namely 8 degrees. There are two differences that influences the ductility of the element in experiment 2: a more ductile reinforcement steel and the element is not subjected to its self-weight.

9.5 Post-crushing behaviour

The one-way element of experiment 3 has reinforcement at the tension side and the compression side. After the concrete crushes the flexural stiffness is not immediately gone. The top reinforcement takes over the force after the compressive resistance of the concrete is lost in the crushed zone. When the top reinforcement has an equal or larger area than the bottom reinforcement, the resisting bending moment remains equal after crushing. However, in most cases the top reinforcement is smaller than the bottom reinforcement. Failure due to a force imbalance in the cross-section is avoided by including the compressive force of the concrete below the crushed zone. This results in a lower bending moment than that at the onset of crushing. The post-crushing resistance creates additional ductility of the element. This allows the structure to reach a larger support rotation compared to the element without compression reinforcement. The resisting force of the compression reinforcement is limited by its buckling force when the bars are free to buckle. Buckling may be restrained by uncrushed concrete or stirrups to transfer forces to the tension reinforcement.

9.6 Verification of the post-crushing behaviour

A comprehensive study is performed by (U.S. Army Corps of Engineers, 2008) on the comparison of SDOF analysis to a large data set of experiments (Appendix II). The referred tests in (U.S. Army Corps of Engineers, 2008) are mostly classified since they are conducted by defence departments. The study gives a good indication of the level of damage at certain support rotations. Up to 2 degrees the damage of the element can be considered moderately. Above the support rotation of 2.6 degrees the damage level is categorised as “heavy” damaged. The transition zone between 2 degrees and 2.6 degrees can lead to “moderate” damage or “heavy” damage. The crucial part of this study is that it shows the ductility of one-way elements beyond the support rotation of 2 degrees up to 6 degrees. This confirms the observations made on the ductility of one-way elements in the validation experiments.

9.7 Case study

The span of the case study slab is significantly larger than experiment 3. Both structures are roofs and subjected to their dead weight. In the case study, the dead weight has significant influence. The bending moment caused by the dead weight is already half the resisting bending moment. The blast load is therefore critical and might cause heavy damage or failure. On the other hand, the dead weight gives additional resistance for the rebound since the initial permanent deflection needs to be pushed back to the zero-deflection state first in order to activate the upwards resistance.

The analysed element of the case study is approached as a SDOF mass-spring system and 2DOF mass-spring system. The F-u graph is obtained in a FDM model. The FDM model for a one-way element is different than for a two-way element. Although the F-u graph for the one-way element and the two-way element (with stiff beams) are similar, as seen in Figure 8.15 and Figure 8.17, they are not quite the same. The main reason for the difference between the F-u graph for a one-way element and a two-way element with stiff beams is the accuracy of the FDM model. The FDM model for a one-way element is based on the beam equation and the two-way element for the plate equation. The load in the two-way element is also carried by the twisting bending moment. Also, the Poisson's ratio increases the load bearing capacity of the slab. The downside of the two-way element FDM model is that it is assumed a certain cracking pattern. Cracks are assumed through parallel and perpendicular to the element edges. When the supporting beams are stiff, this is a reasonable assumption. However, when the beams weaker or not present at all, the cracking pattern is different. For this reason, the nonlinear FDM model for the two-way element is less accurate than the nonlinear FDM model for a one-way element.

From the 2DOF mass-spring system it can be concluded that the supporting beams have little influence. This is due to the high stiffness of the beams compared to the slab. An SDOF approach is suitable for predicting the mid-span deflection of the slab. The maximum mid-span deflection in the nonlinear time history analysis of the original analysis is 144 mm, while the SDOF mass-spring system predicts 156 mm. The rebound motion is less critical due to the positive working dead weight of the concrete.

In the parametric study it is shown that when the beams are stiff enough to keep the slab undamaged in the secondary span direction (perpendicular to the main span), the dynamic response of the slab is practically independent of the beam stiffness. When the beams do not fully support the slab in the secondary span direction, the response of the slab is different. In that case, the beams dissipate more energy whereas the slab dissipated less energy.

10 Conclusions and recommendations

The conclusions are drawn by reflecting on the research objective. The research objective is formulated in a single all-encompassing question:

How can a two-way reinforced concrete slab with stiffened edges subjected to blast load be reduced to a SDOF or 2DOF mass-spring system in which it approximates the nonlinear behaviour of the experimentally tested slabs?

The research question contains a lot of elements. The following elements define the scope of the research:

- Two-way reinforced concrete slab with stiffened edges
- Blast load definition

The other elements in the research question are specifying the research objective:

- The nonlinear (static) behaviour
- The dynamic behaviour
- Experimental validation
- The choice between SDOF or 2DOF mass-spring system

To formulate a good answer, the elements in the research question are elaborated one by one in chapter 10.1 and chapter 10.2. This is followed by a summarizing answer to the research question in chapter 10.3. After that, the contribution of this research to existing studies is expounded in chapter 10.4. Finally, recommendations are put together for designing a reinforced concrete slab supported by beams in chapter 10.5. These recommendations are related to the current design method of Royal HaskoningDHV and the case study.

10.1 Reflection on the research scope and assumptions

Two-way reinforced concrete slab with stiffened edges

In the case study, a slab is assessed supported by two beams on opposing sides. This causes a main span and a secondary span. The main span is perpendicular to the beams and the secondary span is parallel to the beams. The main span is assumed to be much weaker than the secondary span (perpendicular to the main span), resulting in a clear crack through the middle of the main span. On this assumption, the finite element method (FEM) model is set up.

Blast load definition

The blast load on the element partially determines its response. The term 'blast' is used for waves generation by detonation and deflagrations. A detonation is more critical and is typically formulated as an exponentially decaying pressure function in time. Generally, the most destructive part of the blast wave, the positive phase, passes by in less than 0.1 seconds. Blast waves generated by deflagrations are not considered in this research.

A distinction is made between near field explosions and far field explosions. Near field explosions, as the name suggests, are more close-in explosions. Typically, near field explosions cause local failure. This is hard to capture in a mass-spring system. The behaviour of RC elements subjected to close-in explosions is often analysed in FEM software with explicit solvers, such as Abaqus and LS-DYNA. For this type of behaviour and load definition, DIANA is not preferred. This research focusses on the far field explosions, leading to flexural failure.

10.2 Reflection on the research objective

The nonlinear behaviour

The nonlinear behaviour in the mass-spring system is covered by the force-deflection (F-u) relationship. The F-u graph can be constructed in various ways. In this research, the F-u graph is obtained by use of the FDM model. The F-u graph of the FDM model is compared with the F-u graph of the finite element method (FEM) model. For the one-way element, good agreement is found between the FDM model and the FEM model. The FDM model for the two-way element deviates a little. This is because a discrete crack through the middle of the element is assumed in the FDM model. This is true when the supporting beams are relatively stiff. When this is not the case, the actual yield lines are not through the middle of the element.

The mass-spring system is validated by published experiments. From the experiments it turned out that concrete crushing occurs at around a support rotation of 2 degrees. This is followed by the loss of flexural resistance. This is in line with the UFC 3-340-02. For a rough design check, the FEM results can be checked for the support rotation of 2 degrees for slabs without the possibility of membrane action. The more accurate way is to compare the moment-curvature (M- κ) graph in FEM with the constructed M- κ as described in chapter 4.

The mass-spring system transforms the mass and load into a point mass and spring. Not all the mass of the element contributes to the mass-spring system. The same holds for the load. The participating mass factor and participating load factor can be extracted from the deflection of the element. When the load is more concentrated in the middle, the load factor increases. It is shown in the validation experiments that for scaled distances above $1.2 \text{ m/kg}^{1/3}$ the load factor does not differ much compared to the distributed load case.

The dynamic behaviour

The dynamic behaviour involves two main additions in comparison with the static behaviour. The first addition is the inclusion of damping and inertia. Typically, the influence of damping is small while the inertia effects is significantly larger and can dominate in the structural response. This is especially true when the duration of the load is much shorter than the structural response time.

The second addition is the strength increase for the materials under blast loading conditions. This is incorporated by the DIF. The UFC 3-340-02 gives accurate formulas for the DIFs. The Model Code 2010 is rather conservative. Besides the formulas, the UFC 3-340-02 also gives a table with predefined DIFs. In general, this table is conservative. For low material strain rates, the table is more accurate and might overestimate the DIF for reinforcement steel slightly.

Experimental validation

The presented method of analysis (chapters 4-6) is applied on several published experiments. When using the real material parameters taking into account the DIFs, the results of the analysis (FEM or FDM) are a good approximation for a simply supports one-way element. Based on the assessed experiments, it is safe to assume that the failure mechanism for a one-way element in the far field design range is reinforcement failure. UFC 3-340-02 advises to design on a support rotation of 2 degrees. This is where crushing may occur. In the analysis of experiment 1, it is seen that the strain in the outer compressive fibre is around 3.5 ‰ at the support rotation of 2 degrees. This value for the ultimate strain is commonly used as the ultimate strain of concrete because NEN-EN 1992-1-1 (Normcommissie 351 001 "Technische Grondslagen voor Bouwconstructies", 2011) prescribes it. Defining the ultimate strain in FEM analysis is inconvenient. This makes the results mesh dependant since the compressive fracture energy remains equal for any mesh size. Using an energy based concrete model for both tension and compression makes the FEM model mesh independent. Generally, this leads to a much larger ultimate strain of the discretised

element. The NEN-EN 1992-1-1 concrete compression model corresponds to a discretised element length of 670 mm, while the mesh size in FEM is usually smaller.

The analyses show that the concrete compressive force is spread out over a certain area. This is seen in experiment 2, where the concrete is clearly spalling over a relative wide area. It shows that there is plenty energy absorption capacity left in the structure after the support rotation of 2 degrees.

The choice between SDOF or 2DOF mass-spring system

The case study showed that for stiff beams, the beams can be modelled elastically. A post-analysis check on the maximum moment should be done. When the beams are stiff (14x stiffer), the contribution of the beams to the total mid-slab deflection is neglectable. A parametric study has shown that for beams with a spring stiffness ratio compared to the slab lower than 5, the contribution of the beam should be considered.

10.3 Reflection on the problem statement

The two-way reinforced concrete slab with stiffened edges can be reduced to a mass-spring system that correctly calculates the nonlinear behaviour by using:

- The correct dynamic increase factors, which chapter 3 provides, on the material properties.
- An accurately defined force-deflection relationship, which reflects the real nonlinear behaviour as good as possible.

The two-way reinforced concrete slab subjected to blast load can be reduced to a SDOF mass-spring system under the following conditions:

- The scaled distance Z is above $1.2 \text{ m/kg}^{1/3}$. This is referred to as the far field design range. In this range, flexural behaviour of the slab may be assumed.
- The DIFs are chosen carefully, preferably using the empirical relations as described in chapter 3.
- The supporting beams are 5 times stiffer relative to the slab. When the beam stiffness ratio is lower, the contribution of the beams to the total slab deflection should be considered. A 2DOF mass-spring system is then more appropriate.
- Cracks form perpendicular to the main span direction. This is the case in the used experimentally tested slabs

10.4 Contribution of this research to existing studies

The main addition of this research to existing studies is the extensive use of a mass-spring system, specifically the single degree of freedom (SDOF) approach. The SDOF mass-spring system is validated by published experiments. In most experiments, the specimen is analysed in FEM software but sometimes a SDOF mass-spring system is used. In the reports of the experiments, simplifications are made at some point in the analysis. Whether it be the moment-curvature ($M-\kappa$) graph, the force-deflection ($F-u$) graph or the participating load and mass factors.

The presented analysis method of a one-way element is accurate throughout the whole analysis and is applied on multiple published experiments. It originates from the underlying python scripts where the running variable is incrementally increased. By remembering the previous steps in the script, the cracking and yielding branches are well-captured in both the $M-\kappa$ graph and the $F-u$ graph. There are no publications available on the use of the FDM for cracking reinforced concrete (RC) elements. This research presents an accurate technique to implement it on symmetric beams.

The two degrees of freedom (2DOF) mass-spring system is specific for this research. It is not validated by experiments. The validity of the model is affirmed by modifying a similar example in (Biggs, 1964), a

leading source on the topic of dynamic analysis. The 2DOF mass-spring system is compared with FEM results. For the elastic case, the 2DOF mass-spring system matches the FEM results. When cracking of concrete gets involved, the 2DOF mass-spring system deviates a little from the FEM results, but with an acceptable error.

10.5 Recommendations and further development

As concluded before, the nonlinear FDM model for the one-way element is more accurate than the nonlinear FDM model for the two-way element. The loss of accuracy appears after severe cracking occurs through the middle of the two-way element. This is mainly because for relative weak beams, the real cracking pattern is different than assumed in the FDM model. In this research, the nonlinear FDM model for the two-way element is valuable to analyse the effect of the beams. The FDM model for the one-way element is significantly faster than the FDM model for a two-way element and is therefore more suitable for a quick judgement. The two-way element FDM model is practically useable for small spans (leading to less nodes, which reduces computation time) and a clear dominating span. Because of the downsides of the two-way element FDM model, it is not recommended to use it as a design tool.

The FDM model can be significantly improved by implementing the arc-length method. This is an improvement on a force-controlled analysis to accomplish what a deflection-controlled analysis would achieve. The arc-length method makes it possible to continue to analysis after reaching the maximum allowable force, when there is still energy absorption capacity left in the structure.

The unloading stiffness should be investigated more thoroughly for better insight in the rebound deflection. It is not trivial what the exact unloading stiffness should be after the reinforcement has yielded. This research uses the slope of the cracked branch (before reinforcement yielding) in the F-u graph as an approximation for the unloading stiffness. This seems to be a reasonable assumption.

The most important recommendation in relation to blast analysis are listed below:

- When applicable, the SDOF mass-spring system can provide quick and accurate results. It can also serve as a model check for DIANA. Likewise, the constructed M- κ graph (chapter 4) and the constructed F-u graph (chapter 5) can be used to check the DIANA results.
- When the scaled distance is below $0.4 \text{ m/kg}^{1/3}$, the blast analysis should be performed in FEM software with explicit solvers. For scaled distances above $1.2 \text{ m/kg}^{1/3}$, DIANA or a mass-spring system may be used. For the scaled distances in between $0.4 \text{ m/kg}^{1/3}$ and $1.2 \text{ m/kg}^{1/3}$, DIANA or a mass-spring system can provide good results, but the nonlinear pressure distribution over the one-way element must accurately modelled.
- Slabs where the beam deflection has a considerably effect on the slab deflection, DIANA is preferred over the two-way element FDM model to construct the F-u graph. The 2DOF mass-spring system can still be used.
- The beams in the case study can be modelled elastically because of the high stiffness relative to the slab. Generally, the beams are much stiffer than the slab to fulfil their function of supporting the slab.
- The DIFs should be chosen according to the empirical relations mentioned in chapter 3.

11 References

- Abedini et al. (2018). Pressure–Impulse (P–I) Diagrams for Reinforced Concrete (RC) Structures: A Review. *Archives of Computational Methods in Engineering* 26, 733-767.
- Atchley, B., & Furr, H. (1967). Strength and energy absorption capabilities of plain concrete under dynamic and static loadings. *Journal of the American Concrete Institute* 64, 745-756.
- Baker et al. (1983). *Explosion Hazards and Evaluation*. Amsterdam, New York: Elsevier scientific journals.
- Batista, M. (2010). New analytical solution for bending problem of uniformly loaded rectangular plate supported on corner points. *The IES Journal Part A: Civil & Structural Engineering*, 75-84.
- Biggs, J. M. (1964). *Introduction to Structural Dynamics*. New York: McGraw-Hill Book Company.
- Bischoff, P., & Perry, S. (1991). Compressive behaviour of concrete at high strain rates. *Materials and Structures* 24, 425-450.
- Blaauwendraad, J. (2010). *Plates and FEM: Surprises and Pitfalls*. Dordrecht: Springer.
- Bort et al. (2011). *JOHNSON-COOK PARAMETER IDENTIFICATION FOR AISI-304 MACHINING THROUGH NELDER MEAD METHOD*. Trento, Italy: Department of Mechanical and Structural Engineering (DIMS), University of Trento.
- Bridgman, P. (1952). *Studies in Large Plastic Flow and Fracture*. New York: McGraw-Hill.
- Brookes, C. (2015). *How to Model Structural Concrete using Finite Element Analysis*. NAFEMS.
- Brookes, C. (2015). *How to Model Structural Concrete using Finite Element Analysis*. NAFEMS.
- Cadoni, E., & Forni, D. (2015). *Strain rate effects on reinforcing steels in tension*. EDP Science.
- Cavill, B., Reberntrost, M., & Perry, V. (2006). Ductal® -An Ultra-High Performance Material for Resistance to Blasts and. *1st Specialty Conference on Disaster Mitigation*. Calgary, Alberta, Canada.
- Chen et al. (2014). AN IMPROVED ANALYTICAL METHOD FOR RESTRAINED RC STRUCTURES SUBJECTED TO STATIC AND DYNAMIC LOADS. *International Journal of Structural Stability and Dynamics* vol. 14, no. 1.
- Cui et al. (2021). Improved resistance functions for RC elements accounting for compressive and tensile membrane actions. *Engineering Structures* 251.
- Cui et al. (2022). Improved resistance functions for RC elements accounting for compressive and tensile membrane actions. *Engineering Structures* 251.
- Cusatis, G. (2010). Strain-rate effects on concrete behavior. *International Journal of Impact Engineering*, 162-170.
- Dargel, H. (1985). *Zur rechnerischen Analyse von Stahlbetontragwerken unter stoßartiger Beanspruchung*. Darmstadt.
- Department of Defence, US. (2008). *UFC 3-340-02 - STRUCTURES TO RESIST THE EFFECTS OF ACCIDENTAL EXPLOSIONS*. Unified Facilities Criteria (UFC 3-340-02).
- Draganić, H., & Sigmund, V. (2012). BLAST LOADING ON STRUCTURES. *Tehnički vjesnik* 19, 643-652.
- Draganic, H., Varevac, D., & Lukic, S. (2018). An Overview of Methods for Blast Load Testing and Devices for Pressure Measurement. *Advances in Civil Engineering*.
- Fachbereich 07 „Beton- und Stahlbeton/Deutscher Ausschuss für Stahlbeton“. (2008). *DIN 1045-1:2008-08: Tragwerke aus Beton, Stahlbeton und Spannbeton - Teil 1: Bemessung und Konstruktion*. Berlin: Deutsches Institut für Normung E.V. (DIN).
- Faizul, M. (2016). The Effects of Strain Rate on Concrete Strength under Dynamic Impact Load. *Journal of Bangladesh Electronics Society*.
- Fédération internationale du béton (fib). (2013). *fib Model Code for Concrete Structures 2010*. Lausanne: Ernst & Sohn.
- Gao et al. (2019). *Rate effect on the stress–strain behavior of concrete under uniaxial tensile stress*. Shanghai, China: Department of Structural Engineering, Tongji University.
- Gazetas, G. (1991). *FORMULAS AND CHARTS FOR IMPEDANCES OF SURFACE AND EMBEDDED FOUNDATIONS*. ASCE.

- Hendriks, & Roosen. (2020). *Guidelines for Nonlinear Finite Element Analysis of Concrete Structures*. Rijkswaterstaat Centre for Infrastructure.
- Hendriks, M. A., & Roosen, M. A. (2019). *Guidelines for Nonlinear Finite Element Analysis of Concrete Structures*. Rijkswaterstaat Centre for Infrastructure.
- Johnson, G., & Cook, W. (1983). A CONSTITUTIVE MODEL AND DATA FOR METALS SUBJECTED TO LARGE STRAINS, HIGH STRAIN RATES AND HIGH TEMPERATURES. *Proceedings 7th International Symposium on Ballistics*, 541-547.
- Joint Committee on Structural Safety. (2001). *PROBABILISTIC MODEL CODE*. Joint Committee on Structural Safety.
- Joint Research Centre. (2013). *Calculation of Blast Loads for Application to Structural Components*. Luxembourg: Publications Office of the European Union.
- Joint Research Centre. (2015). *Recommendations for the improvement of existing European norms for testing the resistance of windows and glazed façades to explosive effects*. Luxembourg: Publications Office of the European Union.
- Joint Research Centre. (2016). *Analysis of blast parameters in the near-field for spherical free-air explosions*. Luxembourg: Publications Office of the European Union.
- KALMAN, D. (2010). *USE OF STEEL FIBER REINFORCED CONCRETE FOR BLAST RESISTANT DESIGN*. Manhattan, Kansas: Kansas State University.
- Körmeling, H., & Reinhardt, H. (1987). Strain rate effects on steel fibre concrete in uniaxial tension. *The International Journal of Cement Composites and Lightweight Concrete*, Vol. 9, No. 4, 197-204.
- Krauthammer et al. (2008). Pressure–impulse diagrams for the behavior assessment of structural components. *International Journal of Impact Engineering* 35, 771-783.
- Le Roy et al. (1981). A MODEL OF DUCTILE FRACTURE BASED ON THE NUCLEATION AND GROWTH OF VOIDS. *acta metallurgica vol. 29*, 1509-1522.
- Lin et al. (2016). Strain Rate Behavior in Tension of Reinforcing Steels HPB235, HRB335, HRB400, and HRB500. *Materials vol. 9 (MDPI)*, 1013.
- McCann, D., & Smith, S. (2007). Blast Resistant Design of Reinforced Concrete Structures. *Structure magazine* 26.
- Ministerie van Verkeer en Waterstaat. (2003). *Publicatiereeks Gevaarlijke Stoffen 1 deel 2B: Effecten van explosie op constructies*. PSG-beheerorganisatie.
- Murugesan, M., & Jung, D. (2019). Johnson Cook Material and Failure Model Parameters estimation of AISI-1045 Medium Carbon Steel for metal Forming Applications. *Materials vol. 12 (MDPI)*, 609.
- Ngo, T., Mendis, P., & Krauthammer, T. (2007). Behavior of Ultrahigh-Strength Prestressed Concrete Panels Subjected to Blast Loading. *Journal of Structural Engineering vol. 133, issue 11*, 1582-1590.
- Normcommissie 351 001 "Technische Grondslagen voor Bouwconstructies",. (2011). *NEN-EN 1992-1-1+C2: Eurocode 2: Design of concrete structures – Part 1-1: General rules and rules for buildings*. Delft: Nederlands Normalisatie Instituut.
- Ozbolt et al. (2014). Tensile behavior of concrete under high loading rates. *International Journal of Impact Engineering* 69, 55-68.
- Park, G.-K., Kwak, H.-G., & Filippou, F. (2017). Blast Analysis of RC Beams Based on Moment-Curvature Relationship Considering Fixed-End Rotation. *Journal of Structural engineering vol. 143, issue 9*.
- Pham. (2015). An Experimental Study of Reinforced Concrete Façade Panels and Their Fixing Assemblies Subjected to Blast Loads. *Electronic Journal of Structural Engineering* 15.
- Pham et al. (2009). A study of the effects of fixing assemblies on the behaviour of reinforced concrete panels subjected to blast loads. *8th International Conference on Shock & impact loads on structures*. Adelaide, Australia.
- Pham, T., & Ngo, T. (2015). An Experimental Study of Reinforced Concrete Façade Panels and Their Fixing Assemblies Subjected to Blast Loads. *Electronic Journal of Structural Engineering* 15.

- Piani et al. (2019). Dynamic Increase Factors for Adobe : Addressing the dynamic strength in compression for earthen materials. *18th International Symposium for the Interaction of Munitions with Structures*. Panama city beach, Florida, US.
- Raman et al. (2012). Experimental Investigation on the Behaviour of RC Panels Retrofitted with Polymer Coatings under Blast Effects. *Proceedings of the 2nd International Conference on Sustainable Built Environment*. Kandy, Sri Lanka.
- Raman et al. (2014). Retrofitting of RC panels subjected to blast effects using elastomeric polymer coatings. *Proceedings of Concrete Solutions, 5th International Conference on Concrete Repair*. Belfast, UK.
- Riedel et al. (2008). Numerical Assessment for Impact Strength Measurements in Concrete Materials. *International Journal of Impact Engineering* 36, 283.
- Riedel et al., W. (2009). *Engineering and numerical tools for explosion protection of reinforced concrete*. Efringen-Kirchen, Germany: Dep. Safety Technology and Protective Structures, Ernst-Mach-Institut, Fraunhofer Society,.
- Royal HaskoningDHV. (2020). *Report BG8305-RHD-01-ZZ-RP-S-0002, version P01/S0*. Rotterdam.
- Saieni, H. (2012). *Non-linear vibrations of tensegrity structures*. Stockholm, Sweden: KTH Royal institute of technology.
- Schuler et al. (2006). Spall experiments for the measurement of the tensile strength and fracture energy of concrete at high strain rates. *International Journal of Impact Engineering* 32, 1635 - 1650.
- Selby, R., & Vecchio, F. (1997). A constitutive model for analysis of reinforced concrete solids. *Canadian Journal of Civil Engineering* 24, 460-470.
- Syed et al. (2018). The Failure Behaviour of Reinforced Concrete Panels Under Far-field and Near-field Blast Effects. *Structures* 14, 220-229.
- Takeda (2), J., & Tachikawa, H. (1962). The mechanical properties and their fundamental equations of concrete subjected to compression in high rates of loading (in Japanese). *ibid. No. 78*, 1-6.
- Takeda (3), J., & Tachikawa, H. (1972). Deformation and fracture of concrete subjected to dynamic load. *Mechanical Behaviour of Materials vol. 4*, 267-277.
- Takeda, J., & Tachikawa, H. (1962). The mechanical properties of several kinds of concrete at compressive, tensile, and flexural tests in high rates of loading (in Japanese). *Trans. Architect. Inst. Jpn No. 77*, 1-6.
- Tanapornraweekeit et al. (2007). Modelling of a Reinforced Concrete Panel Subjected to Blast Load by Explicit Non-linear FE Code. *Proceedings Of Earthquake Engineering In Australia Conference 2007*. Wollongong, australia.
- Task Group 8.2. (2008). *fib bulletin 42: Constitutive modelling of high strength / high performance concrete*. Lausanne, Switzerland: fédération internationale du béton (fib).
- The Finite Element Method for the Analysis of Non-Linear and Dynamic Systems: Non-Linear Dynamics Part I (Powerpoint presentation)*. (2017, November 23). Retrieved from https://ethz.ch/content/dam/ethz/special-interest/baug/ibk/structural-mechanics-dam/education/femII/2021/Lecture_5_dynamics_part_I.pdf
- TNO. (2005). *Methods for the calculation of physical effects (Yellow book)*. The Hague: PSG-Beheerorganisatie.
- U.S. Army Corps of Engineers. (2008). *Methodology Manual for Component Explosive Damage - Assessment Workbook (CEDAW)*.
- van der Meer, L. (2008). *Dynamic response of high-rise building structures to blast loading*. Eindhoven: Eindhoven University of Technology.
- Vecchio, F., & Collins, M. (1993). Compression Response of Cracked reinforced Concrete. *Journal of Structural Engineering vol. 119, no. 19*, 3590-3610.
- Vegt, & Weerheijm. (2016). *INFLUENCE OF MOISTURE ON THE FRACTURE BEHAVIOUR OF CONCRETE LOADED IN DYNAMIC TENSION*. Rijswijk: TNO Defence, Safety and Security.

- Wang et al. (2012). A new non-uniform blast load model for SDOF method of one-way reinforced concrete slab. *EPJ Web of Conferences* 26.
- Wang, S., Zhang, M.-H., & Quek, S. (2011). Effect of Specimen Size on Static Strength and Dynamic Increase Factor of High-Strength Concrete from SHPB Test. *Journal of Testing and Evaluation*, Vol. 39, No. 5.
- Watstein (2), D. (1955). Properties of concrete at high rates of loading. *Symposium on Impact Testing*, 156-169.
- Watstein, D. (1953). Effect of straining rate on the compressive strength and elastic properties of concrete. *Journal of the American Concrete Institute* vol. 49, 729-744.
- Weerheijm, J., & Van Doormaal, J. (2007). Tensile failure of concrete at high loading rates: New test data on strength and fracture energy from instrumented spalling tests. *International Journal of Impact Engineering* 34, 609-626.
- Weerheijm, J., & Vegt, I. (2010). *The dynamic fracture energy of concrete. Review of test methods and data comparison*. Rijswijk: Delft University of Technology, The Netherlands and TNO Defence Security and Safety.
- Weerheijm, J., Mediavilla, J., & Van Doormaal, J. (2009). Explosive loading of multi storey RC buildings: Dynamic response and progressive collapse. *International Journal Structural Engineering and Mechanics* 32, 193-212.
- Weerheijm, J., Van Doormaal, A., & Mediavilla, J. (2008). CONCRETE STRUCTURES UNDER BLAST LOADING DYNAMIC RESPONSE, DAMAGE, AND RESIDUAL STRENGTH. *Resilience of Cities to Terrorist and other Threats*, 217-238.
- Weerheijm, J., Vegt, I., & van Breugel, K. (2007). *Research developments and experimental data on dynamic concrete behaviour*. Rijswijk: Delft University of Technology, TNO Defence Security and Safety.
- Wu et al. (2009). Blast testing of ultra-high performance fibre and FRP-retrofitted concrete slabs. *Engineering Structures* 31, 2060 - 2069.
- Wu et al. (2009). Blast testing of ultra-high performance fibre and FRP-retrofitted concrete slabs. *Engineering Structures* 31, 2060-2069.
- Yue et al. (2017). 2363. Analytical study of local damage on concrete slab subjected to a contact explosion. *JVE INTERNATIONAL LTD. JOURNAL OF VIBROENGINEERING* vol. 17, issue 2.
- Zeng et al. (2020). Dynamic Tensile Behavior of Steel HRB500E Reinforcing Bar at Low, Medium, and High Strain Rates. *Materials* vol. 13 (MDPI), 185.
- Zhang, C., Gholipour, G., & Mousavi, A. (2020). Blast loads induced responses of RC structural members: State-of-the-art review. *Composites Part B* 195.

Appendices

Appendix I – Experiment 1

Appendix II – Experiment 2

Appendix III – Experiment 3

Appendix IV – Analytical solution to the SDOF mass-spring system